EFFECTIVENESS OF MARKOV RANDOM FIELD BASED METHOD FOR SUPER-RESOLUTION MAPPING IN IDENTIFYING SMALL LANDSCAPE ELEMENTS AND FOREST ENCROACHMENT FROM SATELLITE IMAGES

LAXMI KANT TIWARI
Enschede, The Netherlands, February, 2011

SUPERVISORS:
Dr. V. A. Tolpekin
Ms Dr.Ir.W.Bijker

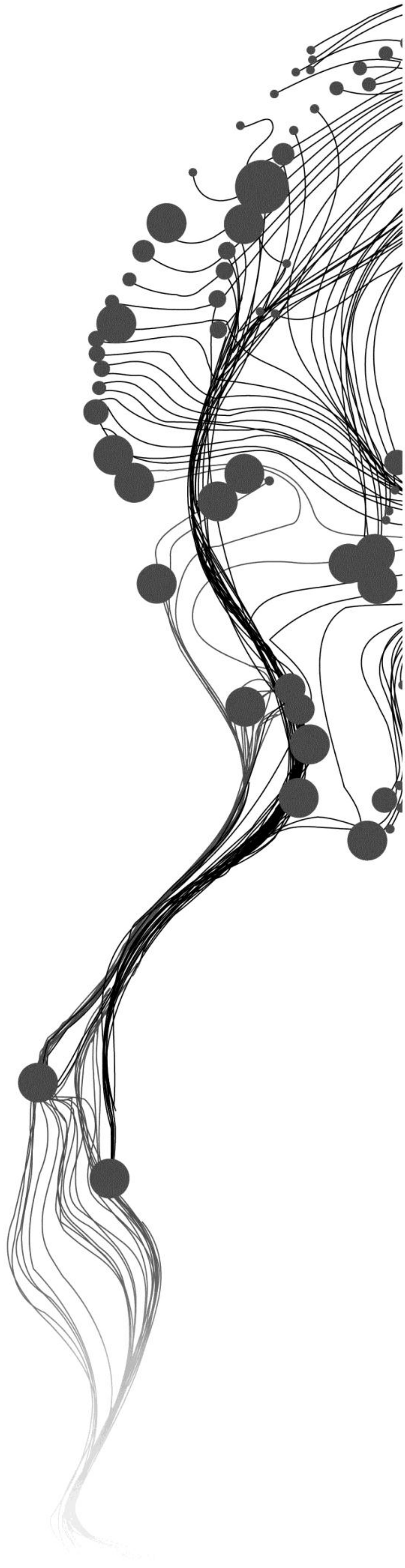

EFFECTIVENESS OF MARKOV RANDOM FIELD BASED METHOD FOR SUPER-RESOLUTION MAPPING IN IDENTIFYING SMALL LANDSCAPE ELEMENTS AND FOREST ENCROACHMENT FROM SATELLITE IMAGES

LAXMI KANT TIWARI
Enschede, The Netherlands, February, 2011

Thesis submitted to the Faculty of Geo-Information Science and Earth Observation of the University of Twente in partial fulfilment of the requirements for the degree of Master of Science in Geo-information Science and Earth Observation.
Specialization: Geoinformatics

SUPERVISORS:
Dr. V. A. Tolpekin
Ms Dr.Ir.W.Bijker

THESIS ASSESSMENT BOARD:
Chair: Prof.Dr.Ir. A. Stein
External Examiner: Dr.Ir. L.J. Spreeuwers, University of Twente

Dedicated to my Parents, Wife and Daughter

ABSTRACT

Small Landscape Elements (SLE) and Forests are major determinants of a landscape's identity and help to maintain ecological and environmental stability, play a key role in subsistence economy. However, little is known about SLE and their existence outside forests and few attempts has been done to study forest encroachment (FE) in the Indian scenario.

The present research was carried out to check the effectiveness of Markov Random Field (MRF) based Super Resolution Mapping (SRM) in the identification of SLE and FE. In this study ASTER image with spatial resolution of 15 m is used for all experimental tests. SLE identification is done at Buurserzand in the Netherlands, whereas, the study for identification of FE is performed at Rutland Island in India. This research work dealt with the real world problem by using real remotely sensed image.

Quality of SRM is compared with MLC classified map. The results of this study were validated using Google Earth image data. Simulated Annealing (SA) parameters were tuned on real data and result is compared with study done on simulated data before. Method parameter of MRF based SRM was evaluated on ASTER data. Accuracy was assessed at fine and coarse resolution using kappa statistics and error measures. It is observed that SRM outperformed MLC in case of fine and coarse resolution. Experimental test was done on the ASTER data to study the optimal neighborhood system size with respect to various Scale factor (S). It is found that resultant map of SRM was smoother than MLC due to resolution issue. This study dealt with Low resolution case in both study sites wherein object was bigger than resolution of pixel cell. Hence low accuracy was reported. Moreover, MRF based SRM is successfully identified SLE and FE at S = 2 by using ASTER image with spatial resolution of 15 m. Similarly, SRM result was successfully validated using Google Earth image.

This study provides guidelines for conducting similar research work by using MRF based SRM for identification of Tree resources outside forests (TROF) and other similar studies related with vegetation.

Key words: Markov Random Field, Simulated Annealing, Super Resolution Mapping, ASTER, Small Landscape Elements, Forest Encroachment, Root Mean Square Error, Google, Correlation Coefficient, Area Error Proportion, Scale factor (S), Fine resolution, Coarse resolution, Sub-pixel mapping, Maximum Likelihood Classification, Parameter Optimization.

ACKNOWLEDGEMENTS

At the very outset before thanking God I would like to express my sincere appreciation and deep gratitude to my first supervisor Dr. V. A. Tolpekin for his intelligent guidance, kind advice and constant support. I shall remain ever grateful to him. My sincere thanks goes to my second supervisor Ms. Dr. Ir. W. (Wietske) Bijker for her priceless guidance, constructive comments, recommendation and fruitful suggestion and help provided me to accomplish this study.

I would like to express my sincere gratitude to Professor George Vosselman for his constructive suggestions during research proposal. My deepest appreciation goes to Professor Alfred Stein, Chairman, Department of Earth Observation, ITC for his fruitful discussion and suggestion during my midterm review.

I would like to extend my thanks to Mr. Gerrit Huurneman, Course Director GFM for his moral support, encouragement and providing constructive suggestion during midterm review. I would take this opportunity to thanks Juan Pablo, Phd Scholar at Earth Observation Department for his help and suggestions provided in my research work.

I would like to express my gratitude to Hon'ble Lieutenant Governer, Andaman and Nicobar Islands to grant me study leave to undergo this study. I would like to thank immensely to the Principal Chief conservator of Forests, Andaman and Nicobar Islands for granting me permission to undergo this course. I would like to thanks European Commission for providing me scholarship to complete this course.

I would like to take this opportunity to offer my sincere thanks to all senior officers of Forest Department, Andaman and Nicobar Administration, Andaman and Nicobar Islands for their support and kind cooperation.

I will not be fair to forget my course colleagues for their co–operation during the entire period of the present course. I have every sense of gratitude to almighty God for his consistent support. Last yet not the least I would like to thank my respected parents, wife, daughter and other family members for their motivation, care, love and kind co–operation.

TABLE OF CONTENTS

LIST OF FIGURES

LIST OF TABLES

LIST OF ABREVIATIONS

$\boldsymbol{S}$	Scale factor
$\boldsymbol{T_0}$	Initial temperature
$\boldsymbol{T_{upd}}$	Temperature update
$\boldsymbol{\lambda}$	Smoothness parameter
$\boldsymbol{W}$	Window Size
$\boldsymbol{\kappa_{max}}$	Kappa maximum
$\boldsymbol{\kappa}$	Kappa statistic/kappa coefficient
$\boldsymbol{\kappa_{min}}$	Kappa minimum
ha	Hectare
MRF	Markov Random Field
SRM	Super resolution mapping
VHSR	Very high spatial resolution
GIS	Geographic Information System
GFW	Global Forest Watch
WRI	World Resources Institute
MLC	Maximum Likelihood Classification
AEP	Area Error Proportion
RMSE	Root Mean Square
CC	Correlation Coefficient
FE	Forest Encroachment
SLE	Small Landscape Elements
GRF	Gibbs Random Field
GCP	Ground control point
T D	Transformed Divergence
SA	Simulated Annealing

1. INTRODUCTION

1.1. Problem statement and possibilities

Detection and mapping of relatively small elements in a landscape, such as hedges, large individual trees and other Small Landscape Elements (SLE) in predominantly agriculture area, Trees Resources outside Forests (TROF) or cleared patches in a forested area i.e., Forest Encroachment (FE) is a big challenge due to the common problems i.e., to find something small relative to the spatial resolution of the image like objects belonging to, FE and SLE, which occupy small areas inside larger forests (in case of FE) or agricultural areas (for SLE). Some of these patches are even less than 0.5 ha. Limited contrast with background/surrounding landcover is another hurdle. Furthermore, the relatively coarse spatial resolution of sensors does not enable detection of all small wooded fragments such as copses, hedgerows and scattered trees(Sheeren et al., 2009). Studies have also shown that identifying and defining SLE is often not easy: which elements should be included and which should not, and how to describe elements discretely. A list of SLE with definitions was derived from a typology overview composed by Dijkstra et al. (2003). Another challenge remains in getting high spectral and spatial resolution satellite imagery for a particular area and within a specific period. If we use high resolution data, it will be noisier than coarse resolution data, high resolution data is too expensive and it requires costly hardware and software for its processing. When we do classification of spectrally similar vegetation types (e.g., Mangrove/Littoral/Evergreen) using coarse resolution data, we are getting mixed pixel results. It is difficult to study landuse/cover at high resolution data due to large variation of the spectral values for the same classes and local variation within homogeneous fields and it has few spectral bands than coarse resolution sensors (Tolpekin and Stein, 2009).

The possible solution for the above mentioned problem may be Markov Random Field (MRF) based super-resolution mapping (SRM). Identification of SLE has been previously carried out using aerial photography and remote sensing in the Netherlands. One major study objective within the framework of the Dutch Remote Sensing Programme and the landscape monitoring project 'MeetnetLandschap' was to investigate the added value of very high spatial resolution (VHSR) satellite data compared with digital topographical 1:10,000 maps and aerial photographs, especially in relation to SLE (Groom et al., 2006). However, this study and earlier studies indicated that many SLE such as solitary trees, hedges, old orchards have a low accuracy in topographic maps because of their lower priority compared with other topographic elements such as built-up areas and infrastructure and are therefore not consistently mapped. In that study, true colour aerial photographs, which cover the entire Netherlands for the year 2000, were compared with panchromatic and multi-spectral IKONOS satellite images from the same year(Groom et al., 2006). Medium and high spatial resolution remotely sensed data (e.g. SPOT and Landsat Thematic Mapper (TM) images) are mainly used to identify wooded areas. These data provide richer spectral information and cover larger areas (Sheeren et al., 2009). In the Netherlands, a landscape monitoring system, including detailed information of all small elements is lacking (Oosterbaan and Pels, 2007). A hybrid approach using both aerial photographs and ancillary data of coarser resolution to automatically discriminate small wooded elements by (Sheeren et al., 2009), shows its usefulness and the prospects for future ecological applications. Methodology for mapping non-forest woody elements using historic cadastral maps and aerial photographs as a basis for management is done by(Skalos and Engstova, 2010).

For proper management and evaluation of SLE and FE by the concerned authorities new remote sensing tool is needed for identification of SLE and FE. SRM can be effective because it result in a higher spatial resolution image from a given coarse spatial resolution image. Data from the satellite sensors like LANDSAT-TM, IRS-LISSIII, and ASTER are rich in spectral bands, economically cheap and a huge volume of archive data is available, which will help in detecting actual changes on the ground. Hence, by using these coarse spatial and high spectral resolution data as an input to SRM, it is possible to solve the issue of class separability. Various parameters in SRM will be analysed to arrive at optical values for extracting SLE & FE with high accuracy.

1.2. Research identification

Various studies have been carried out on the MRF based SRM, to check its suitability for landcover classification and change detection analysis. Whereas, only limited amount of SRM validation studies have been done. To the best of my knowledge no attempt has been made to study the effectiveness of MRF based SRM in identifying SLE and FE.

1.2.1. Research Objective

The main objective of this research is to apply technique for identification of SLE and FE using MRF based SRM described in Tolpekin and Stein (2009) and to validate the result.

1.2.2. Research Questions

In order to achieve the aforementioned objective the following Research questions were formulated

- How can fine tuning of Simulated Annealing parameters be achieved?
- What is the difference in the method for parameter setting for a case with real data compared to the use of simulated data?
- What are the major improvements in the optimal neighbourhood system in comparison to earlier simulations?
- What is the framework for quality assessment at multiple spatial resolutions?
- Does the object shape and size affect the quality of final SRM?

1.3. Research approach

The general approach of this research is shown in Figure 1.1, ASTER data is used as an input to the applied technique. Contextual SRM method based on MRF is adopted after preprocessing of ASTER image. Finally obtained result is checked for its accuracy on fine and coarse resolution level.

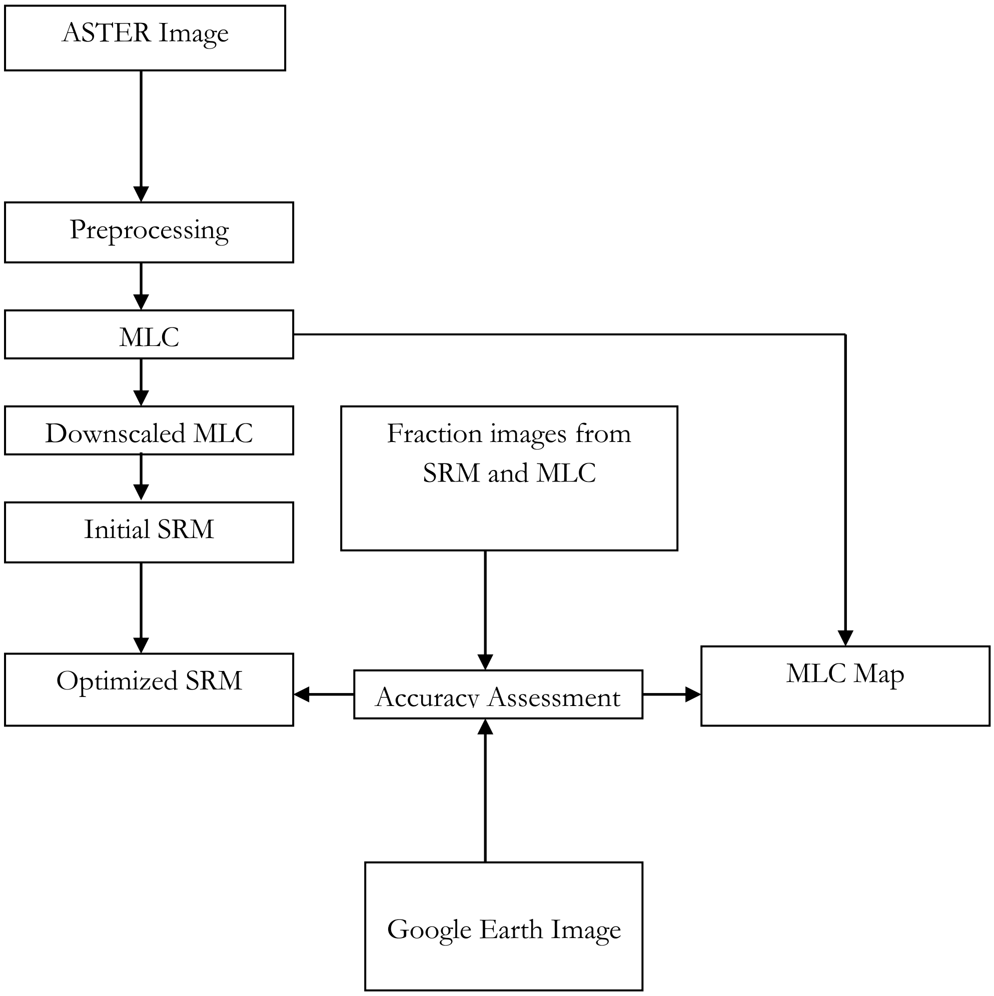

Figure 1.1 Research approach adopted for the study

1.4. Structure of the thesis

The first chapter provides introduction, problem statement and possibilities in detecting SLE and FE, research objective along with research questions and structure of the thesis. Chapter two presents the literature review done in this research. Chapter three discusses the study area and data sets used in this study. Chapter four describes methods adopted in this research. Chapter five presents results whereas chapter six deals with discussion. The last chapter describes conclusion and recommendations of this research work.

2. LITERATURE REVIEW

The available literatures were reviewed with respect to SLE, FE and SRM validation studies. In the past several attempts had been done to detect SLE and FE using remote sensing and Geographical Information System (GIS) technique. On the other hand, very few studies are done on validation of SRM. The main aim of this chapter is to build theoretical basis and review related work done on SLE and FE. There are various related work has been done to evaluate and examine SLE and FE on classification issues using remote sensing. The last section of this chapter describes studies on validation of SRM.

2.1. Studies on SLE

In the past several studies on landscape change analysis is found in the literature. These studies mainly concerned on the change detection i.e., landscape changes and distribution providing less emphasis on the land classification methods (Cousins et al., 2002; Herben et al., 2006; Hietel et al., 2005; Sklenicka and Lhota, 2002; Van Eetvelde and Antrop, 2004). Similarly, many studies have been done to identify non-forest wood elements (NFWE) by using old cadastral maps and aerial photographs (Bender et al., 2005; Domaas, 2007; Hamre et al., 2007; Vuorela et al., 2002).

SLE has been studied in the Netherlands by using IKONOS image, digital topographic map (Top10 – vector) and aerial photographs (Groom et al., 2006). Two study areas were selected, one in the province of Limburg and one in the province of Brabant. In the Netherlands, monitoring of SLE for large part obtained from the use of Top10 – vector maps and their updates. However, this study and earlier studies presented that many SLE such as hedges, old orchards and solitary trees have low accuracy in topographic maps. Since, digital topographic maps are cartographic product and therefore several SLE are simplified in their geometry. This study revealed that spatial variation such as in delineation, homogeneity, compactness and structure can only be derived from VHSR satellite image and true colour aerial photograph and not from Top10 – vector maps. True aerial photographs for the year 2000 were compared with panchromatic and multi – spectral IKONOS satellite images from the same year for the entire Netherlands, which is shown in Figure 2.1, in the next page. Furthermore, the distinction between landcover classes i.e., trees, dark shadow and waterbody was more easily performed on the IKONOS satellite images than true aerial photographs. In addition to that, IKONOS satellite images have more radiometric quality and it exhibits less geometric distortions in comparison to true aerial photographs. IKONOS satellite images cover a larger area (11 x 11 Km) in one scene than most of aerial photographs. This study suggested that with respect to classification there is need for re-examinations of the role of remote sensing image data in identifying SLE.

Monitoring of SLE in the Netherlands, this research work is done by (Oosterbaan and Pels, 2007), this monitoring system designed by using a digital database for SLE, proved to be practicable and can be carried out with the help of local volunteers. In this study field maps were prepared in GIS, showing all SLE from existing topographic maps and corrected/adjusted with aerial photographs, on a basis of polygons. The designed monitoring system was tried out in three areas with different landscape types.

(a) True colour aerial photograph, Eurosense, June 2000

(b) IKONOS panchromatic image, May 2000

(c) Top 10 vector (topographic map 1999)

(d) Field photo, taken from red arrow in (a)

Figure 2.1, Source: Groom et al. (2006)

Some studies have been reported on SRM of vegetation (Boucher et al., 2008; Thornton et al., 2006). The automatic detection of SLE, small wooded and thin linear elements in rural landscapes has drawn less attention. In (Thornton et al., 2006), Hedgerows and trees were successfully identified by using fine resolution satellite sensor imagery using super – resolution pixel – swapping. In earlier studies only one dimension of linear feature extraction was considered. Whereas, in the latter said study two dimensions i.e., width and length of linear feature extraction was successfully dealt with. Pixel swapping algorithm for sub – pixel mapping was applied to soft classified Quickbird satellite sensor with a spatial resolution of 2.6 m. Initially in the aforementioned study two sub – pixel algorithm namely Fuzzy c – means and Linear mixture model was performed. However, Fuzzy c – means outperformed linear mixture model. In (Tolpekin and Stein, 2009) it was found that Linear mixture model is not suitable for SRM. In (Thornton et al., 2006), Fuzzy c – means algorithm was performed to obtain fraction images, on this, pixel – swapping algorithm was applied to get SR map at Scale factor $(S) = 5$. In addition to that mathematical morphology was used to overcome error in the output of sub – pixel mapping in order to yield enhanced overall accuracy.

By using methodology called image segmentation, edge extraction and linking, edge grouping and matching, and verification with Digital Surface Model (DSM), (Zhang et al., 2006) extracted the SLE (namely tree rows and edges). A hybrid approach using both aerial photographs and ancillary data of coarser resolution to automatically discriminate small wooded elements by (Sheeren et al., 2009), which shows the results in usefulness of the hybrid approach and the prospects for future ecological applications.

In (Ardila Lopez et al., 2010; Tolpekin et al., 2010) urban tree crown have been identified using MRF based SRM from VHSR satellite Images. Contextual SRM method based on MRF presented in (Tolpekin and Stein, 2009) used to retrieve tree crown objects from VHR satellite images i.e., Quickbird images(Tolpekin et al., 2010), the novelty of this study is that it incorporates information from panchromatic band. This study was done in residential area. Result obtained in the aforementioned study can be combined with other vector data in a GIS. The proposed method used in the said study is based on posterior probability modelling and in this way it allows to compute the posterior probabilities for all landcover classes by using fuzzy membership as demonstrated in Bijker et al. (2010), analysis of the post probabilities values allows us to convert the classification results into fuzzy membership.

MRF based SRM for identification of urban trees in VHSR images (Ardila Lopez et al., 2010) based upon the SRM as implemented in Tolpekin and Stein (2009) on synthetic normally distributed multispectral images. In this study, the initial point for SRM was obtained from the maximum likelihood classification (MLC) of the multispectral bands and MRF was implemented in C^{++} program and parameter estimation was done by trial and error method whereas pixel based accuracy assessment was performed for accuracy.

Methodology for mapping non-forest wood elements using historic cadastral maps and aerial photographs as a basis for management is developed by (Skalos and Engstova, 2010). This study was based on old cadastral maps (from 1839 to 1843), black and white aerial photographs (from 1938, 1950, 1966, 1975 to 2006) and provides a method for making a detailed analysis of NFWE oriented towards future state, and analysis of the long term dynamics. In addition to that several categories of NFWE were considered:

- NFWE inside the village.
- Scattered vegetation in the open landscape.
- Scattered vegetation along roads.

The above said method can be used for all types of study sites, irrespective of landscape size or type. However, the detailed classification system is most efficient when it is used for rather small territories. This study dealt with only quantitative changes, no qualitative analysis has been done. This paper suggested that change in Non-forest wood vegetation can be considered as permanent landscape structure and any alteration taking place in the latter said vegetation can be regarded as change in the whole land cover. In this research SLE (small group of trees) comes under scattered vegetation in the open landscape will be studied.

2.2. Studies on FE

In (Abdulkadir-Sunito and Sitorus, 2007), two forest – margin villages Sulawesi in Indonesia is presented to clarify the scenario of FE. Here encroachment is not only perceived as an economic action, but also an arena of ethno – political action, it also explained how encroached ownership is changed. This paper describes land - use and landownership patterns in the context of inter - ethnic relationship.

FE is studied by using optical and microwave image fusion to detect and monitor illegal logging and tropical rain forest encroachment in east Kalimantan, Indonesia (Vega et al., 2006). In this paper it is reported that the output classifications from Principal component analysis (PCA) were relatively better than other two techniques used. Comparison was made between the results of MLC and sub – pixel classification to identify gaps made by a single tree felling and it was observed that sub – pixel classification outperformed MLC. It is suggested that if the remote sensing techniques, combined with the appropriated classifiers, demonstrated better performance and reliable results.

In (Vega, 2005), three remotes sensing fusion techniques using two different data combinations i.e., multi-spectral and Panchromatic from Landsat ETM; and multi-spectral and Radar data from ASAR-ENVISAT C band VV polarization were studied for FE monitoring. However, this study shows that the fused images obtained from multi-spectral and panchromatic data were more appropriate with exception of Intensity-Hue-Saturation created some confusion during interpretation.

FE was detected in the mount makiling forest reserve by using intergrated remote sensing and GIS technologies by (Panaguiton et al., 1999). This study suggested that by integrating several images intrusion of encroachers into the forest land can be detected. It could be a nice tool for decision makers and forest managers who are involved in the forest conservation making plans.

In (Saleh et al.), use of satellite data and GIS in monitoring of Indonesia forest cover is highlighted wherein quick evaluation of forest cover was done by the integrating approach of GIS and low resolution satellite data i.e., SPOT4 (SPOT – Vegetation) and Landsat ETM^{+}. The classification method used in this study was MLC, fuzzy and fuzzy knowledge based classification. The latter mentioned third method gives the best result to assess forest cover in that study.

(Baranga, 2007) studied the FE at Mabira forest reserve in Uganda to investigate the different activities carried out in the reserve and to assess how these affect its conservation status. This study was performed by systematic sampling technique and interview. This study suggested that FE occurs due to illegal timber logging, wood extraction for domestic and commercial purpose and further he concluded that FE may be stopped by Joint Forest Management Programme (JFM) wherein residents who are residing near to forest areas should be trained about importance of forest and environment, once awareness with respect to save forest is developed in public then automatically they will participate in safeguarding the forest.

In (Minnemeyer, 2002), Global Forest Watch (GFW): Mapping and Monitoring is dealt with various forest management issues which includes illegal timber felling and encroachment. To address the various aspects of forest mapping and monitoring the World Resources Institute (WRI) developed GFW in the year 1997. The main objective of GFW is to bring transparency and accountability in the forestry sector, through independent monitoring of forests and forest management practices. GFW is an international organisation consisting of 75 non - governmental, academic and scientific institutions in ten countries. GFW is tracking information by using GIS and remote sensing tools.

Deforestation related issue was studied in (Stone et al., 1991)where coarse satellite imageries were used to detect forest loss and cleared patches inside the forest. The various other works on forest cover monitoring, deforestation and FE is found in (Hirota, 2003; Rosenqvist, 1996; Walker)

2.3. Studies on validation of SRM

This section presents literature review related with studies on validation of SRM.

In (Tatem et al., 2002b) SR map was produced by using Hope field neural network. In this study the SRM was implemented on synthetic and simulated Landsat TM imagery and it was validated by verification data derived by ground survey and manually prepared map from the digital aerial photographs with 0.5 m spatial resolution. Sub pixel mapping was obtained by using genetic algorithm in (Mertens et al., 2003) here the latter mentioned algorithm was tested on synthetic and degraded real satellite imagery. The resultant SR map was compared with conventional hard classification i.e., Maximum Likelihood Classification (MLC) for the purpose of accuracy assessment.

In another study SR mapping was performed on artificial imagery and tested on artificial and real synthetic imagery (Mertens et al., 2004). In this study validation of SRM was conducted with MLC map. An algorithm was developed for super - resolution target mapping from remotely sensed images in which was dependent on soft classification results (Atkinson, 2005). This algorithm was tested for its accuracy by generating realistic irregular polygon shape in SPLUS ™ software. Earlier SRM was applied on real remote sensed satellite data in (Kasetkasem et al., 2005). In this study SRM was obtained from IKONOS and

LANDSAT imageries validated with reference data generated from panchromatic image of IKONOS and digital aerial photograph with spatial resolution of 1 m and 2 foot respectively.

In (Thornton et al., 2006) sub-pixel mapping was conducted for identification of hedgerows and trees and the resultant map was validated with Field data (Differential Global positioning system) including the detailed information available on the field site. Issues associated with SRM reveals that validation of SRM is not easy (Atkinson, 2008). However, this study paves the way for accuracy assessment by providing different types of accuracy assessment methods.

SRM was conducted on normally distributed synthetic images in Tolpekin and Stein (2009). In this study accuracy assessment was done by kappa statistics at fine resolution level and accuracy at coarse resolution was assessed by Area error proportion (AEP), Root Mean Square (RMSE) and by using Correlation Coefficient (CC). In subsequent studies (Ardila Lopez et al., 2010; Tolpekin et al., 2010) which were extension of method proposed in the (Tolpekin and Stein, 2009) validation of SRM was assessed by using ground survey followed by manual digitization of VHSR, digital aerial photographs digitization and they also performed pixel and object oriented based method for accuracy assessment.

So far, SRM has been used mainly in experimental datasets or particular study cases. Although, the accuracy of all methods of SRM has been tested, most of them are based on synthetic or experimental datasets. Only limited validation of SRM have been done with real available fine resolution data.

In, (Atkinson, 2009) it is suggested that it is very crucial to determine the goal of SRM in terms of its dimension i.e., whether it is binary or multivariate and resolution case (i.e., L – resolution or H – resolution or lies in between them). After knowing the latter said aspects algorithm is designed and applied to provide as solution. The SRM algorithm falls into two categories. The first contains regression-type algorithms and another one is learning algorithms. The four testing scenarios which involves in assessing uncertainty are provided in (Atkinson, 2009) next step is adopted which is described in the latter said paper for accuracy assessment wherein four different types of accuracy assessment methods are mentioned.

2.4. Summary

But still there is need to do further research on SLE on FE. In the latter said cases MRF based SRM is not used to study the SLE and FE. Hence, this will be new research of its kind. The pertaining literature with respect to FE is reviewed and it is found that in most of the cases FE was detected with the integrated approach of using remote sensing and GIS tools. Some of the papers on FE cited above discussed their results on the basis of systematic sampling and interviews whereas few of them were discussed forest management i.e., JFM and their sustainability. From afore mentioned literature it is revealed that there are two forms of FE i.e., shifting cultivation and Illegal logging. In this research we are going to identify FE sites wherein shifting cultivation and residence is found. This research is not dealt with illegal logging in FE. Last not the least section of this chapter describes some previous studies done on the validation of SRM.

3. STUDY AREA AND DATASET

3.1. Study area – 1

Buurserzand: Buurserzand is located in the region south east of Twente close to the border of Germany, in the province of Overijssel in the Netherlands. It is geographically situated between $52^{\circ}09'00''$N latitude and $6^{\circ}48'00''$E longitude. The area lies in the municipalities Haaksbergen, Berkelland and Enschede. It is property of the Natuurmonumenten foundation (Nature Monuments). The Buurrserzand is rich of heath land forests and pools. It is managed by Non Gazetted Organization (NGO) Natuurmonumenten. It is a heath land zone that was used in the past for sheep grazing. It accounts for 800 ha and it is one of the last sites of its type in Western Europe. For that reason it receives ample support from the International community. The main purpose of the reserve is the maintenance and restoration of rare plants for national cultural heritage. Several plant and animal species are preserved here. Study for identification of SLE will be conducted in this Study area.

Sustainable development and optimal management of forests and SLE is an essential ingredient of socio-economic development of a region. SLE consists of terrestrial and smaller aquatic ecological elements, such as trees, shrubs, lines and clusters of trees and ponds. Forests and SLE have fundamental value for the landscape and its historical development. In the past SLE played an important role in different land use systems (Oosterbaan and Pels, 2007).

A clear understanding of the mutual interdependencies of various natural phenomena is a prerequisite, to provide necessary inputs for developing a cost effective energy efficient, environmentally friendly system. The remote sensing technology has emerged as an important tool for identifying the natural resources rapidly as the satellite data provides the best synoptic input, about the forests, SLE and the dynamic change over time and space. Remote sensing can make a substantial contribution management flows from the unique characteristics that remote sensing data provide-repetitive, quantitative, and spatially explicit capabilities. Furthermore, remote sensing is the best and perhaps only possible way to do temporal and large-scale mapping of forested area and the SLE outside forests. Remote sensing gives quantitative and qualitative information about forests and SLE. Through satellite data, it is possible to identify the forest cover broken down to density classes and the other land cover classes accurately. The remote sensing satellite data therefore has become very handy for stratifying the forests into homogenous sections which make the field inventory efficient, accurate and cost effective.

Data set

ASTER Image

ASTER (Advanced space born Thermal Emission radiometer) is a joint Japan – US imager deployed on NASA's Terra platform. Each scene of ASTER covers an area of 60×60 Km. ASTER is an optical sensor which covers a wide spectral region from the visible to the thermal infrared by 14 spectral bands (ERSDAC, 2010). The first three VNIR bands with 15 metres spatial resolution were used in this research to identify SLE. Spatial characteristics of the ASTER image is mentioned in the below shown Table 1.1. The acquisition date for the ASTER image was 12th September, 2006 and it covers Twente Region.

Band	Wavelength (μm)	Resolution (m)	Swath Width (km)	Revisit time (days)
Band1(VNIR)	0.5-0.6	15	60	16
Band2(VNIR)	0.63-0.69	15	60	16
Band3N(VNIR)	0.76-0.86	15	60	16
Band3B(VNIR)	0.76-0.86	15	60	16

Table 3.1. Details of ASTER Image, source: ITC Geodata warehouse

Google Earth Image

Google Earth Image (Google, 2011) acquired on 21st September, 2006 was used for generating reference data. Digital aerial photograph with spatial resolution of 0.50 m was used by Google Earth for mapping Buurserzand on 21st September, 2006. However, type of sensor and company providing the imagery was known from the copyright given in the Google Earth image but acquisition data for digital aerial photograh is not known. The date indicated above is obtained from Google Earth image. Accuracy assessment was done by κ at fine resolution and AEP, RMSE and CC at coarse resolution of the classification results obtained in study area – 1.

3.2. Study area – 2

Rutland: The Andaman and Nicobar are a group of picturesque Islands, big and small, inhabited and uninhabited, a total of 572 islands, islets and rocks lying in the South Eastern Part of the Bay of Bengal, in India. They lie along an arc in long and narrow broken chain, approximately North – South over a distance nearly 800 kms. . It is logical to presume a former land connection form Cape Negris at South part of Myanmar to Achin Head (Cape Pedro) in Andalas (Sumatra). The flora and fauna of these islands, however, indicate that this land connection if it existed should have been prior to the development of their present life form. Rutland Island (Study area – 2), Andaman and Nicobar Islands, India is located between latitude $11^{\circ}28'00''N$ to $11^{\circ}20'00''$ N and longitude $92^{\circ}35'00''E$ to $92^{\circ}45'00''E$. It lies in the District of South Andaman in the Union Territory of Andaman and Nicobar Islands. Rutland Island bears a unique stunted formation of southern hilltop forest dominated by Dipterocarpuscstatus (with an average height below 10 metres). It occupies an area of 14027.52 ha. Highest peak in Rutland is Mount Ford – 435 meters. The Rutland Island is the storehouse of many interesting plant species. Because of mass level of forest extraction activities in the past, vast stretch of evergreen forest is converted into secondary evergreen forest. FE will be studied in this Study area.

Illegal capture of forest land by felling natural trees of forest for cultivation/plantation and residential purpose is termed as FE. It leads to deforestation and change in forest types which causes deterioration of ecological balance.

Immediately after independence, the Govt. of India passed a Cabinet Resolution during 1952 approving rehabilitation of 4000 agriculture families by the end of 1st five – year plan and clearance of 20,000 ha of land for paddy cultivation in Andaman and Nicobar Islands. The Scheme of rehabilitation continued till seventies. Initially all such lands earmarked for settlement of refugees in the islands were covered with dense natural tree/forest cover.

Being an undulating terrain flat portion of the allotted land was intended for paddy cultivation while adjoining hilly lands to be made use of raising plantation crops. Conversion of land use from forest to non

–forest (agriculture, horticulture) was done. Hence, commercial trees were removed by the Forest Department of the Andaman and Nicobar Administration. And thereafter allottee was to clear the remaining jungle growth to develop the land for paddy cultivation or plantation crops.

Due to sudden raise in the population in A & N Islands during 1970 there was enormous pressure for livelihood and FE took places in remote areas where there was no communication or other means of facilities in a concealed manner. Since there was no staff posted in remote/interior locations and lack of communication and lack of political will, the forest encroachments were continued till 2000.

In the absence of proper communication facilities/shortage of staff/lack of protection to staff who are engaged for anti-encroachment duties/lack of political will/lack of proper focus on forest encroachments etc. many parcel of forest were encroached by the settlers, retired mazdoors and inhabitants.

Data set

Aster Image

In the Study area – 1 ASTER image was used for studying FE, first three VNIR bands with spatial resolution of 15 metres were used. The acquisition date for the latter said satellite image was 23rd February, 2006.

Google Earth Image

Google Earth Image (Google, 2011) acquired on 1st March, 2006 was used for generating reference data for this study area. Quickbird imagery with spatial resolution of 60 cm was used by Google Earth for mapping Rutland Island on 21st September, 2006. However, type of data and company providing the imagery was known from the copyright given in the Google Earth image but acquisition data for Quickbird data is not known. The date indicated above is obtained from Google Earth image. Accuracy assessment was done by κ at fine resolution whereas AEP, RMSE and CC are used at coarse resolution of the classification results obtained in study area – 2.

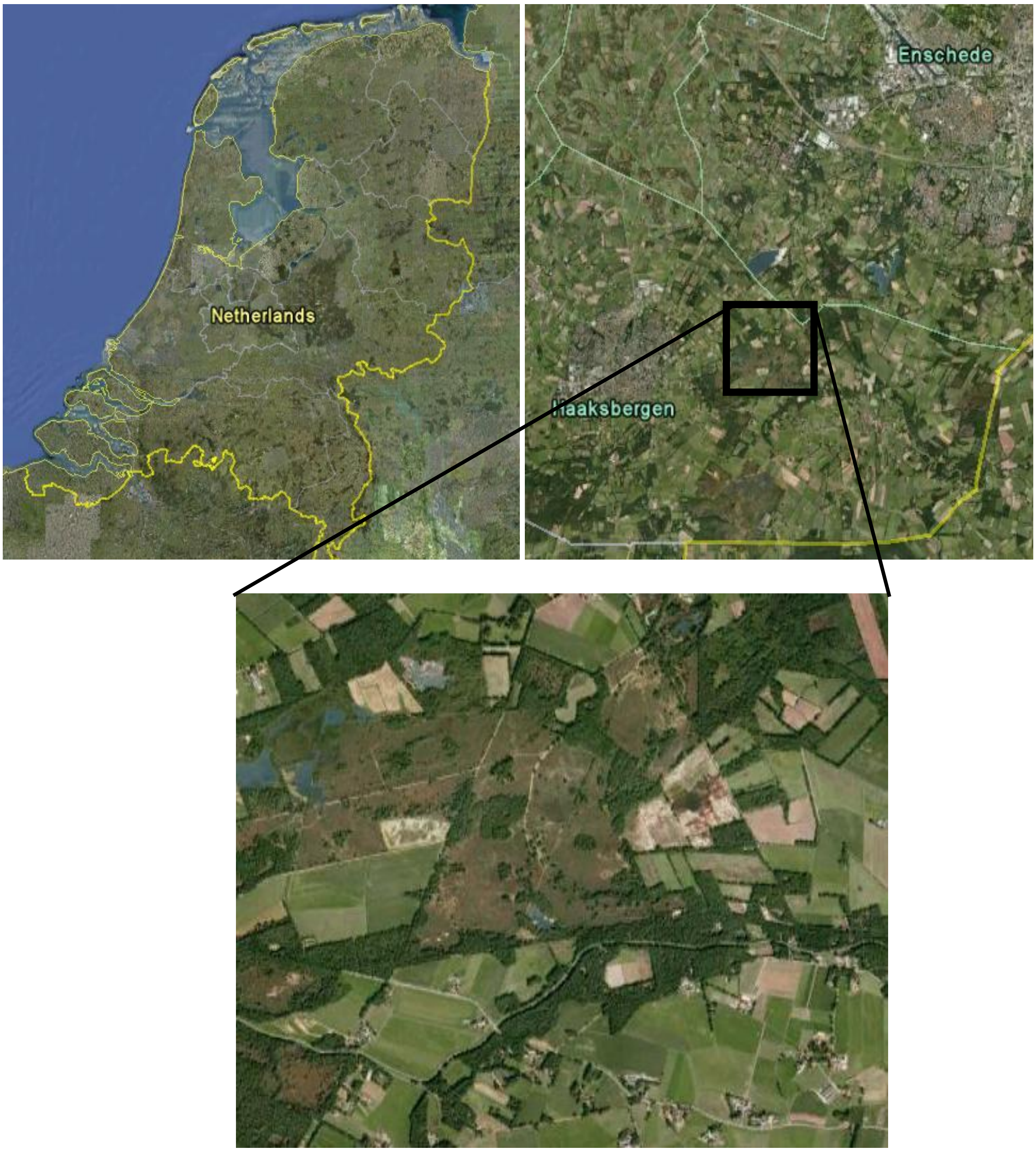

Figure 3.1. Study area – 1, Source: Google Earth

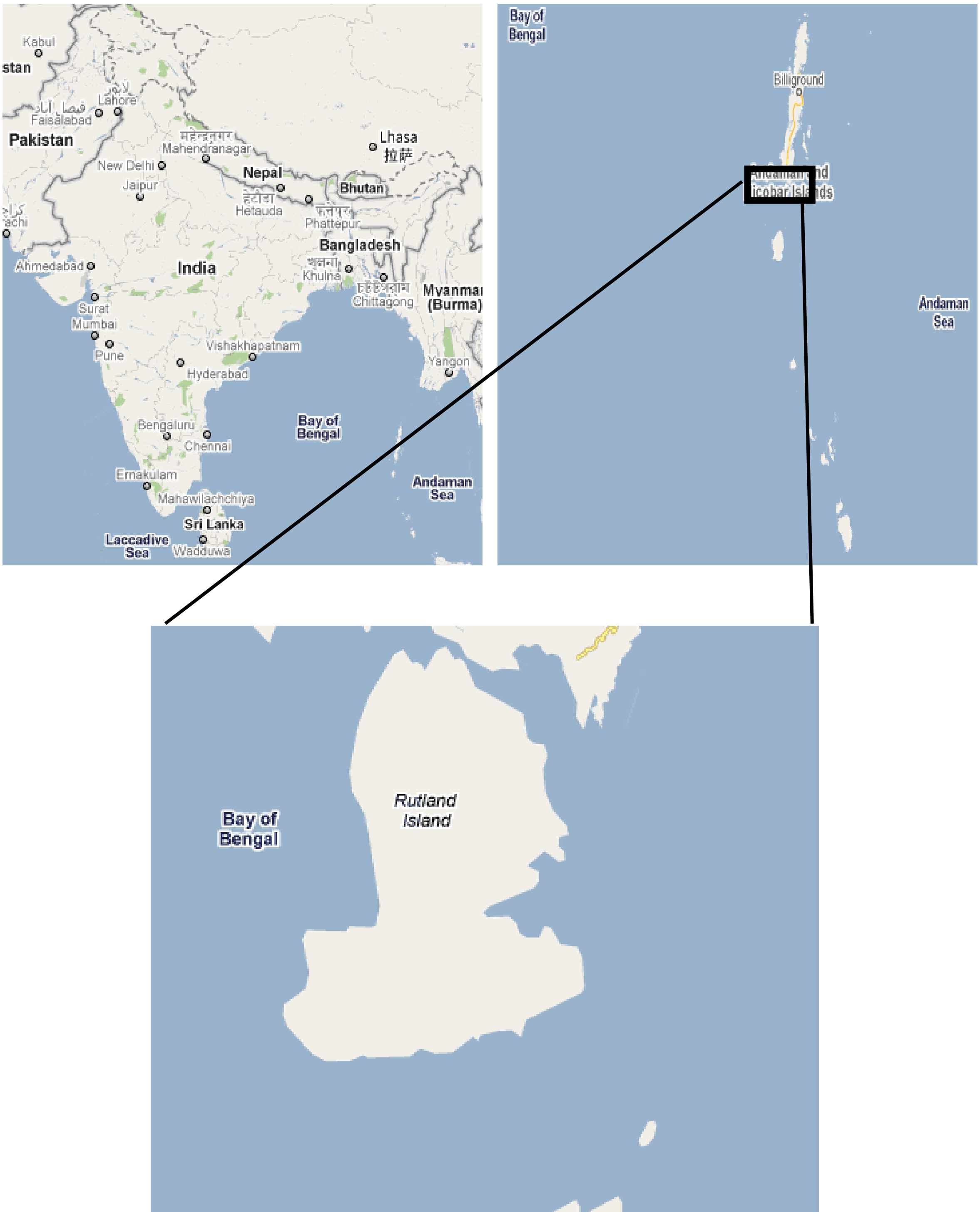

Figure 3.2. Study area – 2, Source: Google Map

4. METHODS

This chapter describes the methods used in this research. Section 4.1, presents preprocessing of ASTER and Google Earth data, wherein data import, image co – registration, GCPs selection, resampling and evaluation of the co – registered image data is dealt with. Section 4.2 deals with destriping of an ASTER Level 1 A data. Section 4.3 describes selection of Spectral classes and defining their training sets whereas section 4.4 describes reference data creation from Google map image. Section 4.5 presents approach of the study. Section 4.6 draws attention on class statistics whereas section 4.7 presents Maximum Likelihood classification (MLC) method and section 4.8 deals with Super resolution mapping method. In the section 4.9 MRF based SRM is explained. Section 4.10 presents MRF and Gibbs Random field (GRF). Sections 4.11 and 4.12 describe Estimation of Smoothness and Simulated Annealing parameters and their optimization. This chapter is ended with section 4.13 where accuracy assessment for this study is described.

4.1. Preprocessing

4.1.1. Importing data

Initially ASTER data was provided in HDF - EOS format, the standard format for all EOSDIS Core system (ECS) products (Erdas, 2010). The ASTER dataset was imported from HDF format into .img format as a file media using ERDAS IMAGINE software. After importing the first three VNIR bands of ASTER image it was layer stacked in the Erdas imagine software. No correction parameters were applied during the import, in order to avoid resampling during further analysis in SRM.

4.1.2. Image co-registration

Satellite Images in their raw form contain geometric distortions. ASTER data was provided in Geographic (lat/long) coordinate system with map units in degrees and seconds. Since UTM coordinate system has less distortion. Hence, ASTER data projection was altered to UTM with WGS 84 North spheroid and datum, Zone number32. It was given pixel size as 15 m by 15 m. In this research image co-registration process was performed by registering the Slave image with the Master image, where ASTER data was considered as Master and Google map image as Slave. It is the process in which the two images are made to match each other properly. When doing the image co - registration, it is generally preferable to register the lower resolution image to the higher resolution image, i.e., the high resolution image is used as the Reference Image. (Erdas, 2010). However, in this research reverse process was performed meaning Google Earth image used as slave and ASTER image had been used as master image. The latter said process was done to avoid resampling of ASTER Image. Since altered geometry and spectral value of the pixels are influencing the SRM. Hence, in order to preserve the original DN values in the pixels of ASTER image, resampling is not performed in this step. Therefore, Google map image was co-registered with ASTER image. The aforementioned image co-registration was accomplished in the following below mentioned steps:

4.1.3. GCPs Selection

The precision of geometric correction depends on the ground control points (GCPs). GCPs should be established precisely otherwise the images don't match to each other. The GCPs was put in specific location which can be found in two images easily like: Tri junction of road, bent of creeks and sharp corner of the identifiable unique ground features. The GCPs were scattered all over the image but more densely in the working area so that it makes the image matching properly at that area. 1st order Polynomial transformation was used. The projection chosen was UTM with WGS84 North spheroid and datum, Zone 32. The Root Mean Square Error (RMSE), which is the distance between the input location of the GCP and the resampled location of the same GCP, was about 0.2 pixel for study area – 1. In the case of second study area 2nd order polynomial transformation was used and it was resampled into UTM projection with WGS84 North spheroid and datum, Zone 46 by using Nearest Neighborhood resampling technique. The RMSE was about 0.3 pixel.

4.1.4. Resampling the image

Resampling is the method in which the pixel values of the input image are assigned to pixels in the output grid. Resampling of the image leads to change in DN values, contrast, brightness and geometry of the pixels. Three methods are used to do resampling of the slave: Nearest Neighbour Interpolation, Bi-linear Interpolation and Cubic convolution. Since Nearest neighbourhood assigns the value of the nearest pixel in the input image to pixel in the output image. This is mainly suited for use with classified data. Hence, in this research Nearest Neighbour Interpolation method was used for resampling reference image.

4.1.5. Evaluation of the Co- registered image

Accuracy checking of image co-registration was done by using viewer swipe in ERDAS IMAGINE. The swipe tool slowly works its way over the images allowing one to evaluate the quality of the co-registration. Both horizontal and vertical directions were examined. Some features like creek, tri junction of road and other identifiable objects which were present in the slave image tallied with the master image by using swipe tool and it was found that in slave image they were matching properly in terms of shape, size and location.

4.2. Destriping of Aster Image

In this research ASTER level 1 A image data is used after destriping. The method followed for destriping the aforementioned image is adopted from (Van Ede et al., 2004). Furthermore striping in satellite images is caused due to defective, out of alignment and improper calibaration of sensors. There was some striping present in the VNIR bands of ASTER data, which causes in rows and columns in the image that deviate from neighbouring rows and and columns and can affect subsequent processing. Hence, ASTER image used was destriped in order to remove the striping artifacts from the image data for further analysis. Usually destriping of Landsat data is done either in Envi or Erdas softwares which contain horizontal strips. In ASTER level 1 A image data vertical strips were found and corrected.

Direct destriping was done in Envi and Erdas and observed that resultant output was not better. Hence method followed by (Van Ede et al., 2004) was performed for destriping of ASTER image. Firstly ASTER data was imported from HDF-EOS format in .img format without correction. In order for better execution of destriping algorithm, the striping in the image should thus have a horizontal orientation. In addition to that VNIR sensor use an array of sensor perpendicular to the flight direction, possible striping from miscalibrated sensor will occur in a vertical orientation, and not horizontal as in Landsat images. Hence, image needs to be rotated before applying a destriping algorithm therefore it was rotated by 90 degrees. After completion of import and rotation, actual destriping can be done. Different sensor is used for every column of the image (4100 sensors for VNIR, 2048 for SWIR, 700 for TIR), the number of sensors for destriping was set to 2 as suggested in Van Ede et al. (2004). Furthermore after carefully examination of the destriped images from Envi it is observed that still some strips were present. Hence, they were again destriped with the desriped utility of Erdas. The resultant images are shown in the Figures 4.1 and 4.2, displayed in the next page.

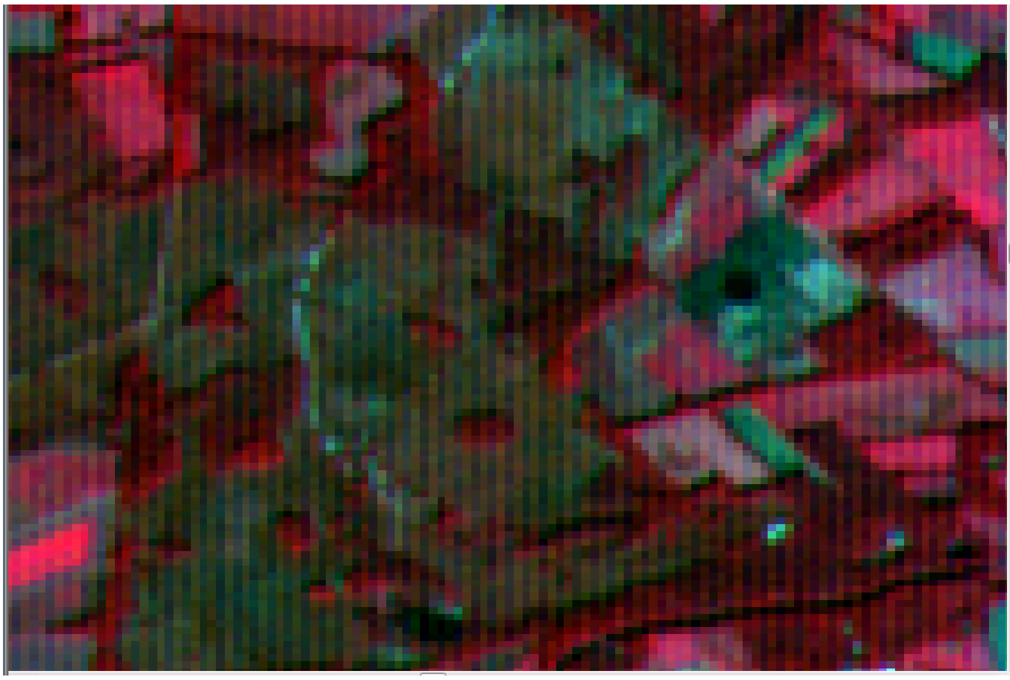

Figure 4.1 Before destriping, level 1 A image data of ASTER Sensor

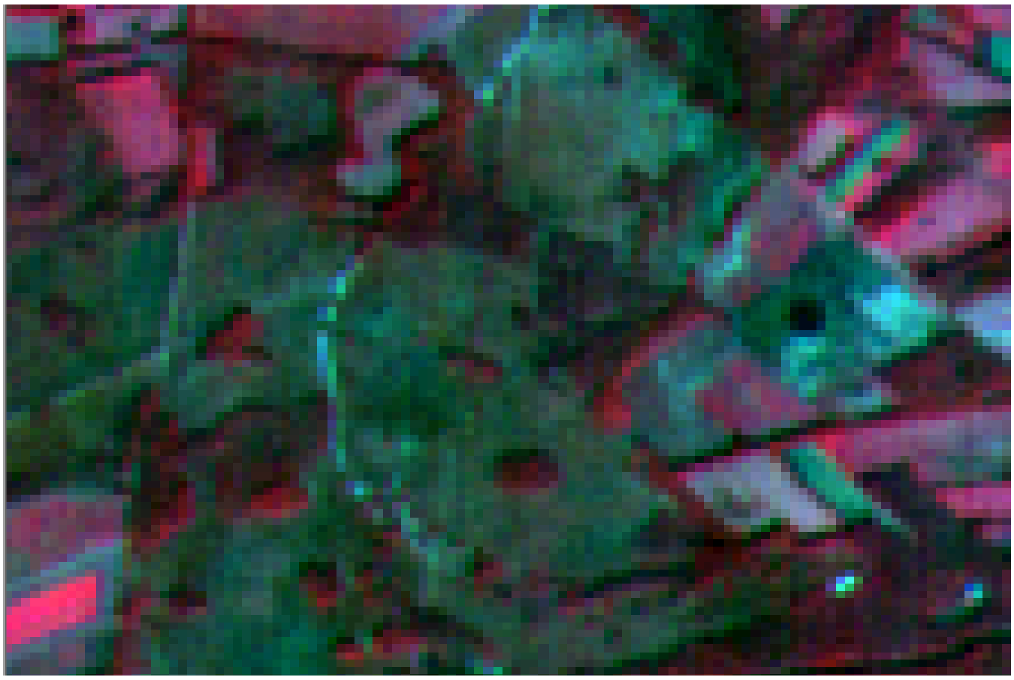

Figure 4.2 After destriping, level 1 A image data of ASTER Sensor

4.3. Select Spectral classes and defining their training sets

Several training sets have been taken to produce single training set. For study site – 1 four landcover classes were selected. In addition to that for each of these landcover classes a training set was defined for estimation of class mean and covariance for the ASTER image by using Envi software. In order to avoid overfitting of the method to the data of the study area Global training set were taken from a larger ASTER scene outside the study area, which is shown in appendix (A). Only four land cover classes i.e., heath, baresoil, waterbody and trees with their mean and covariance in the ASCII format were considered for running SRM algorithm for identification of SLE in the study area – 1. Class separability was also considered between the selected land cover classes and was determined by Transformed Divergence (T D) which is added in the appendix (A).

In the study area – 2, three landcover classes namely forest, waterbody and encroached_area (mixed landcover class) with their mean and covariance were taken. Class separability was determined by T D method, it is appended in the appendix (A)

4.4. Reference data generation

For accuracy assessment reference data is needed. Hence, reference data was generated by manual digitization of high resolution data i.e., google map image in Arc Gis software and exported to .tif format on the subset extension parameters i.e., output coordinates and processing extent. Furthermore, the latter said format was exported to ASCII file by using ENVI Software. Therefore, pixels achieved by manual digitization of digital aerial photograph for Study area – 1 and from Quickbird data in case of study area – 2 obtained from Google earth image. After vectorization and rasterization they were used for the accuracy assessment. The latter said method was adopted in (Ardila Lopez et al., 2010; Tolpekin et al., 2010) for generating reference image for identification of tree crown from residential areas. Hence, the above mentioned method was followed to generate reference data for both study sites in this research. The ground reference image generated from visual interpretation of the Google earth image (digital aerial photograph with spatial resolution 0.50 m) for the study area – 1 whereas Google earth image with 0.60 m resolution was used for producing reference data for study area – 2. The reference data generated for study area – 1 is shown below in Figure 4.3.

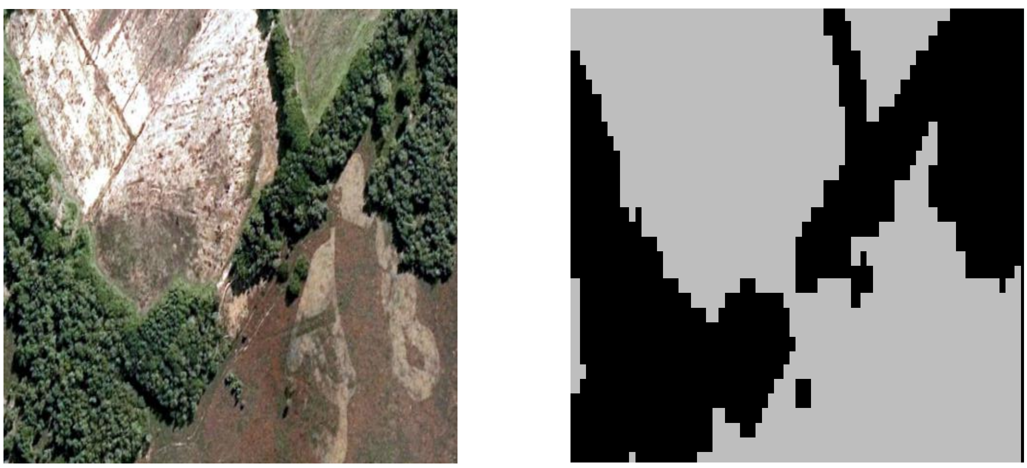

Figure 4.3 Ground reference image at 0.50 m spatial resolution of Buurserzand area

4.5. Proposed approach for the study

The below mentioned figure shows the overall approach used for assessing the effectiveness of MRF based SRM in identifying SLE and FE from satellite images. Firstly, the effectiveness of the latter said technique is assessed on the ASTER image for identifying SLE, for the study area – 1 explained in the forthcoming sections. Consequently, the technique shown in the Figure 4.4, is used for identifying FE, for the study area – 2. The technique used in this research is explained step by step in the coming sections.

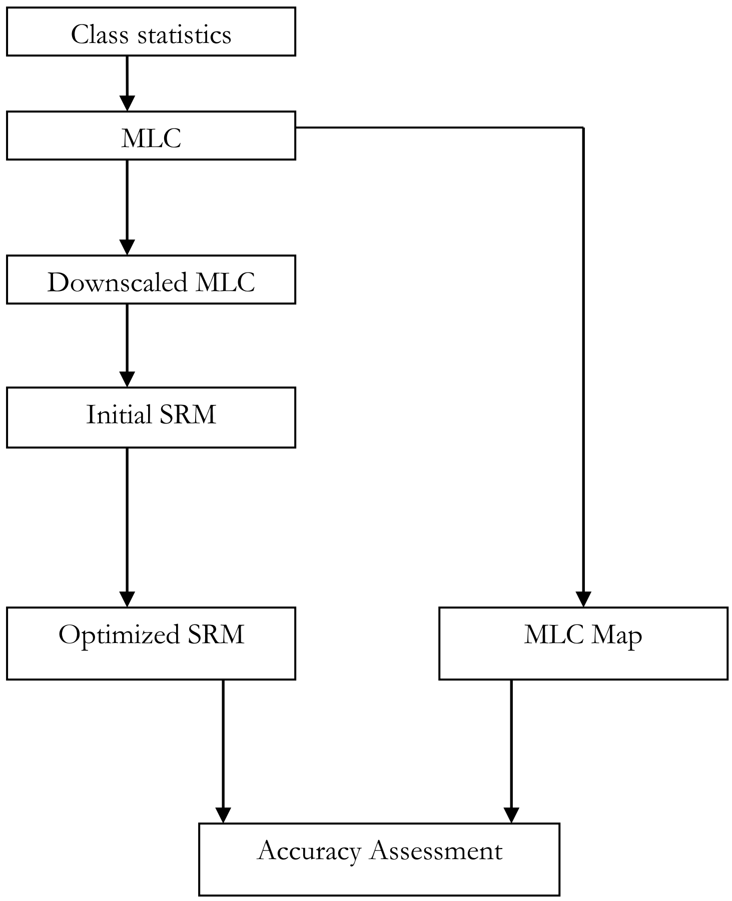

Figure 4.4 Flowchart for methodology

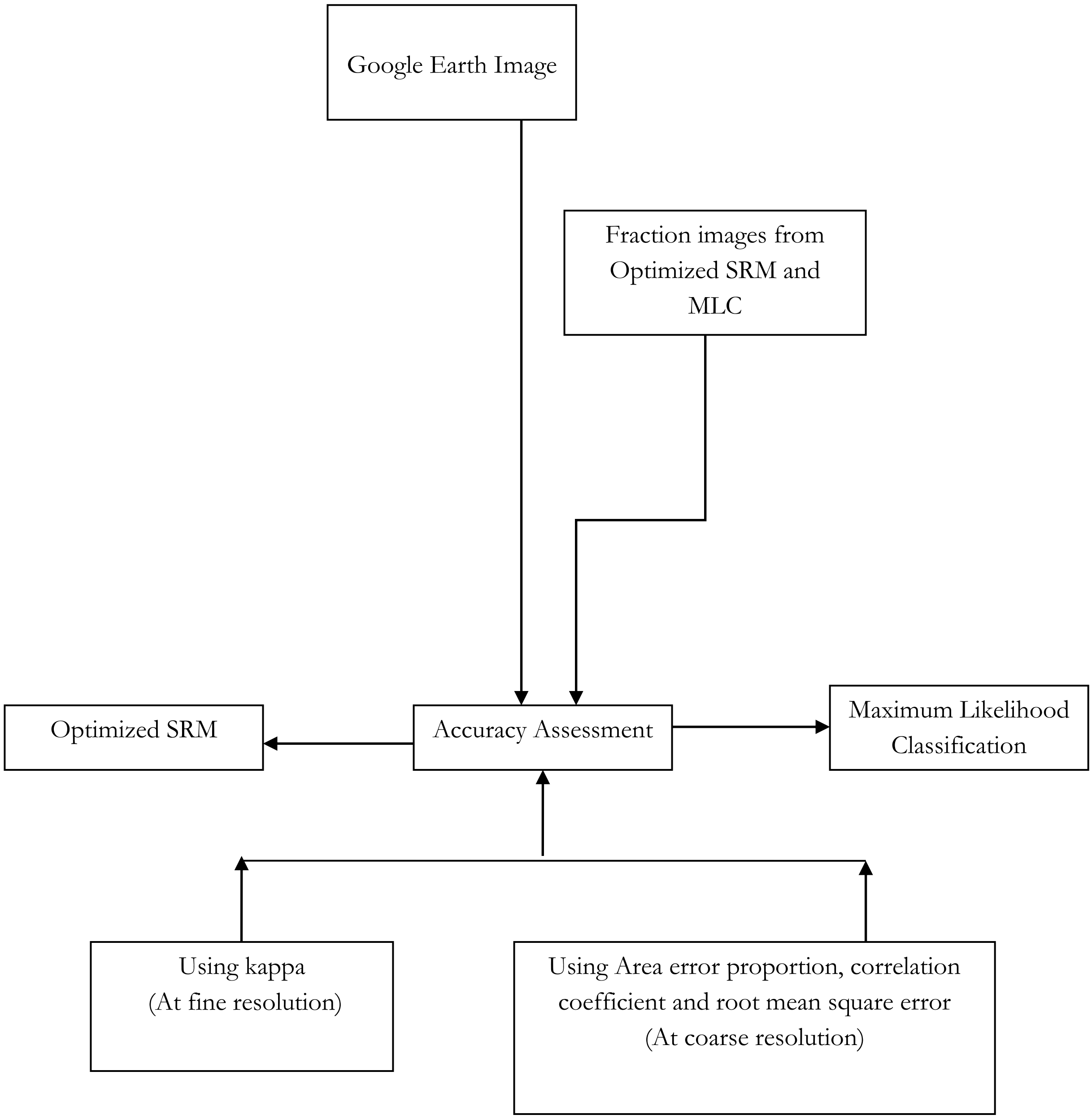

Figure 4.5 Flow chart for accuracy assessment

4.6. Class Statistics

We need to find mean vectors and covariance matrices for all landcover classes which are used by both SRM and MLC methods as an input in their classifying process. Pure pixels (containing only one land cover class) are used to estimate mean and covariance matrices, which is not easy to get in the coarse resolution image like ASTER data. If we select training pixels with similar spectral properties then it is under representing the class variance then it leads to confusion between classes. For low class separability, MLC and SRM lead to confusion between classes. However, T D is used in this research to calculate the separability between the landcover classes. It is assumed that observed image i.e., ASTER remotely sensed data is normally distributed with mean and covariance matrices.

4.7. Maximum Likelihood Classification (MLC)

MLC decision rule is based on the probability that a pixel belongs to a particular class. The basic equation assumes that there probabilities are equal for all classes, and that the input bands have normal distributions. It is a parametric decision rule and it assumes that the observed measurement vectors obtained for each class in each spectral band are normally distributed (Gaussian). This rule uses the statistics (mean, covariance of the pixels in the training sample). MLC uses the variance and covariance in class spectra to determine classification scheme. We can determine a probability that a given digital number (DN) is a member of each class. The pixel is classified by using the most likely class. It is based on Bayesian probability formula:

$$P(x, w) = P(w|x)\, P(x) = P(x|w) P(w) \tag{4.1}$$

Where x and w indicates events. $P(x, w)$ represents the probability of coexistence of events x and w. $P(x|w)$ and $P(w|x)$ are conditional probabilities. If event X_{i} is the i[th] pattern vector and W_{j} is information class j then, according to equation (4.6), the probability belongs to class W_{j} is given by

$$P(W_{\mathrm{j}}\, |X_{\mathrm{i}}) = \frac{P(X_{\mathrm{i}}\, |W_{\mathrm{j}}) P(W_{\mathrm{j}}\,)}{P(X_{\mathrm{i}})} \tag{4.2}$$

Where, $P(W_{\mathrm{j}}\, |X_{\mathrm{i}})$ is posterior probability, $P(X_{\mathrm{i}}\, |W_{\mathrm{j}})$ indicates conditional probability, $P(W_{\mathrm{j}}\,)$ is prior probability and $P(X_{\mathrm{i}})$ in general assumes to be normally distributed.

4.8. Super resolution mapping (SRM)

The problem of mixed pixel in the remotely sensed satellite data occur when the sensor's instantaneous field-of-view includes more than one land cover class on the ground and it can be accommodated by using sub-pixel classification, which provides class proportions or fractions. The key problem of sub-pixel classification is determining the most likely locations of each land cover class within the pixel. In general, Spatial dependence is the phenomenon that observations close together are more alike than those further apart (Chiles and Delfiner, 1999; Curran et al., 1998). Hence, an approach to consider the spatial distribution i.e., spatial dependence within and between the pixels was introduced by Atkinson et al. (1997) in the form of SRM also called as sub-pixel mapping, they attempted sub-pixel mapping with three techniques. However, they obtained most appropriate result with a neural network. SRM leads to an increase in the spatial resolution of the classified image by resolving the pixel into smaller units, known as sub-pixels, based on spatial dependence (Thornton et al., 2006). In SRM we obtain fine resolution thematic map from given multi spectral remotely sensed data. It is also a land cover classification technique (Tolpekin and Stein, 2009).

SRM approach is based on the phenomenon of spatial dependency. It is assumed that the landcover class are normally distributed and they have spatial dependency both within and between the pixels. To have a more clearity on a spatial dependency and example indicating problem and solution is provided in Figure 4.6, for further details interested readers may refer to (Atkinson, 2009). The S equals the ratio between the pixel size in the input and output images. In the below mentioned Figure 4.6 (a), coarse resolution image with 3×3 grid, with associated proportions of one land cover class is shown. After applying the S of five, it is divided into 25 sub pixels, which is shown in Figure 4.6 (b). In Figure 4.6 (c), each sub-pixel has 4% coverage of the coarse resolution pixel and it exhibits the possible alignment of sub-pixels, in which the spatial distribution is enhanced, both within and between the coarse resolution images.

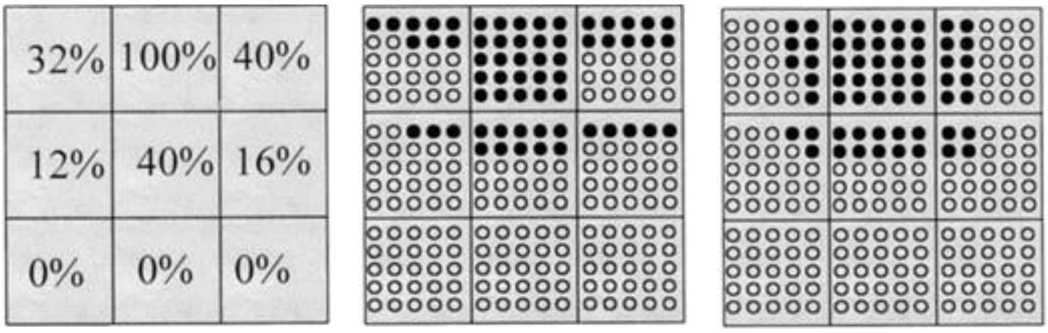

(a) (b) (c)

Figure 4.6 Super resolution mapping, Source: (Atkinson, 1997)

Many SRM techniques have been reported in the literature. A comprehensive introduction to SRM is given in Atkinson (2004a) and Tatem et al. (2002b). In Atkinson (2004b) Super-Resolution land cover classification is obtained using soft classification i.e., mixture model as a input with the two-point histogram method.

Hopfield neural network was used by Tatem et al. (2002a,b) to predict the location and patterns of sub-pixel classes. After the successful implementation for features larger than a pixel (Tatem et al., 2002b), their method was extended to determine the spatial pattern of sub-pixel scale features (Tatem et al., 2002a). A genetic algorithm for sub-pixel mapping was developed by Mertens et al. (2003) they obtained higher accuracy measures compared with conventional hard classification. In the latter said algorithm optimization involves expert knowledge, which is one of its demerits. Mertens et al. (2006) provide spatial attraction model for SRM. They reported enhanced accuracy when compared to hardened soft classifications. A pixel-swapping algorithm for sub-pixel mapping assisted by mathematical morphology was developed to soft classified fine spatial resolution remotely sensed imagery in Thornton et al. (2006).

In, (Atkinson, 2009), SRM approaches are divided into two categories: regression or learning algorithms, which include geostatistical models, and spatial optimization algorithms, such as pixel swapping, Simulated anneaing (SA) and Hopefield neural network. Furthermore most of the algorithms under SRM approaches are dependent on other technique for their soft classification results. Hence, their SRM result is limited by the sub pixel classification technique used. Some of the algorithms (Mertens et al., 2003; Tatem et al., 2002a, 2002b; Verhoeye and De Wulf, 2002) are dependent on another technique to accomplish sub-classification on the given input image. Whereas the algorithm provided by (Kasetkasem et al., 2005) neither relies on the availability of accurate boundary features nor on sub-pixel classification from other sources. It is based on MRF model based algorithm, described in the coming section. In one of the major findings in Tolpekin and Stein (2009) it is found that the error in the sub-pixel classification result can be corrected in SRM.

In this research MRF-based contextual SRM method described in Tolpekin and Stein (2009) is used for checking the effectiveness of MRF-based SRM in identifying SLE and FE from satellite Images. The latter said study method was used in (Ardila Lopez et al., 2010; Tolpekin et al., 2010) for extraction of urban tree crown objects form VHR satellite images which leads to object identification.

4.9. MRF based SRM

This section presents concept of MRF – based SRM. Earlier (Solberg et al., 1996) developed MRF – based SRM for image classification and change detection using multi-source data. MRF is a useful tool for characterizing contextual information and has been widely used in image segmentation and restoration. MRF models have been used ranging from statistical physics, medical sciences to remote sensing. MRF model favours and assigns more weightage to homogeneous regions of landcover classes than heterogeneous regions of landcover classes i.e. isolated pixels.

Context can be obtained by different dimensions: spectral, spatial or temporal. Spectral dimension refers to the different bands of the electromagnetic spectrum, which helps in classifying landcover classes more accurately. In another words it can be said that contextual information is very much needed while doing MRF based SRM. The second dimension considers adjacent pixels in the spatial neighborhood. The third dimension temporal refers to temporal aspects of the multitemporal image of the same area for doing change detection. Hence, it is obvious that context plays crucial role in solving possible ambiguities, the recovery of missing information and the correction of errors (Tso and Mather, 2009). MRF is a part of Bayesian probability theory, where two key elements i.e., prior density function (p.d.f) and conditional p.d.f combine together to provide Bayesian classification formula. After combination of prior and conditional p.d.f maximum a posterior (MAP) criteria is established. MAP is popularly known criteria in MRF modelling (Kasetkasem et al., 2005; Li, 2009; Tso and Mather, 2009)

Let y be a multi spectral remote sensing image containing K spectral bands obtained from satellite sensor and the pixel locations are denoted as $\mathrm{b_i} \in \mathrm{B}$, where B is the pixel matrix with size M X N. The super-resolution map (SR map) c is defined on a set of pixels A, which covers the same area on the ground as B, it has finer resolution. Image resolution is denoted as R, i.e., each pixel is assumed to correspond with a square a on the ground of size R^2. R and r represents coarse and fine resolution respectively. The goal in SRM is to obtain c from y. S=R/r and it is assumed that S will be an integer. Each pixel $\mathrm{b_i}$ represents to the area on the ground covered by S^2 fine resolutions of $\mathrm{a_{j|i}}$where $\mathrm{j} = 1, \dots S^2$. This will result in pixel matrix size $(S\mathrm{M}) \times (S\mathrm{N})$. It is assumed that image x has same number of spectral bands as y but it has finer resolution than image y and x is not observed directly. An assumption is made that the pixels of matrix A which contains in image x can be assigned to a unique class, therefore $c(a_{j|i}) = \alpha$, where $\alpha \in \{1,2, \dots, L\}$

The relation between x and y is built by a degradation model, where y can be treated as degraded version of x. The degradation model for the image y and x is mentioned below:

$$y(b_i) = \frac{1}{S^2}\sum_{j=1}^{s^2} x\left(a_{j|i}\right) \tag{4.3}$$

Symmetric neighborhood $N(a_{j|i})$ is introduced on A, which is obtained from image x. the symmetric neighborhood can be defined as set of pixels inside a square window where a_j pixel is located at the centre of the window, excluding itself.

The window size W, being the length of one side completely defines the neighborhood, that's why the amount of pixels at the edges differs. The neighboring relationship properties of are described in (Li, 2009). In (Li, 2009) neighborhoods are defined in terms of order. First – order and second – order neighborhood corresponds to four and eight closest pixels. The latter neighborhood systems are the most popular ones. Furthermore, window size of $W = 3$ and corresponds to second order neighborhood system. Similarly, fifth- order neighborhood system with a Window size of $W = 5$ will contain twenty four pixels which are shown in Figure 4.7.
A clique is defined as subset of pixels. It came from graph theory. The amount of cliques are dependent on the size of the window, if window is large then it will accommodate more amount of cliques. Cliques contain either single pixel, pair of pixels, a triple pixels and quadruple pixels and so on. However, it is noted that when the order of neighborhood system increases it leads to increase in amount of cliques, which causes computational complexity. In Figure 4.8 (a), cliques for neighborhood system 1 are shown. Cliques associated with neighborhood system 2 are shown in Figure 4.8 (b).

5	4	3	4	5
4	2	1	2	4
3	1	x	1	3
4	2	1	2	4
5	4	3	4	5

Figure 4.7 Neighborhood order up to 5 sharing a side with the given pixel.

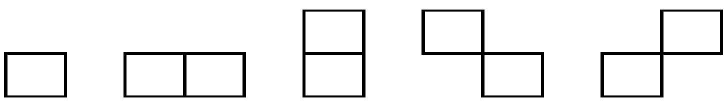

(a) Cliques for first neighbourhood order

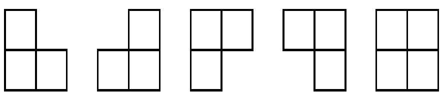

(b) Cliques for second neighbourhood order
Figure 4.8 Cliques for different neighbourhood order

In this research neighborhood for different size are tested on the real data set of ASTER image, which is performed in the section 4.13.

4.10. MRFs and Gibbs Random Fields (GRF)

In order to model the SR map c as MRF, it needs to satisfy the following properties (Li, 2009):

- Positivity $\mathrm{P(w)} > 0$ for all possible configurations of w,
- Markovianity: $\mathrm{P(w_r|w_{s-r}) = P(w_r|w_{Nr})}$, and
- Homogenity: $\mathrm{P(w_r|w_{Nr})}$ is the same for all sites r.

The first property says that the joint probability of the class is always positive. This allows to determine the joint probability by the local conditional probabilities and it can usually be satisfied in practice, and the joint probability P(w) can be uniquely determined by local conditional properties as long as the positivity property sustains (Besag, 1974). Markovianity indicates the labeling of a site r is only dependent on it neighboring sites. The third property i.e., Homogenity specifies the conditional probability for the label of a site r, given the labels of the neighboring pixels, regardless of the relative position of site r in S (Tso and Mather, 2009).

When these properties are satisfied. The prior probability for SR map is represented by $p(c)$, the conditional probability that image y is observed, given the true SR map c as $(y|c)$, and the posterior probability for SR map c is indicated by $P(c|y)$. However, a GRF provides a global model for an image and the MRF is equivalent with GRF because of Hammerley- Clifford theorem (Tso and Mather, 2009)above mentioned probabilities can be formulated by means of energy functions (Geman and Geman, 1984). The formulation of MRF Theory described below is adapted from (Tolpekin and Stein, 2009) with some minor changes.

$$P(c) = \frac{1}{Z_\mathrm{p}} \exp(-U(c) \,/\, T) \tag{4.4}$$

$$P(y|c) = \frac{1}{Z_\mathrm{l}} \exp(-U(c) \,/\, T) \tag{4.5}$$

$$P(c|y) = \frac{1}{Z} \exp(-U(c|y) \,/\, T) \tag{4.6}$$

Where Z_p , Z_l, Z are normalizing constants, T is a constant termed temperature. $U(c)$ indicates prior energy function, $P(y|c)$ is likelihood energy and the posterior energy of S R map is given by $P(c|y)$

The relation between the conditional probabilities can be related with Bayes theorem by

$$P(c|y) \; \alpha \; P(c)P(y|c) \tag{4.7}$$

On rewriting the above equation (4.7) for energy functions

$$U(c|y) \;=\; U(c) + U(y|c) \tag{4.8}$$

As per the equation (4.4) the prior energy can be formulated by the below mentioned equation where prior energy is considered as the sum of pair – site interactions (Li, 2009)

$$U(c) = \sum_{i,j} U\left(c(a_{j|i})\right)$$

$$= \sum_{i,j} \sum_{l \in N(a_{j|i})} w(a_l) \cdot \delta\left(c(a_{j|i}), c(a_l)\right) \tag{4.9}$$

Where, $U\left(c(a_{j|i})\right)$ is the local contribution to the prior energy from the pixel $c(a_{j|i})$, $w(a_l)$ represents the weight of the contribution from pixel $a_l \in N(a_{j|i})$ to the prior energy, and $\delta(c_1, c_2)$ if c_1 and c_2 are same i.e., $c_{1=}c_2$ then it provides value of 0 otherwise 1 is obtained. Hence, $w(a_l)$ is model as

$$w(a_l) = q \cdot \varphi(a_l) \tag{4.10}$$

In the above equation (4.10) $\sum_{l \in N(a_{j|i})} \varphi(a_l) = 1$ and $0 \leq q < \infty$

If value of q is lower than it gives noisy images whereas, if the value of q is higher than it leads to smoother solutions.

It is assumed that the observed image y consists of mixed pixels and it contains normally distributed landcover classes. Furthermore, we assume that values x are spatially uncorrelated given their class association. Under the assumption of absence of spatial correlation of the spectral values, the likelihood of $y(b_i)$, given $c(a_{j|i})$, is given by

$$P(y|c) = \prod_{i,j} P\left(y(b_i)|c(a_{j|i})\right)$$

$$= \prod_{i,j} \frac{1}{2\pi^{k/2}|C_i|^{1/2}} \times \exp\left(-\frac{1}{2}(y(b_i) - \mu_i)' \;\; C_i^{-1}\left((y_{b_i}) - \mu_i\right)\right) \tag{4.11}$$

Then corresponding likelihood energy then equals

$$U(y|c) = \sum_{i,j} U\left(y(b_i)|c(a_{j|i})\right)$$

$$= \sum_{i,j} \left[\tfrac{1}{2}(y(b_i) - \mu_i)' C_i^{-1}(y(b_i) - \mu_1) + \frac{1}{2} \ln|\mathrm{C_i}| \right] \tag{4.12}$$

Where $U\left(y(b_i)|c(a_{j|i})\right)$ is the local contribution to the likelihood energy from the pixel $c(a_{j|i})$

$$U(c|y) = q \cdot \sum_{i,j} \sum_{l \in N(a_{j|i})} \varphi(a_l) \cdot \delta\left(c(a_{j|i}), c(a_l)\right) + U(y|c) \tag{4.13}$$

The Equation (4.13) indicates a maximum a posteriori (MAP) probability solution for the SRM problem (Geman and Geman, 1984) on normalization done in (Tolpekin and Stein, 2009) Equation (4.13) can be written as:

$$U(c|y) \alpha \lambda \sum_{i,j} \sum_{l \in N(a_{j|i})} \varphi(a_l) \cdot \delta\left(c(a_{j|i}), c(a_l)\right) + (1 - \lambda) U(y|c) \tag{4.14}$$

Where $\lambda = \frac{q}{(1+q)}, 0 \leq \lambda < 1$ and λ represents smoothness parameter and controls the contribution from the prior and likelihood energy in the posterior energy.

4.10.1. Energy Minimization:

After obtaining global energy, the next step was to determine solution i.e., the energy needs to be minimized of (4.14) with respect to c. Several minimizing algorithms have been reported in the literature. The three algorithms, known as Simulated Annealing (SA) (Geman and Geman, 1984), Iterated Conditional Modes (Besag, 1974) and Maximize of Posterior Marginals (Marroquin et al., 1987) . All three algorithms are iterative in nature. In this research we adopted the SA algorithm to determine maximum a posteriori (MAP) solution. Results obtained in (Geman and Geman, 1984; Hailu Kassaye, 2006; Kumar Bist, 2009; Sikazwe, 2007; Tso and Mather, 2009) show that the SA provides best result if tuned carefully. It is a type of stochastic iterative optimization technique which is based on the use of random numbers and probability statistics for the global minimization problem. In SA the starting point should be close to one of its local minima. SA uses a cooling schedule which decreases the temperature T in an iterative way. The cooling schedule can be expressed by

$$T_{(\mathrm{t})} = T_0 . T_{\mathrm{upd}} \tag{4.15}$$

This procedure is controlled by two annealing parameters T_0. and T_{upd} (Besag, 1974) where $T_{(t)}$ is any temperature value depending on the i[th] iteration. T_0 is the initial temperature and controls the randomness of the optimization algorithm. High temperature defines more randomness and low temperature yields low randomness. For instance if SA algorithm started at high temperature T_0.

$$U(w_{\mathrm{r}} | d_{\mathrm{r}}, w_{\mathrm{Nr}}) \tag{4.16}$$

In the equation (4.16) in the previous page d_{r} is observed pixel, w_{r} denotes unknown pixel and w_{Nr} resembles neighboring pixel. Here we will use pixel iteration and examine new pixel value, which is generated randomly i.e., it is new random number. After that we compute post energy with old and new values i.e., U_1 and U_2 if it gives minimum value then it is negative and we accept the old one i.e., $U_2 < U_1$ and if the new value is greater than old one and greater than zero then accept the new one.

The iteration was repeated three times for each temperature update value. If there is no alteration in the three iterations the algorithm was permitted to terminate the process. In SA algorithm convergence occurs when the number of iterations approaches infinity, which is its disadvantage. Furthermore, the downscaled MLC result obtained from multispectral image y, where all subpixels $a_{j|i}$ corresponding the pixel b_i were assigned to the same land cover class was used for the initial estimate of c.

4.11. Estimation of the Smoothness parameter

Smoothness parameter (λ) plays an important role in MRF based SRM and it is estimated before method can be applied. Generally λ is determined by two procedures i.e., by trial and error method or by estimation done from training sites. At one hand first procedure is time consuming on the other hand second procedure is computationally expensive. In this research the internal parameter of MRF based SRM is firstly estimated by trial and error method and it is compared with the procedure developed in Tolpekin and Stein (2009). The experiment for λ estimation is done in the below mentioned paragraph

This experiment was conducted on subset of ASTER data with dimension 12×12 in order to save processing time; it presents estimation of optimal λ and its range at S i.e., 2, 3, 4, 5, 6 and 10. At each S optimal and range of λ were identified. The results are shown in the Figures, 4.9 and 4.10. The resultant Tables for the Figures 4.9 and 4.10 are attached in the appendix (B). Although, standard deviation was small, identification of optimal values of λ was not easy. Hence, optimal value $\hat{\lambda}$ that results into the largest mean Kappa value i.e., $\kappa_{\max}$. In addition to that, for the criterion of closeness to the maximum value we choose $\kappa \geq 0.9\kappa_{\max}$ (Tolpekin and Stein, 2009). λ, range represents the optimal range of λ values where κ is above 90% of $\kappa_{\max}$ is shown in the Table 4.1.

S	λ	$\kappa_{\max}$
2	0.7 – <u>0.9</u> – 0.95	0.70776 ± 0.01905
3	0.7 – <u>0.85</u> – 0.95	0.70497 ± 0.01262
4	0.6 – <u>0.7</u> – 0.99	0.68893 ± 0.01344
5	0.6 – <u>0.8</u> – 0.95	0.71106 ±0.0199
6	0.5 – <u>0.7</u> – 0.9	0.69583 ± 0.02125
10	0.4 – <u>0.6</u> – 0.8	0.67449 ± 0.01944

Table 4.1 $\kappa_{\max}$ indicates the maximal value and the standard deviation of κ. λ indicates the λ range where number in the underline is $\hat{\lambda}$.

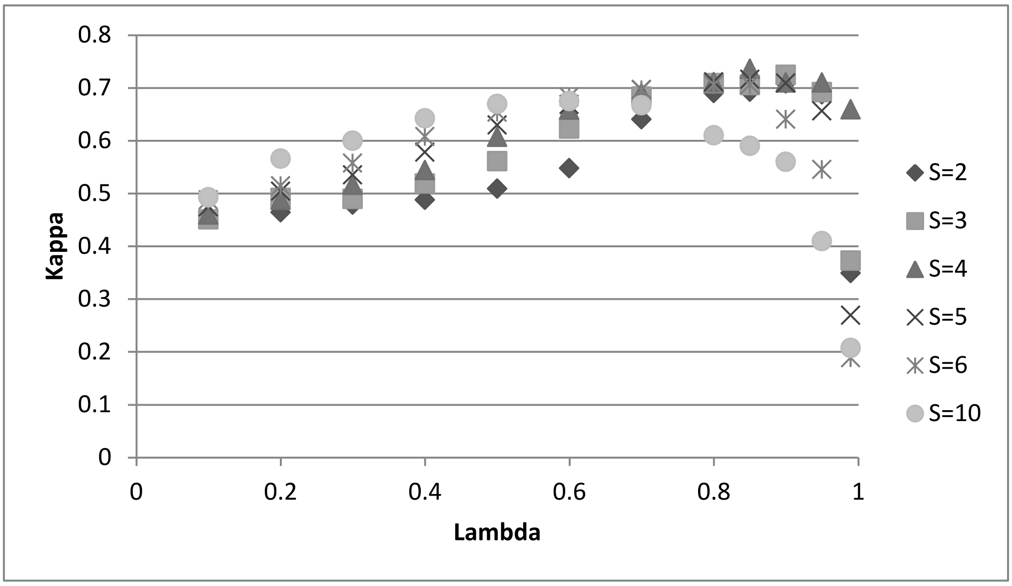

Figure 4.9 kappa (κ) at varying lambda(λ) values

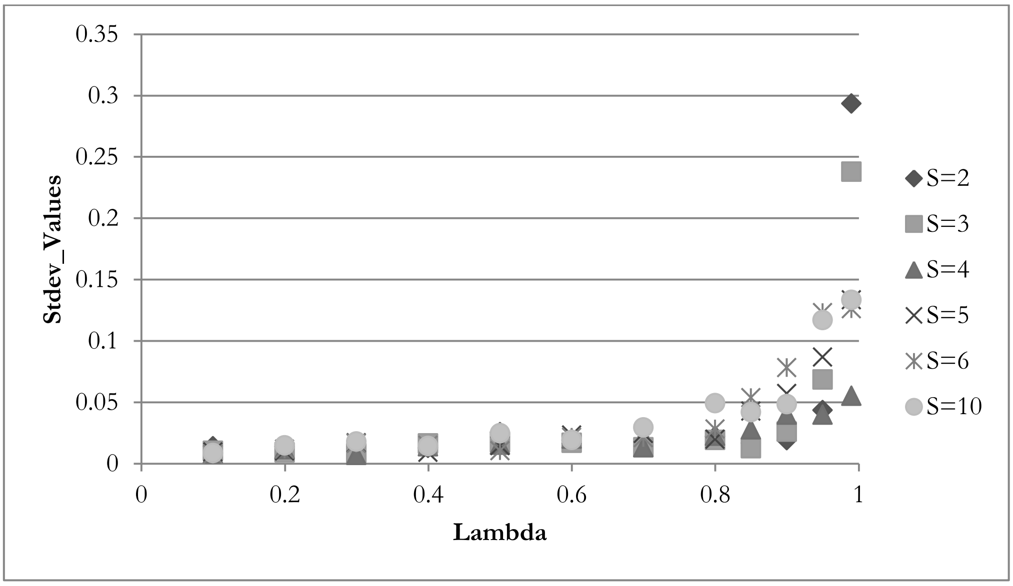

Figure 4.10 Standard deviation of lambda (λ)

4.12. Optimization and Estimation

Initial temperature(T_0) and the temperature updating schedule ($T_{\mathbf{upd}}$) are the two parameters of SA algorithm and they are related with the minimization of energy, their value depends upon the magnitude of the posterior energy (Geman and Geman, 1984). The values of the SA parameters are varying from simple to complex scene and it is estimated separately for each image. At low temperature there is tight coupling between pixels of the image is observed which leads to image appearance more regular whereas at high temperature the coupling between pixels of image is loosened and resultant image appears noisy (Geman and Geman, 1984). In this research fine tuning of the SA parameters is evaluated on real dataset of ASTER image. Since, equation (4.14) is normalized in Tolpekin and Stein (2009) and applied on simulated data before therefore we can apply optimized values of SA parameter for all values of varying λ of MRF based SRM. However, in this research experimentation is conducted in the sections 4.12.1 and 4.12.2 in order to get optimal values for T_0 and T_{upd}

4.12.1. Initial temperature T_0 estimation

This experiment was performed to generate optimal T_0 for Aster Image. The experiment was conducted for $T_0 = 0, 1, 2, 3, 4$ and 5 for $\lambda = 0.5$ and $S = 3$. The mean and standard Energy value with varying SA parameter i.e., T_0 is summarized in Figures 4.11 and 4.12. The resultant values of energy mean and standard deviation is shown in Tables 4.1 and 4.2 respectively. We apply SA to minimize the energy. At low temperatures the coupling is tighter between the pixels and the images appear more regular: we get homogeneous pixels (Geman and Geman, 1984). It better explains classification. In order to produce low temperature we need low energy. Since $T_0 = 3$ consumes low energy and its standard deviation is lowest, which describes better reproducibility shown in Figures 4.11 and 4.12

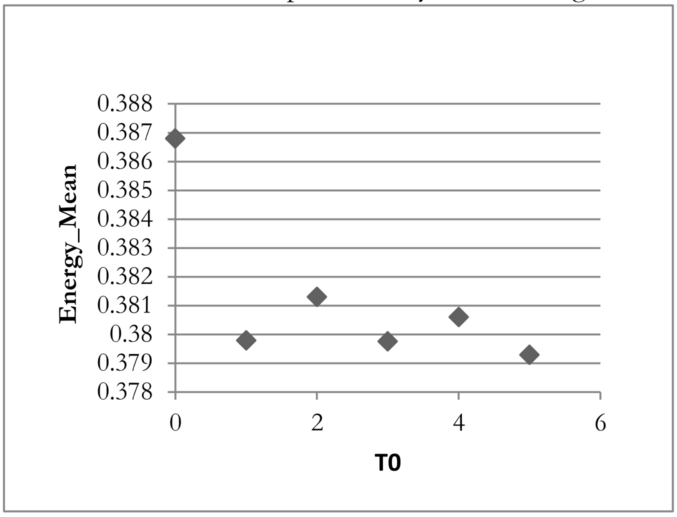

Figure 4.11 Energy mean at varying T_0

T_0	E_Mean
0	0.386793
1	0.379784
2	0.381296
3	0.379749
4	0.38059
5	0.379279

Table 4.2 Energy mean and T_0 values

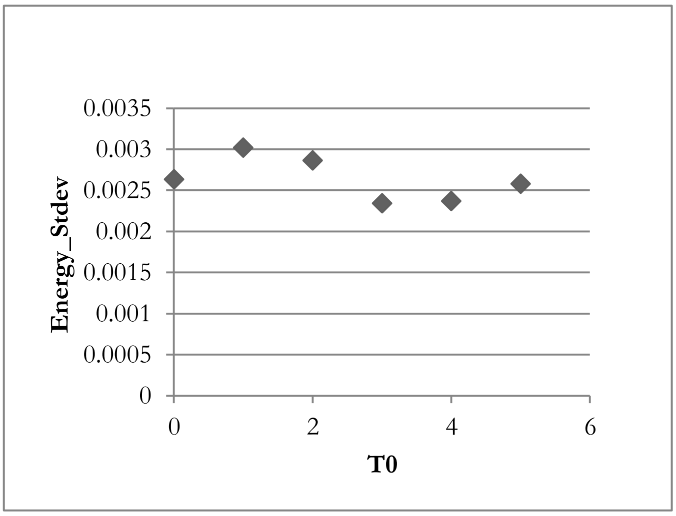

Figure 4.12 Energy standard deviation at varying values T_0

T_0	E_Stdev
0	0.002634
1	0.00302
2	0.002866
3	0.002345
4	0.00237
5	0.00258

Table 4.3 Energy std deviation and T_0 values

From the above displayed Figure 4.11 for ASTER Image, the Mean energy at the three T_0 values (1, 3 and 5) was optimal and close to each other. Similarly, from shown Figure 4.12, standard deviation is at the two T_0 values (3, 4) were optimal and close to each other. Since T_0 cosumes low energy and it shows low standard deviation. Hence, this values of SA parameter is selected as optimal value for conducting experiments. In (Geman and Geman, 1984; Hailu Kassaye, 2006; Kumar Bist, 2009; Sikazwe, 2007; Tolpekin and Stein, 2009; Tso and Mather, 2009; Welikanna, 2008), it is suggested to set in the range of either 2 or 3. Hence, it corroborates our experiment and we incorporated $T_0 = 3$ as an initial temperature parameter value in this research.

4.12.2. Optimal temperature updating schedule search

In this experiment SA parameter T_{upd} optimization was done by varying the values from 0.1 to 0.99 while other parameters were kept fixed. Demonstration is provided in Figures 4.13 and 4.14. From the Figure 4.13, it is obvious that mean κ value is optimal at $T_{\text{upd}} = 0.6$ and 0.9. In addition to that standard deviation of κ is also considered here for optimal T_{upd} search. In Figure 4.14, standard deviation of $T_{\text{upd}} = 0.9$ found to be minimum in comparison to $T_{\text{upd}} = 0.6$. A low standard deviation of κ value indicates that the results are representative for multiple values of parameter value and which is good for reproducibility as well. Hence, $T_{\text{upd}} = 0.9$ is considered as optimal temperature updating schedule in this research work. The κ and standard deviation of κ values with varying T_{upd} values are shown in the Tables 4.4 and 4.5 respectively.

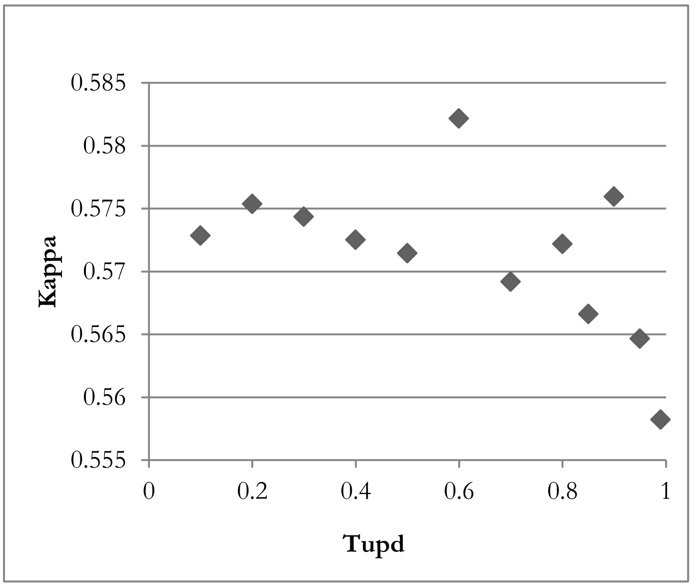

Figure 4.13 kappa $(\kappa)$with varying T_{upd} values

T_{upd}	Kappa
0.1	0.572846
0.2	0.575363
0.3	0.574349
0.4	0.572518
0.5	0.571444
0.6	0.582165
0.7	0.569177
0.8	0.572189
0.85	0.566608
0.9	0.57597
0.95	0.564665
0.99	0.558221

Table 4.4 kappa (κ) and T_{upd} values

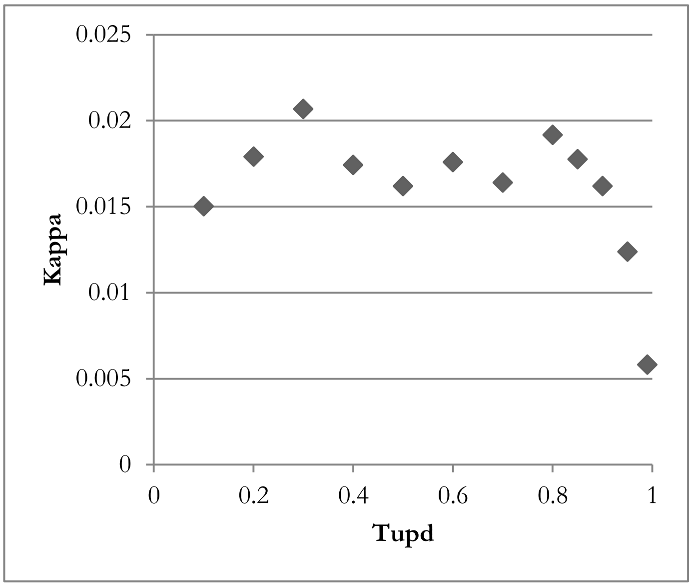

Figure 4.14 Standard deviation of Kappa (κ)

Tupd	K_Stdev
0.1	0.015015
0.2	0.017893
0.3	0.020661
0.4	0.017411
0.5	0.016182
0.6	0.017584
0.7	0.016395
0.8	0.019156
0.85	0.017755
0.9	0.016184
0.95	0.012371
0.99	0.005807

Table 4.5 Std deviation of kappa and T_{upd}

4.13. Search for optimal neighbourhood system size

After getting optimal λ values at S = 2, 3, 4, 5, 6 and 10 in the section 4.11 another experiment was conducted for the appropriate window size (W) by varying the λ values and W equal to 3, 5, 7 and 19 on the fixed S value 10. The optimal W for varying λ values at fixed S is shown in the Figures 4.15 and 4.16, in the next page. The resultant Tables for the Figures 4.15 and 4.16 are attached in the appendix (B).

In, (Tolpekin and Stein, 2009), window size 7 and 19 were founded optimal, where κ provides maximum accuracy. This experiment was performed in line with (Tolpekin and Stein, 2009). Figure 4.15 shows that $\hat{\lambda}$ is the same for all W. Since, standard deviation was small it leads to complication in the identification of $\hat{\lambda}$. Hence, κ_{max} was introduced which is equal to the largest κ mean value. For the criterion of closeness to the maximum value, we choose $\kappa \leq 0.9\kappa_{max}$. For $\lambda = 0.3, 0.4, 0.5, 0.6, 0.7$ κ_{max} value and all the combinations of W obtained. The optimal range of λ value was for between 0.1 and 0.7. Maximum value of κ was achieved at $\lambda = 0.7$ for $W = 7$ in comparison to $\lambda = 0.3$ for $W = 9$, which is shown in the Figure 4.15. Since, standard deviation of $W = 5$ is very high in comparison to the latter said two window sizes, therefore the highest accuracy in terms of κ is reached for $W = 7$ as shown in the Figure 4.16. In this research $W = 2S - 1$ is adopted for all values of $S > 1$.

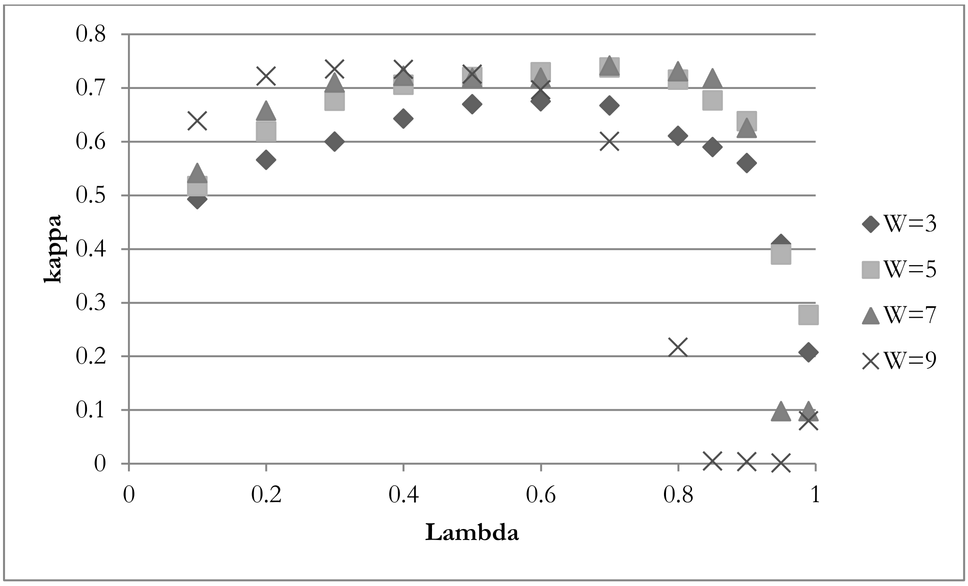

Figure 4.15 W accuracy range on varying lambda (λ)values

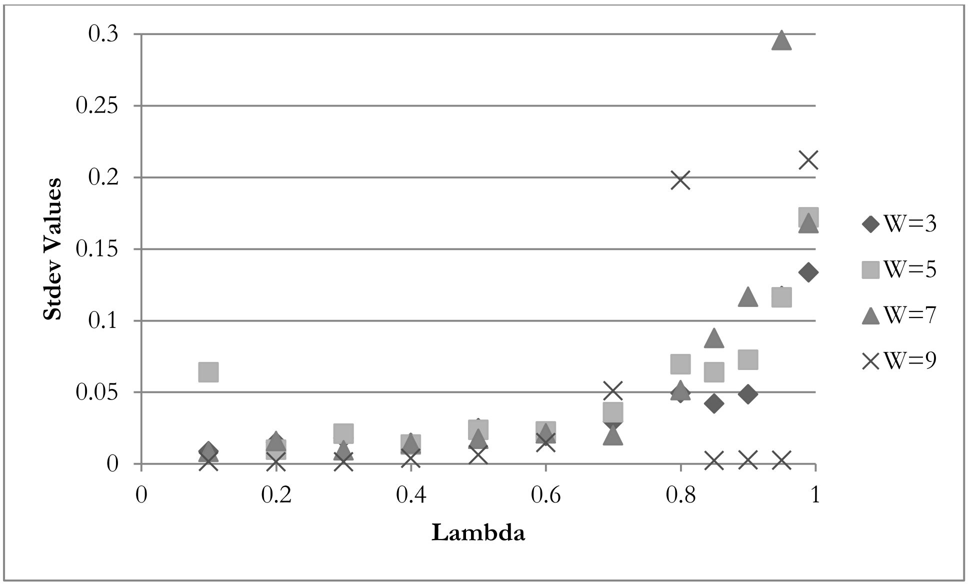

Figure 4.16 Various W sizes on varying lambda (λ) values

4.14. Accuracy Assessment

No classification is considered complete unless an assessment of accuracy has been performed (Jensen, 1986). The accuracy assessment is a critical step in any mapping process, and thus is an essential component that allows a degree of confidence to be attached to maps for their effective use. After obtaining the classified land cover map (CLCM) it is necessary to validate it. In this research validation and the accuracy assessment of the final CLCM is done against the reference data i.e., Google earth image. User's and producer's accuracies and κ values are used in accuracy in the chapter under section 5.1.3, 5.1.4, 5.2.4 and 5.2.5.

User accuracy: This is a measure of error of commission. User accuracy is computed by dividing the total number of correct pixels in a category by the total number of pixels that were classified in that category.

Producer accuracy: Probability that a reference pixel on a map is that particular class. It indicates how well the reference pixels for that class have been classified. This is a measure of error of omission.

Overall accuracy: It is computed by dividing the total number of correctly classified pixel by total number of pixel checked. It is given by:

$$\hat{P} = \frac{1}{N}\sum_{i}^{r} x_{ii} \tag{4.17}$$

Where N is the total number of classes in the image, r denotes the number of rows and columns in confusion matrix and x_{ii} is the number of correctly classified pixels.

Kappa coefficient: The kappa analysis is a discrete multivariate technique used in accuracy assessment for statistically determining if one error matrix is significantly different than other (Congalton, 1991). In this research the kappa coefficient will be used as a measure of accuracy of the super resolution mapping method. Kappa coefficient is computed by:

$$\kappa = \frac{N\sum_{i=1}^{r} x_{ii} - \sum_{i=1}^{r}(x_{i+}.x_{+i})}{N^2 - \sum_{i=1}^{r}(x_{i+}.x_{+1})} \tag{4.18}$$

Where, N is the number of observations. r is the number of rows in the matrix, x_{ii} is the number of observations in row I and column I (the I th diagonal elements). x_{i+}andx_{+1} are the marginal totals of row r and column I respectively. Kappa coefficient ranges between 0 and 1.

In addition to pixel – based validation described above, SR map is assessed by AEP, RMSE and CC as described in Tatem et al.(2002b). One of the measures of agreement between a set of known proportions y, and a set of estimated proportions a and n indicates the total number of pixels in this way the AEP and is formulated as follows:

$$AEP = \frac{\sum_{q=1}^{n}(y_q - a_q)}{\sum_{q=1}^{n} a_q} \tag{4.19}$$

Quality of class area proportion on the scale of coarse resolution image is assessed by the aforementioned RMSE and CC. The latter said techniques do not depend on the spatial distribution of the fine resolution sub – pixels. RMSE and AEP are used to evaluate the agreement between the fraction Images generated from MLC and SRM technique, with the reference fraction image.

RMSE informs about the accuracy of the prediction (bias and variance). It is represented by:

$$RMSE = \sqrt{\frac{\sum_{q=1}^{n}\left(y_q - a_q\right)^2}{n}} \tag{4.20}$$

The CC represents measure of the amount of association between a target and estimated set of proportion and can be presented by the below mentioned equation:

$$C_{y.a} = \frac{\sum_{q=1}^{n}\left(\bar{y}_q - y_q\right)\cdot\left(\hat{a}_q - a_q\right)}{n-1} \tag{4.21}$$

$$s_{Y.a} = \sqrt{\frac{1}{n-1}\sum_{i=1}^{n}(Y_a - \bar{Y})^2} \tag{4.22}$$

$$\mathrm{CC} = \frac{C_{y.a}}{S_y \cdot S_a} \tag{4.23}$$

Where $\mathrm{C_{y.a}}$ indicates covariance between y and a and S_y and S_a are standard deviation of y and a.

5. RESULTS

This chapter describes results obtained from MRF – based SRM. Section 5.1 presents results from Aster Image. Section 5.1 presents results of two subsets studied to identify SLE. The applied technique on SLE is evaluated for identification of FE on three subsets in the study area – 2 are dealt with in the section 5.2.

Experimental results from Aster Image

5.1. SRM results from ASTER data

The method described in Tolpekin and Stein (2009) was tested on ASTER image to deal with the real – world problem to identify SLE and FE. Reference data was created by using digital aerial photograph and Quickbird data obtained from Google earth image. The result obtained by using MRF based SRM is compared with MLC. However, fraction images were obtained by downscaling of MLC of multispectral image y, which leads to initial SRM generation, thereafter resultant SR map was obtained. The quality of SRM was measured with κ at fine resolution level, whereas, AEP, RMSE and CC accuracy measures were performed at coarse resolution level to assess the accuracy.

In all the experimentation in the coming sections the optimized T_0 and T_{upd} values i.e., $T_0 = 3$ and $T_{\text{upd}} = 0.9$ are used. They were optimized earlier in the section 4.12.1 and 4.12.2 respectively. The latter said two SA parameters depend on the complexity of the problem (Geman and Geman, 1984) and it varies complex to simplest case. Earlier in Tolpekin and Stein (2009) the equation (4.14) was normalized for the posterior energy. Hence, $T_0 = 3.0$ and $T_{\text{upd}} = 0.9$ is used for varying Smoothness parameter λ values in all the experiment performed in this research. Once we optimized the SA parameters than they become dependent on the λ, this is obvious from equation (4.14). λ is obtained by trial and error method for each S earlier in the section 4.11. In another experimentation which was conducted on ASTER image in the section 4.13 optimal W was determined for various S. The latter said optimized parameters are applied in all the experiments performed in the coming sections. The resultant plot for temperature, error evolution and energy minimization in provided in the appendix (B).

5.1.1. SLE with different scale factors

Subset of dimension 30×32 was selected for studying the quality of super resolution map with respect to identification of SLE shown in the Figure 5.1 (b). The resultant output from $S = 2, 3, 4, 5, 6, 10$ is demonstrated in the Figures 5.2 and 5.3. The Figure 5.2 (c), shows smooth boundary than output of MLC in Figure 5.2 (b). Earlier in the section 4.13 it was observed that larger W at larger S are computationally expensive and time consuming and it leads to over smoothening of the resultant SRM. However, it is applied on the above mentioned subset to see the result. The resultant map at $S = 2$ is acceptable whereas SRM obtained at $S = 3, 4, 5, 6, 10$ are not acceptable as it leads to confusion for the end user to read. Some scattered trees are present on the top left corner of the input image which is demonstrated in Figure 5.1 (b), which is neither accurately classified by MLC nor MRF based SRM technique shown in the Figurers 5.2 (b) and (c). Same result is obtained from middle bottom part of the input image. Due to the fact that at $S = 2$ with optimized SA parameters, W with λ obtained in this section provides good quality SR map in comparison to other higher S. Hence in the next experiment which is conducted in the section 5.1.2 for detection of SLE, SRM is obtained at $S = 2$ for further analysis. Here in this experiment three landcover classes were taken into account i.e., trees, heath and waterbody with training pixels 1020, 276 and 272 respectively.

(a) (b)

Figure 5.1 (a) digital aerial photograph with resolution 0.50 m (b) Aster image with resolution at 15 m with band combination of 3,2,1

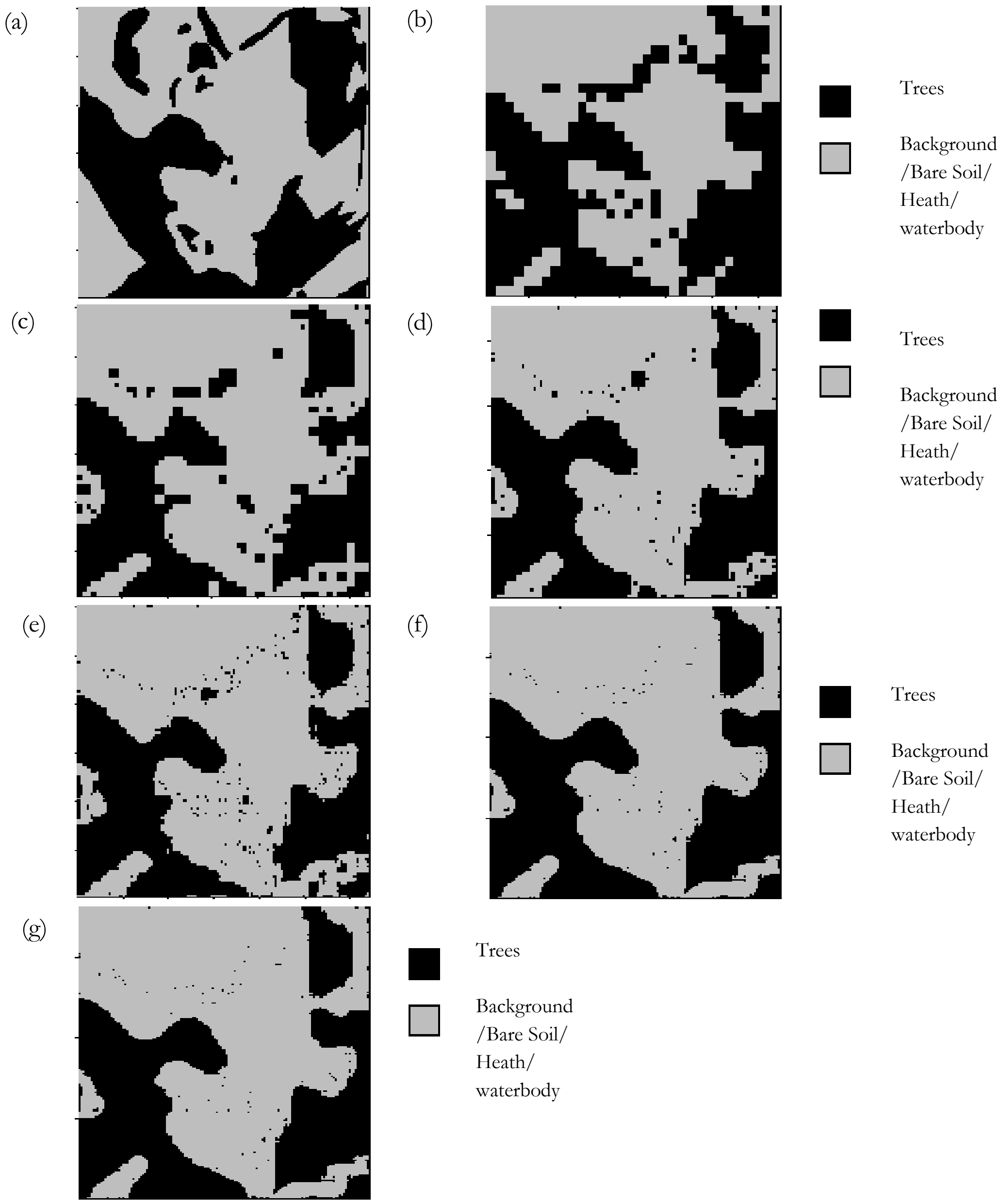

Figure 5.2 (a) Reference map prepared from digital aerial photo. (b) MLC classified map at 15 m resolution (c)-(g) SRM at S=2,3,4,5 and 6

S=10, $\lambda = 0.3$(h)

S=10, $\lambda = 0.4$(i)

S=10, $\lambda = 0.5$(j)

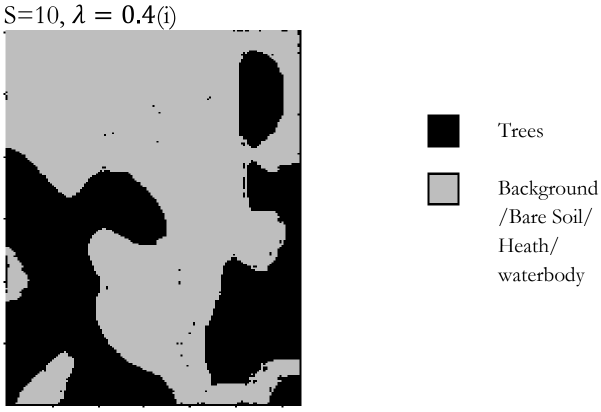

S=10, $\lambda = 0.6$(k)

S=10, $\lambda = 0.7$(l)

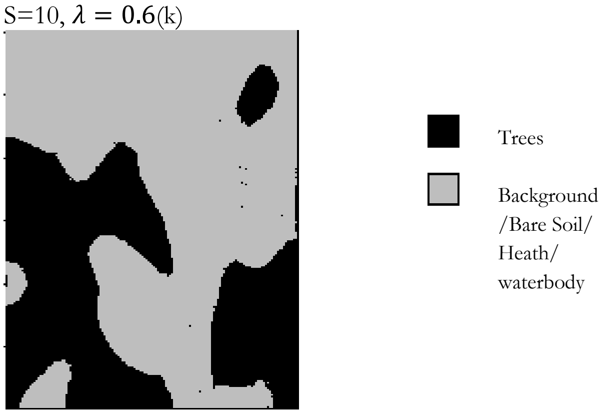

S=10, $\lambda = 0.8$ (m)

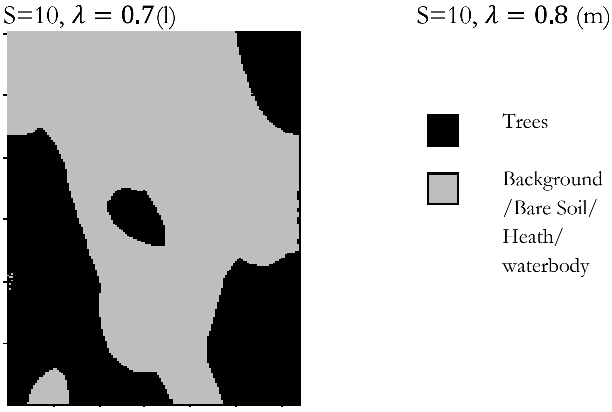

S=10, $\lambda = 0.9$(n)

Figure 5.3 (h)-(n) SRM at $S = 10$ with varying $\lambda = 0.3, 0.4, 0.5, 0.6, 0.7, 0.8, 0.9$

In Figure 5.3 (h)-(n), output SR maps are achieved at $S = 10$ with $W = 3, 5, 7, 19$ with varying λ values, it is worthy to mention here that in the section 4.13 optimal value of λ was 0.6 but in this case if we look on the SR map shown in the Figure 5.3, it is $\lambda = 0.3, 0.4$ which provides better ouput than $\lambda = 0.6$. $\lambda = 0.4$ lies in the range of lambda values whereas $\lambda = 0.3$ is out of range which is shown in the Table 4.1 under section 4.11 in the chapter 4.

5.1.2. SLE identification with Aster 15 meter resolution data

In order to identify linearly located group of trees i.e., SLE an ASTER data subset of size 16×32 was chosen and it comprised of three landcover classes: heath, baresoil and trees. The total numbers of training pixels were 276, 477 and 1020 for heath, baresoil and trees respectively. Since the main objective of this research was to identify SLE hence, purposely the place is selected where mainly three landcover classes were present. This experiment was conducted to observe how accurately lineary located group of trees are identified by MLC and SRM, which is shown in Figure 5.4 (d) and (e).

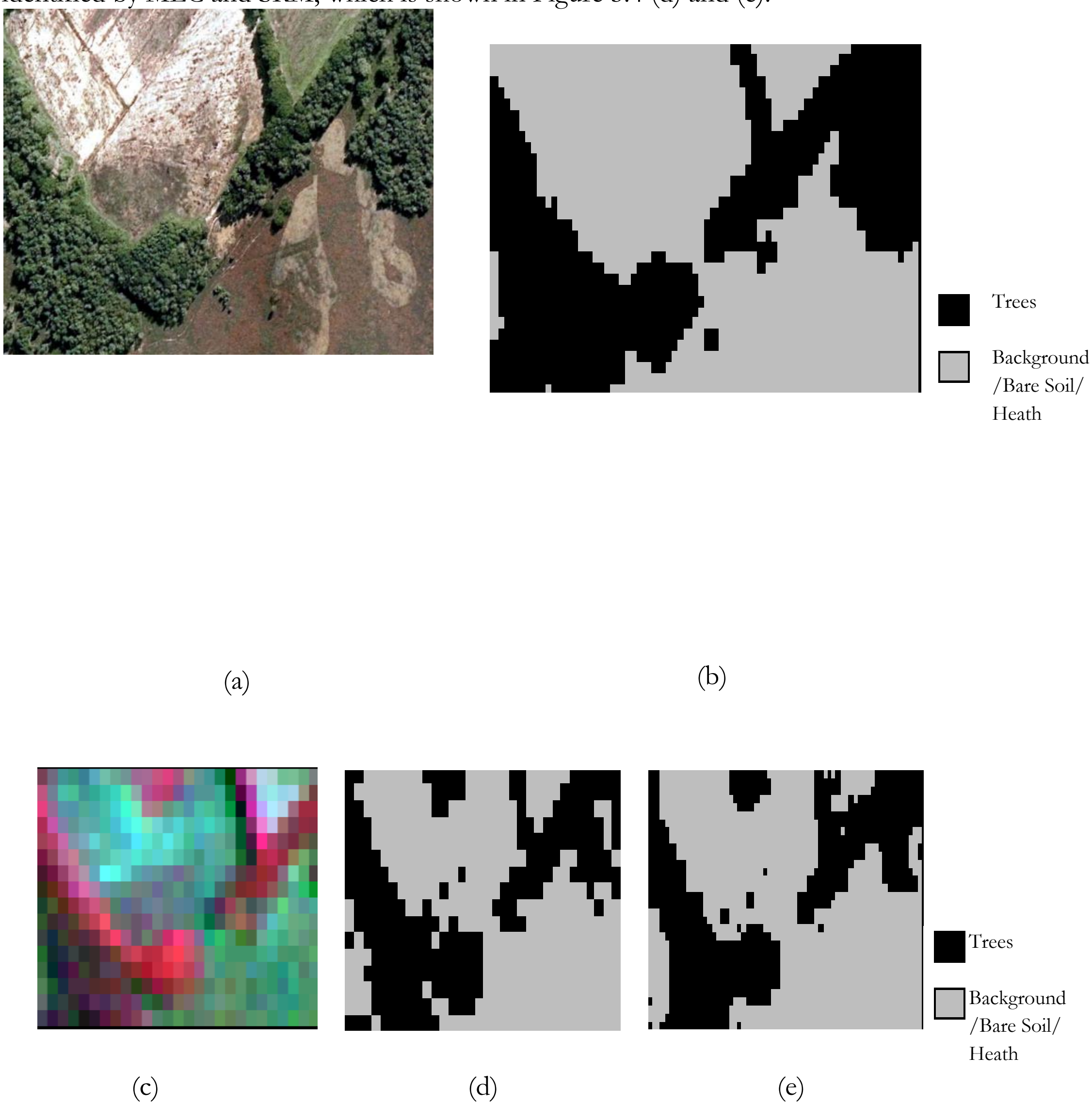

Figure 5.4 (a)Google Earth image with 0.50 m resolution (b) Manually prepared reference map (c) ASTER image at 15 meter resolution with band combination 3,2,1 (d) MLC map and (e) SR map with SLE(Group of trees) at 7.5 meter resolution at S=2.

The result obtained in the Figure 5.4 (d) doesn't have smooth boundary. The demerit which was observed in the output classification result of Figure 5.4 (d) is overcome in the SR map of SLE which is shown in

Figure 5.4 (e). In the Figure 5.4 (e) SLE has smooth boundaries in comparison to Figure 5.4 (d). Hence, here in the above fig it is observed that classified map provided by SRM is more accurate and smoother than MLC. Hence, we can say that in this experimental result smoothness of boundaries is resolution issue.

5.1.3. Classification accuracy of SLE

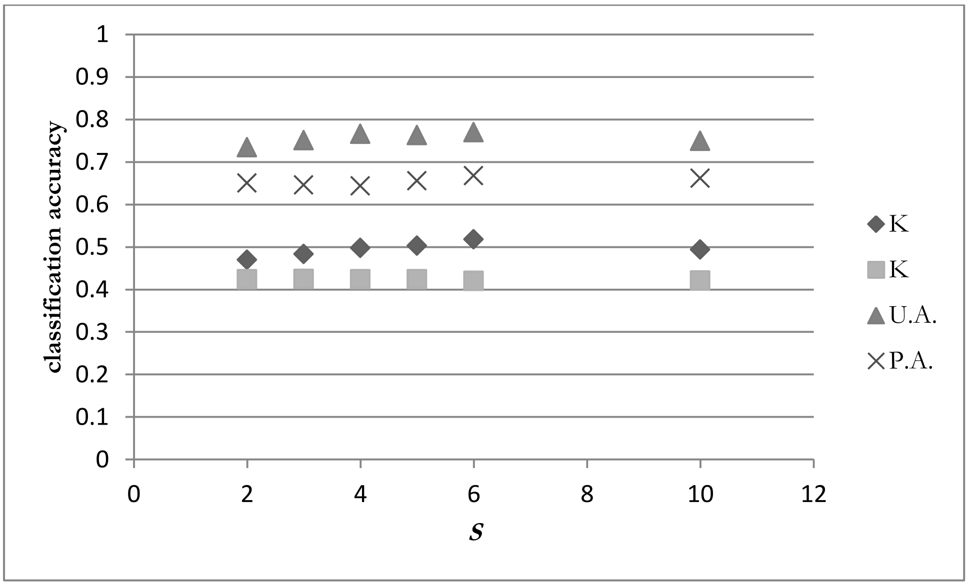

Figure 5.5 Classification accuracy SLE in terms of K , Producer and User Accuracy.

Figure 5.5, demonstrates that κ value of SRM is higher than MLC in terms of classification accuracy. It is also justified that the κ value for SRM and MLC is lying the ranges of 0.4 – 0.54 whereas P.A and U.A. Of SRM is lying in the range of 0.6 – 0.7. Classification accuracy of SLE in terms of P.A. and U.A. is more than κ value of SRM which indicates that landcover class trees (SLE) is accurately mapped by SRM.

5.1.4. Accuracy assessment

After getting result of SRM in the previous sections 5.1.2 and 5.1.3, it needs to be assessed for its accuracy. The SLE results obtained were assessed by κ at fine resolution level which is shown Tables 5.3 and 5.4. In addition to that accuracy for the SLE was assessed by fraction images produced from SRM and MLC at coarse resolution level. Accuracy statistics for the SLE by AEP, RMSE and CC accuracy measures is shown in table 5.1 and 5.2 respectively.

Result for experiment conducted on subset 16×32					
MLC			**SRM**		
RMSE	CC	AEP	RMSE	CC	AEP
0.384	0.679	0	0.325	0.745	0.020

Table 5.1 Results of CC, AEP and RMSE

SRM, CC results in the Table 5.1, shows that there is a high correlation between the predicted and the known fractions whereas in case of MLC, CC result is lower than SRM in other words correlation is lesser in between predicted and the known fractions in case of MLC. RMSE drops by a significant amount in SRM in comparison to MLC whereas value of AEP in case of MLC is 0 and for SRM the value of this error measure is more, which is obvious from the result shown in the Table 5.6. Hence, we can say that SRM outperformed MLC.

In case of SRM, CC is 0.568 whereas for MLC it is 0.461, from the resultant Table 5.2, it is found that correlation is high in SRM between predicted and known fractions. In case of AEP value of SRM value is more than MLC, which is shown in the Table 5.2. Hence, SRM found to be better than MLC in terms of RMSE and CC.

Result for experiment conducted on subset 30×32					
	MLC			**SRM**	
RMSE	CC	AEP	RMSE	CC	AEP
0.497	0.461	0.023	0.412	0.568	0.050

Table 5.2 Results of CC, AEP and RMSE

Result for experiment conducted on subset 16×32		
	SRM	**MLC**
$\boldsymbol{\kappa}$	0.660	0.645

Table 5.3 κ value for SRM and MLC

Κ result shown in the Table 5.3, indicates that SRM is giving more classification accuracy than MLC in order to identify SLE. Hence, fine resolution accuracy assessment of SRM shows improved results than MLC.

Result for experiment conducted on subset 30×32		
	SRM	**MLC**
$\boldsymbol{\kappa}$	0.469	0.424

Table 5.4 κ value for SRM and MLC

In this experiment also the κ value of SRM is observed higher than MLC. The κ value of MLC is smaller than SRM; it is justified by the visual interpretation of the resultant SR map demonstrated in the Figure 5.2 (c) and supported by the higher value of κ in the Table 5.4.

5.2. FE identification with Aster 15 meter resolution data

Further the applied technique for identification of SLE was evaluated for identification of FE in Rutland Island (Study area – 2). By expert knowledge and the visual interpretation of VNIR bands of ASTER image with 15 meter resolution combined with high resolution Quickbird data captured from Google earth image three encroachment sites were identified for study. In the subsequent sections for experimental results three landcover classes i.e., forest, waterbody and encroached_area (modelled as FE) were selected. Discussion on encroached_area is provided in the discussion chapter. The training pixels 485, 86 and 256 were collected for forest, waterbody and encroached_area respectively. It was very difficult to get pure pixel for class waterbody and encroached_area. However, pure and homogeneous pixels were taken for the latter said training sites. Besides, this T_0= 3 and T_{upd} = 0.9 values were taken for experimentation in the later sections. In addition to that optimized parameter values of λ and optimal W were applied for the subsequent experimental results, earlier the said parameters were optimized in the sections namely 4.11 and 4.13 respectively. The resultant plots for temperature, error evolution and energy minimization in provided in the appendix (B).

5.2.1. FE with different scale factors

Subset with dimension 58×60 was chosen for study at different S, which is shown in the Figure 5.6 (b), this FE site was evaluated for its suitability at various S. It is observed that quality of SRM is decreased by increasing S. However, at $S = 2$ best optimal SR map in achieved which is shown in Figure 5.7 (c) . In the case of $S = 3,4,5,6,10$ it leads to over smoothening. Hence in the coming sections SRM at $S = 2$ is generated for evaluating FE.

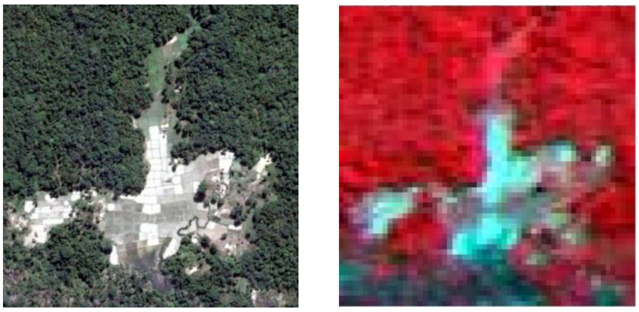

(a) (b)

Figure 5.6 (a) Quick bird image obtained from Google Earth, (b) Subset from Aster image at 15 meter resolution with band combination 3,2,1

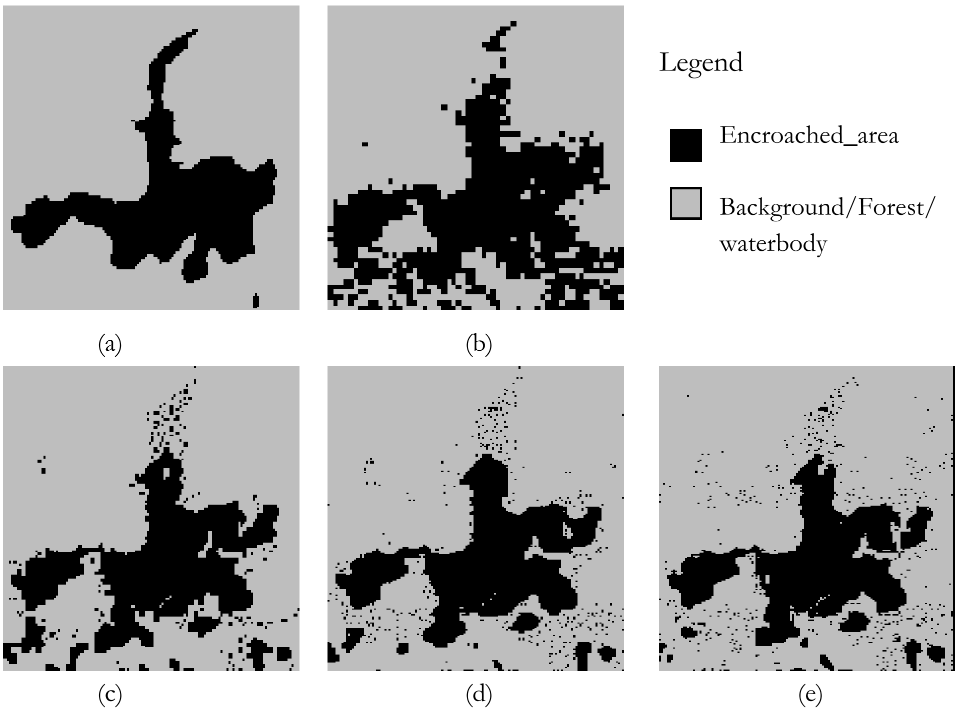

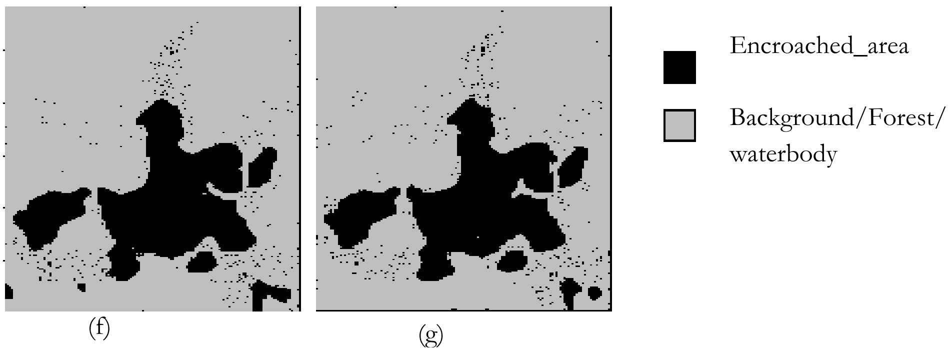

Figure 5.7 (a) reference map generated from Quickbird data (b) MLC (c)-(g) SRM at S=2,3,4,5 and 6

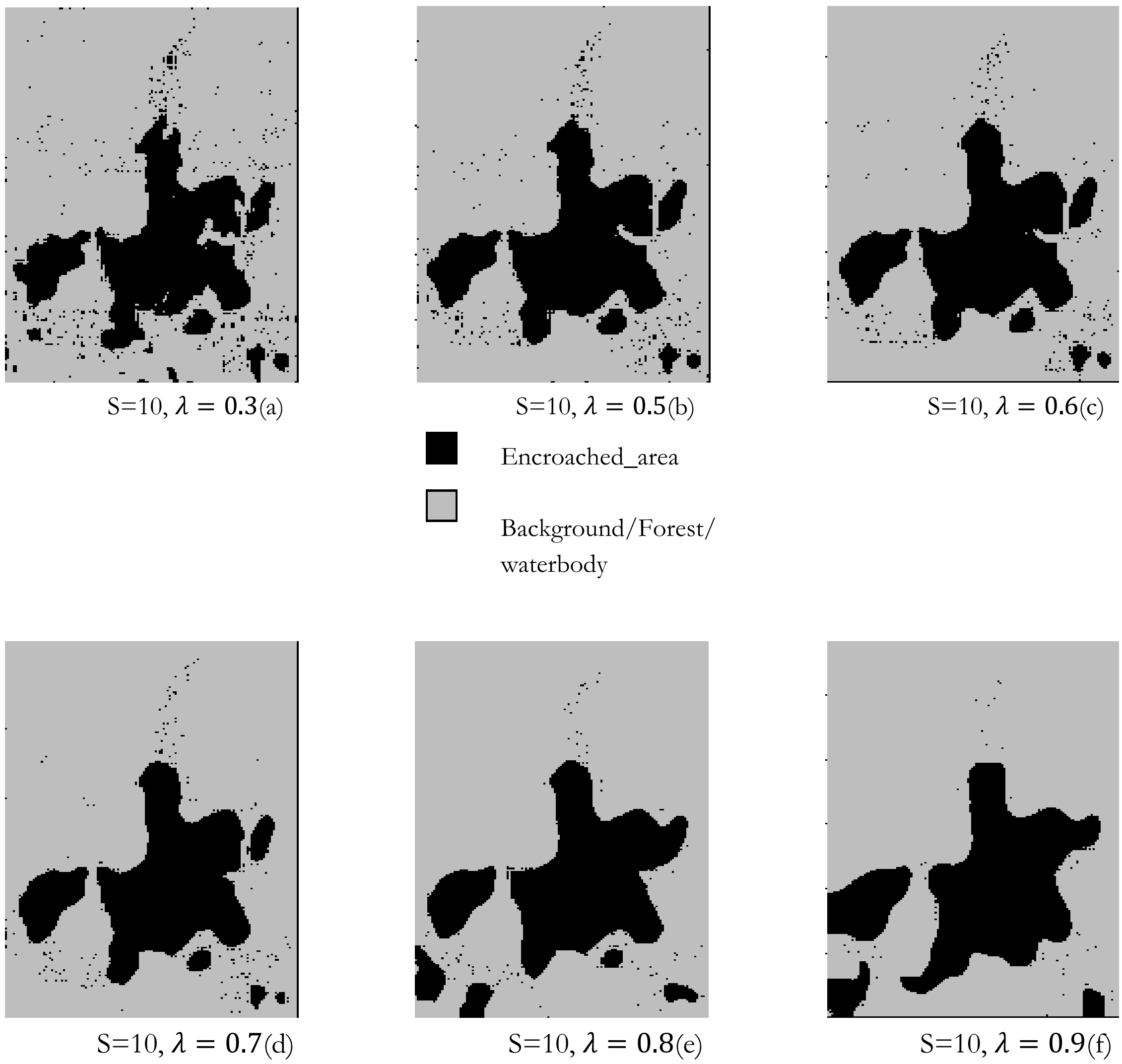

Figure 5.8 (a)-(f) SRM at S=10 with varying $\lambda = 0.3, 0.5, 0.6, 0.7, 0.8, 0.9$

In Figure 5.8 (a)-(f), output SR maps are achieved at $S = 10$ with $W = 3, 5, 7, 19$ with varying λ values, it is worthy to mention here that in the section 4.13 optimal value of λ was 0.6 but in this case if we look on the SR map shown in the Figure 5.8, it is $\lambda = 0.3, 0.5$ which provides better ouput than $\lambda = 0.6$. $\lambda = 0.5$ lies in the range of lambda values whereas $\lambda = 0.3$ is out of range which is shown in the Table 4.1 under section 4.11 in the chapter 4.

5.2.2. Smallest FE with dimension 16×14

Smallest FE site: This place is known by the name RM point where FE was identified and it is one of the smallest FE site present in the Rutland Island (study area – 2). From the reference map it is clear that it is case of linear sub pixel. On the uppers side of the FE site which is shown in Figure 5.9 (a) the shape of FE looks like linear which is fallow land with some grass. However, the resultant map of MLC and optimized SRM shows that linear sub pixel case is difficult to detect. Moreover, this FE site seems like linear at the top but it has main encroachment at the bottom part and which is successfully identified by the MRF based SRM technique. Some objects were smaller and their radius was less than resolution of the ASTER data. Hence, they were missed, which is shown in Figure 5.9 (e).

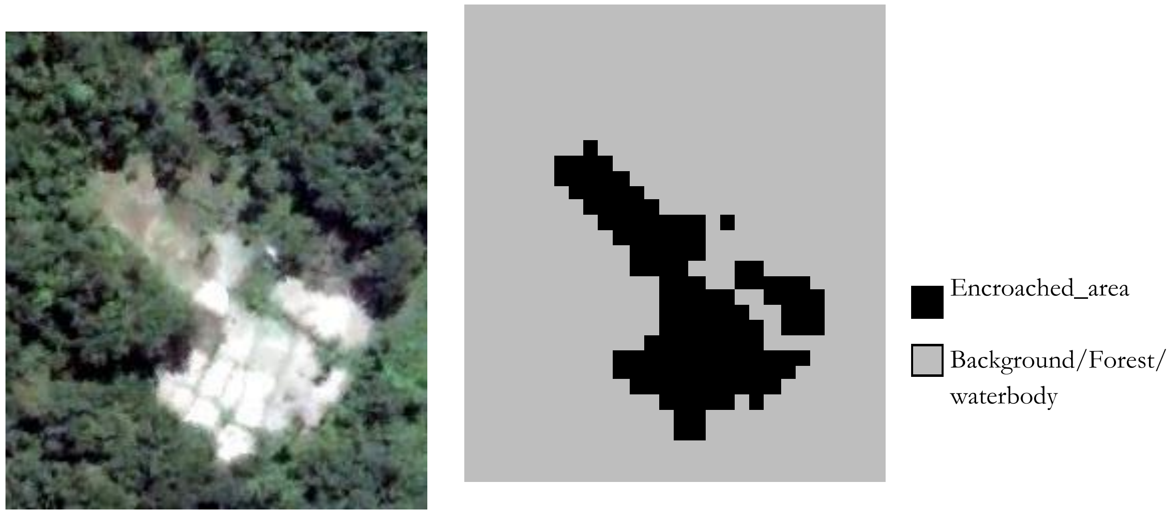

(a) (b)

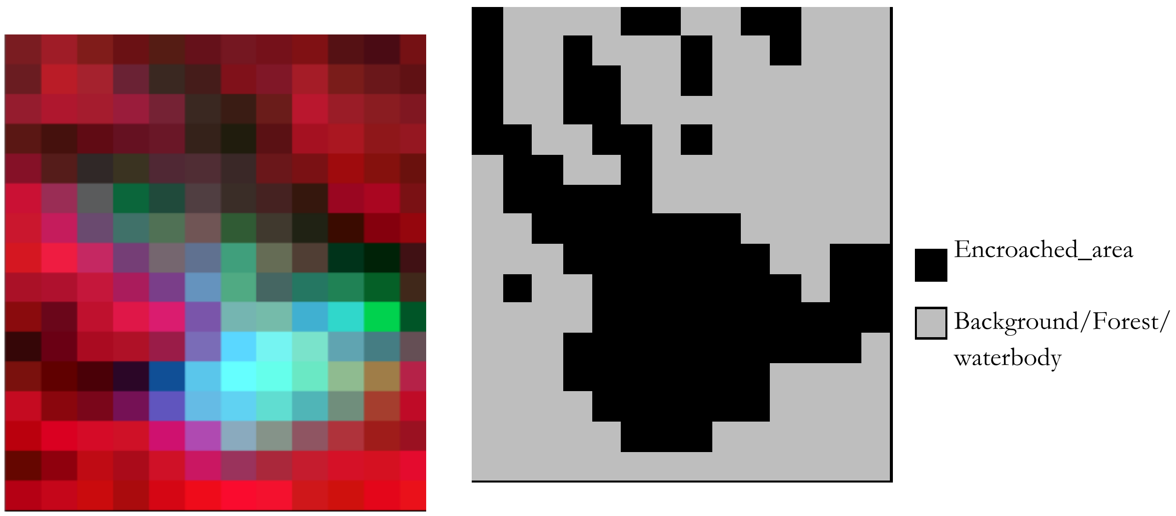

(c) (d)

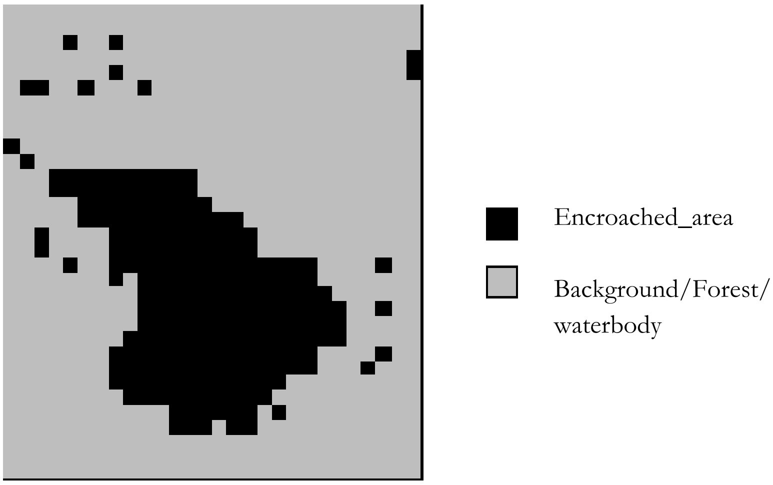

(e)

Figure 5.9 (a)Google Earth image (Quickbird data)(b) Manually prepared reference map (c) ASTER image at 15 meter resolution with band combination 3,2,1 (d) MLC map and (e) Optimized SR map with FE (mixed landcover) at 7.5 meter resolution at S=2.

5.2.3. Third FE site

The third, FE site with dimension $\mathbf{44 \times 32}$ is like curvature in nature and it is very well identified by the MRF based SRM technique. With few isolated objects but it outperformed MLC in terms of classification accuracy and quality aspects, which is shown in Figure 5.10 (e).

(a) (b)

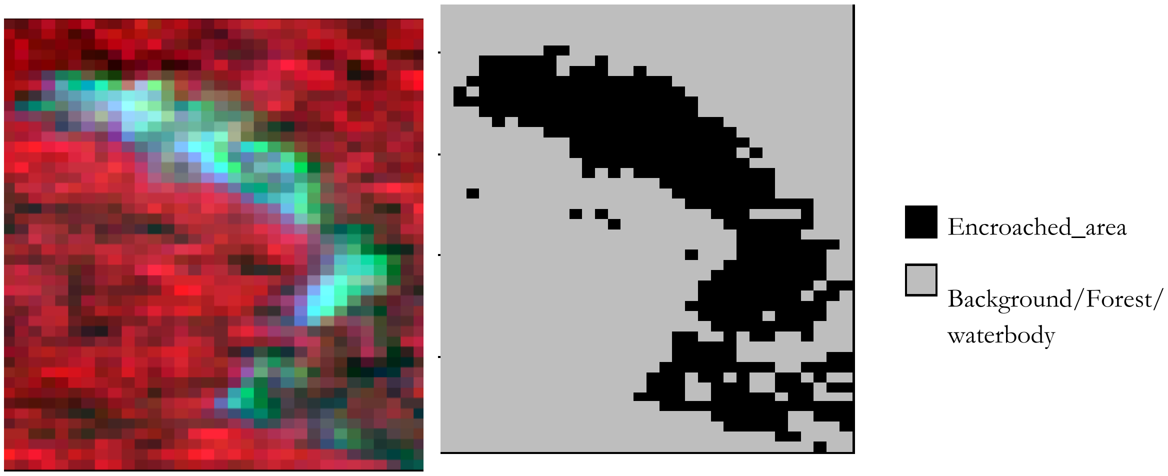

(c) (d) (e)

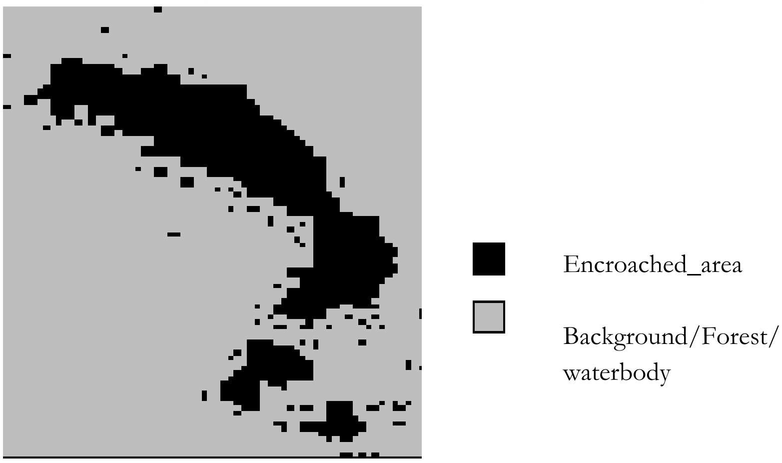

(e)

Figure 5.10 (a)Google Earth image (Quickbird data) (b) Manually prepared reference map (c) ASTER image at 15 meter resolution with band combination 3,2,1 (d) MLC map and (e)SR map with FE (mixed landcover) at 7.5 meter resolution at S=2.

5.2.4. Classification accuracy of Encroached_area

The subset in the section 5.2.1 was selected for experimentation to study the effect of classification accuracy at different scale factors with varying W optimized in the Section 4.13.The Figure 5.11, shows that User's and Producer's accuracy are more than κ value of SRM. This trend indicates low agreement between reference and classified map. In this experiment κ values of SRM and MLC varies in the range of 0.5 – 0.7 and on the other hand user and producer accuracy of SRM is varying in the range of 0.65 – 0.8 which is shown in the Figure 5.11. Classification accuracy of Encroached_area is high in terms of Producers's and User's accuracy, which indicates that it is better classified by SRM

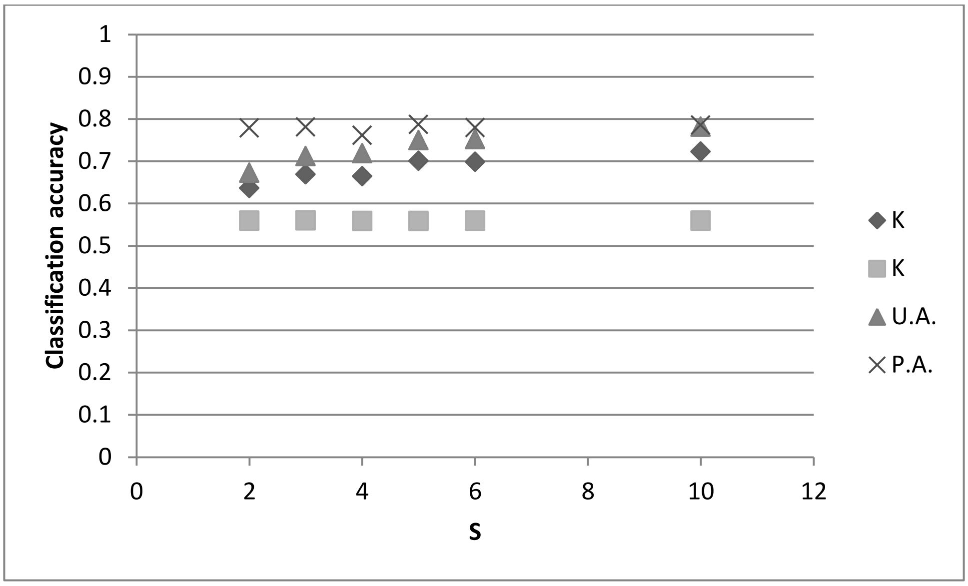

Figure 5.11 Classification accuracy range in terms of SRM, MLC, U.A (User's accuracy) and P.A.(Producer's accuracy.

5.2.5. Accuracy assessment

Subset with dimension 16×14					
	MLC			SRM	
RMSE	CC	AEP	RMSE	CC	AEP
0.515	0.456	0.256	0.289	0.739	0.118

Table 5.5 values of CC, AEP and RMSE

CC values shows association between target and estimated fractions. In case of SRM, fractions are highly correlated whereas in MLC, the correlation between the fractions is low which is revealed from the Table 5.5. Same trend is followed for RMSE also where SRM outperformed MLC. However, in case of AEP MLC result is higher than SRM and in this accuracy assessment measure.

Subset with dimension 44×32					
	MLC			SRM	
RMSE	CC	AEP	RMSE	CC	AEP
0.363	0.665	0.131	0.217	0.814	0.046

Table 5.6 values of CC, AEP and RMSE

Here the CC value of MLC is observed to be lower than SRM which further resulted into low correlation between target and estimated fractions of MLC. RMSE is dropped in SRM whereas it is has high value in comparison to MLC. AEP is found to be more in MLC than SRM, which is demonstrated in the Table 5.6.

In this experiment CC value for SRM is 0.721 which is higher than MLC, CC value. In other words the correlation between predicted and target proportion in SRM is higher than MLC. Same trend is followed for RMSE also where SRM outperformed MLC. However, in case of AEP MLC result is higher than SRM and in this accuracy assessment measure, MLC is outperformed SRM.

Subset with dimension 58×60					
MLC			**SRM**		
RMSE	CC	AEP	RMSE	CC	AEP
0.414	0.604	0.124	0.298	0.721	0.034

Table 5.7 values of CC, AEP and RMSE

Kappa is used to compare how one confusion matrix differs from other. In this case accuracy assessment was done by comparing kappa value obtained from MLC and SRM. Table 5.8, shows kappa value obtained from Subset 16 × 14 where MLC has 0.33 but for SRM is reported higher i.e., 0.55. In the second subset with dimension 44 × 32 kappa value of SRM is higher than MLC kappa value demonstrated in the Table 5.9. In the last subset for FE the kappa value of MLC is reported to be 0.55 whereas, for SRM the kappa value is 0.63 which is far better than MLC kappa results. It is obvious from the results demonstrated in Tables 5.8, 5.9 and 5.10 that SRM outperformed MLC at fine resolution level in terms of kappa accuracy assessment.

Kappa

Subset with dimension 16×14		
	SRM	MLC
Kappa	0.55	0.33

Table 5.8 value of Kappa

Subset with dimension 44×32		
	SRM	MLC
Kappa	0.69	0.58

Table 5.9 value of Kappa

Subset with dimension 58×60		
	SRM	MLC
Kappa	0.63	0.55

Table 5.10 value of Kappa

6. DISCUSSION

This chapter is dealt with discussion on the achieved results obtained in the previous chapter. Parameter optimization of SA is done with respect to T_0 andT_{upd} . Experiment was conducted to achieve range and optimal value for the internal method parameter of MRF based SRM i.e .,λ. Search for optimal Wat S=10 was conducted. The resultant output of SRM was compared with output of MLC. Accuracy assessment was done at fine and coarse resolution image. It is noted that all experiment in this research work were conducted on real ASTER image with spatial resolution of 15 m to obtain optimal values of parameters. Firstly, obtained optimal parameters is discussed followed by output achieved for the two study areas mentioned in the chapter 3 to deal with real world problem to identify SLE and FE using MRF based SRM.

The two SA parameters i.e., T_0 and T_{upd} are used to minimize the posterior energy and cooling schedule of the said algorithm. In this research experiment was conducted in the section 4.12.1 and 4.12.2 for fine tuning of SA parameters. Firstly, T_0 was fine tuned by varying its value at fixed scale factor and other fixed parameter for ASTER image. After obtained $T_0 = 3$ as an optimal value for the T_0 parameter another experiment was conducted in order to obtain the optimal value for T_{upd} and in this case the parameter value T_0 was kept fixed at 3 tuning of T_{upd} was done by varying T_{upd} values and it was found that $T_{\mathrm{upd}=0.9}$ was the optimal value for ASTER image used in this research work. The latter said two SA parameters depend on the complexity of the problem and it varies from complex to simplest case. However, the equation (4.14) was normalized for the posterior energy. Hence, $\mathrm{T}_0 = 3.0$ and $\mathrm{T}_{\mathrm{upd}} = 0.9$ was used for in all the experiments performed in this research which in turn provided better results. The results obtained for T_0 and T_{upd} were agreed with the findings of (Tolpekin and Stein, 2009)

The internal method parameter λ needs to be estimated before applying on the MRF based SRM. The latter said parameter can be estimated in dual way i.e., it might be estimated via training site or by performing trial and error method, the first procedure is time consuming whereas second one is computationally expensive. In this research work trial and error method is adopted to get range of and optimal value of internal method parameter which is demonstrated in Figure 4.9, Figure 4.10 and Table 4.1 respectively. Figure 4.9, demonstrates mean κ values at varying S. Whereas in Figure 4.10 standard deviation of κ is shown at varying . The resultant range of method parameter is obtained by selecting optimal range and in terms of classification accuracy obtained from kappa statistics. κ_{max} is obtained by taking into account the largest meant kappa value which is shown in the Table attached in Appendix B. Furthermore, again it is found that range and optimal value of internal method parameter which was obtained by doing experiment on the real data i.e. Aster image were agreed with the finding of (Tolpekin and Stein, 2009). Here it is worthy to mention that all experiments in (Tolpekin and Stein, 2009) were conducted on normally distributed synthetic data i.e., simulated data.

In another experiment which is performed in section 4.13 under chapter 4 at $S = 10$, by taking W equal to 3, 5, 7 and 19. Here, it is observed that with increase in W there is increase in the neighborhood system size and clique size which leads to computational complexity. In Figures 4.15 and 4.16 the result of mean and standard kappa is shown where it is obtained by varying Window sizes and λ by adopting the optimized SA parameters demonstrated in the section 4.12.1 and 4.12.2 respectively under chapter 4. The resultant Tables for the Figures 4.15 and 4.16 are appended in the appendix (A). In this case also, it is observed that the result achieved were agreed with the finding of (Tolpekin and Stein, 2009).

Before starting experiments on real ASTER data comparison between the objet for identification and ASTER Image reveals that we are dealing with L-resolution scene models. In L-resolution scene model objects are smaller than resolution cells, so it is assumed that one pixel will resemble its neighbour (Strahler et al., 1986; Woodcock and Strahler, 1987). In (Fisher, 1997) four types of mixed pixels are defined i.e., boundary, intergrade, sub pixel and linear sub pixel wherein, boundary sub pixels describe the easier case for SRM. In this research work boundary mixed pixel for SLE was observed whereas combination of boundary and linear sub pixel case for FE is dealt with. As suggested in (Jupp et al., 1988) we are dealing with L-resolution case where each digital value represents a brightness for a combination of objects and background. Since in both study areas we are dealt with L-resolution case hence low classification is achieved. Earlier in (Tolpekin and Stein, 2009) high classification was reported in their study on synthetic images wherein they studied on H-resolution case. In this research work, MRF based SRM is checked for its effectiveness in identifying SLE and FE at two study sites. Hence, in the coming paragraphs outcome of every experiment is discussed. First the MRF based SRM technique described in (Tolpekin and Stein, 2009) is discussed for SLE identification later on results of the latter technique is discussed in identification of FE.

Subset of dimension 30×32 was selected for studying SLE in study area – 1 the quality of SR map generated for SLE, which is shown in Figures 5.2 and 5.3. The resultant output from SR map at $S = 2, 3, 4, 5, 6, 10$ is demonstrated in Fig 5.3. As earlier noted in (Hailu Kassaye, 2006; Welikanna, 2008) even with the optimized parameters the quality of SRM is decreases with increasing S and same is demonstrated by results obtained in the section 5.1. In Figures 5.2 (b) and (c), it is evident that some objects are missing. It is observed from the MLC and SRM map shown in the Figures 5.2 and 5.3 that both are unable to capture scattered young trees present in the experimental subset of ASTER image. This is due to the fact that the MRF model favours a more homogenous SRM than the isolated pixels, it result in the loss of some small objects i.e., trees. Moreover, it is obvious from the Figure 5.2 (d) onwards that increase in scale factor leads to loss of quality in final SRM. In addition to that over smoothening is observed after S=2. Since, S=2 with neighbourhood window size with smoothness parameter obtained in this section gives good quality in comparison to other higher S. The resultant map at $S = 2$ is acceptable whereas the SRM obtained at $S = 3, 4, 5, 6, 10$ are not acceptable as it leads to confusion for the end user to read due to over smoothening and loss of some objects of interest.

In next experiment where subset of dimension 16×32 was selected to study SLE, one peculiarity is observed that some landcover which is not present in the reference map was found in the post classification of SRM. On verification with the reference data and the input source data it was concluded that the it might be happened due to difference of 9 days between input and reference data acquisition date or wrong date of data captured from Google earth image. In addition to that Google earth image provides imagery updation date not the acquition date for imagery captured by the sensor. Through this experiment it is also found that MRF based SRM is accurately identified linearly located group of trees in comparison to MLC, which is demonstrated in the Figures 5.4 (d) and (e).

In FE identification Encroached_area is modelled as mixed land cover class it contains mainly agricultural land, built-up, grass, baresoil. In majority of the encroached area inside the forest in the Rutland Island (study area – 2) cultivation is done by the encroachers and it is supported by visual interpretation of the Figures 5.6 (a) and (b)

Subset with dimension 58×60 was chosen for study FE at different S, which is shown in the Figures 5.7 and 5.8, but found best result at $S = 2$. It shape is very zigzag is like octopus. In addition to that one more point is observed here, when we achieved SRM at $S = 10$ by varying the λ values from 0.3,....0.9 it is found that best optimal SRM map is obtained at $S = 10$ and $\lambda = 0.3$ not $\lambda = 0.6$ found earlier in the section 4.11. One smallest FE site with dimension 16*14 was selected for studying linear sub pixel case as defined in (Fisher, 1997). On the top the shape of FE looks like linear which is fallow land with some grass. The resultant SR map shows that linear sub pixel case is difficult to detect as described in (Tolpekin and Stein, 2009). Moreover, in this case MRF based SRM identified main encroachment at the bottom part of the subset but unable to identify encroachment at the topmost part due to linear sub pixel problem, which is shown in the Figure 5.9. The third, FE site is like curvature in nature and it is very well identified by the MRF based technique. With few isolated objects but it outperformed MLC in terms of classification accuracy and quality aspects, which is shown in Figure, 5.10.

The qualities of the resultant SR map was tested for its accuracy at fine resolution level by using κ whereas; the three measures of accuracy i.e., AEP, RMSE and CC were used to assess the accuracy of SRM and MLC at coarse resolution level.

Figure 5.5 in the section 5.1.3, demonstrates that κ of SRM is higher than MLC at every S, if we observe Figure 5.5, it is found that the User Accuracy is higher than Producer Accuracy. Figure 5.11, in the section 5.2.4 it is justified that κ value of SRM is higher than MLC. In Figure 5.17, it is revealed that Producer accuracy is higher than user accuracy. Similarly, other subsets which were selected to study SLE and FE shows that κ value of SRM is higher than MLC. Furthermore results shown in Tables 5.3 and 5.4 under section 5.1.4, shows that κ value of SRM is higher than MLC, in the case of SLE. On the other hand if we look into Tables 5.8, 5.9 and 5.10 in the section 5.2.5, it is concluded that κ value of SRM is again outperformed MLC in terms of classification accuracy. In all cases discussed above κ of SRM is found to be more accurate and higher than MLC at fine resolution level.

The higher accuracies obtained for the results in Figure 5.2 (c) indicates that the MRF based SRM is suitable to detect SLE from ASTER image. Visual interpretation of Figures 5.2 (a), (b) and (c) provides information that MRF based SRM has mapped the SLE more accurately than traditional MLC. After visual interpretation of result obtained from MLC it is observed that it leads to classification in many areas, the statistics shown in Table 5.2, supports our visual interpretation. SRM results shows CC=0.5689 value in comparison to MLC where CC=0.4619 obtained with high correlation between the target and estimated fractions. Whereas RMSE value of SRM is lesser than that of MLC indicates that SRM is more accurate than MLC. Same trend is observed for AEP. Furthermore, the values presented in the Table 5.1, tells that SRM is more accurate than MLC. RMSE of SRM is reported as 0.3253 whereas in case of MLC it is 0.3843. SRM shows good correlation between target and estimated fractions whereas CC value shown in Table 5.1, for MLC is lower than SRM, same trend is observed for AEP. Here in this case also, SRM outperformed MLC.

Moreover, visual inspection of the Figures 5.7, 5.8,5.9 and 5.10 indicates that SRM is detected FE more accurately than MLC and it is supported by the values of RMSE, CC and AEP provided in the Tables 5.8, 5.9 and 5.10 respectively. In all three sites AEP value is reported smaller in case of SRM whereas it is high in MLC. CC value is higher in SRM which shows that target and estimated fractions are strongly correlated whereas correlation is low between the latter said two fractions in MLC. At one hand RMSE is higher in MLC on the other hand RMS is lower in SRM which shows that SRM has less variance and biasness. After considering all these statistics it is revealed that SRM is better than MLC in detecting FE.

The shape and size of the object are the two aspects which were considered in this research for quality of final SRM. Bigger object were identified more accurately than smaller ones. This is due to the fact that the

MRF model favours a more homogenous SRM than the isolated pixels, it result in the loss of some small objects i.e., trees.

7. CONCLUSION AND RECOMMENDATION

The main objective of this research is to apply technique for identification of SLE and FE using MRF based SRM described in (Tolpekin and Stein, 2009) and to validate the result. It contains the following research questions

- How can fine tuning of Simulated Annealing parameters be achieved?
- What is the difference in the method for parameter setting for a case with real data compared to the use of simulated data?
- What are the major improvements in the optimal neighbourhood system in comparison to earlier simulations?
- What is the framework for quality assessment at multiple spatial resolutions?
- Does the object shape and size affect the quality of final SRM?

The said study result is discussed in chapter 6. However, based on the results and discussion, the following conclusions are drawn with respect to the above mentioned research questions. The recommendation for the improvement of the result and further research are provided in section 7.2

7.1. Conclusion

Several experimental tests were conducted under chapter Results to achieve the answer for the following research questions.

7.1.1. How fine tuning of Simulated Annealing parameters can be done in this research?

This research question is related with fine tuning of SA parameters. T_0 and T_{upd} are the two SA parameters which are used to minimize the posterior energy and area associated with cooling schedule of SA algorithm. In this research experiment was conducted in the section 5.1.1 and 5.1.2 for fine tuning of SA parameters and they were found to be optimal. Hence, $\mathrm{T_0} = 3.0$ and $\mathrm{T_{upd}} = 0.9$ was used for in all the experiments performed in this research which in turn provided better results.

7.1.2. How method parameter setting differs in case of real data compared to simulated data studied before?

Another experiment was conducted in the section 4.11 for smoothness parameter which addresses the answer for the second research question. In this research didn't consider estimation of smoothness parameter from training site. We did trial and error method for estimating smoothness parameter and findings of this experiment exhibited that the method parameter estimation were agreed with the method developed in earliear for normally distributed synthetic data.

7.1.3. How optimal neighbourhood system differs in this research compared to simulated data studied earlier?

This research question was dealt in the section 4.13. Optimal neighbourhood system size varies differs from one scale factor to another. However it is observed that larger values of neighbourhood system size leads to increased computational time, they are computationally expensive.

7.1.4. How to best assess the quality at fine and coarse resolution?

The qualities of the resultant maps were tested for their quality at fine and coarse resolution respectively. Kappa statistic was used to assess the quality at fine resolution i.e. for SRM in the sections 5.1.3 and 5.2.4 respectively. Validation in terms of AEP, RMSE and CC was done at coarse resolution level to determine the quality at coarse level in the sections 5.1.4 and 5.2.5 respectively. Both accuracy assessment measures indicates that SRM is more accurate than MLC in detecting SLE and FE.

7.1.5. Does the object shape and size affect the quality of final SRM?

The shape and size of the object are the two aspects which were considered in this research for quality of final SRM. Bigger object were identified more accurately than smaller ones. This is due to the fact that the MRF model favours a more homogenous SRM than the isolated pixels, it result in the loss of some small objects i.e., trees. One more point may be concluded here after scale factor of 2 i.e., S=2 quality of final SRM map is decreasing described in sections 5.2.1 and 5.3.1 respectively.

7.2. Recommendations

- Identification of SLE and FE may be tried with VHSR which may lead to object identification at higher scale factors
- Simulated annealing parameter is computationally very expensive. Hence alternative energy minimization method may be searched for.
- This study paves a path for further research on identification of FE and SLE in different scenarios
- The applied technique in this research can be useful in identification of deemed forest (forest with in revenue villages)
- The applied technique could be used for classification of poorly separable classes for instance forest cover classification

BIBLIOGRAPHY

Abdulkadir-Sunito, M., and Sitorus, M. (2007). From ecological to political buffer zone: ethnic politics and forest encroachment in Upland Central Sulawesi. In T. Tscharntke, C. Leuschner, M. Zeller, E. Guhardja & A. Bidin (Eds.), *Stability of Tropical Rainforest Margins* (pp. 165-178): Springer Berlin Heidelberg.

Ardila Lopez, J. P., Tolpekin, V. A., and Bijker, W. (2010). Markov random field based super - resolution mapping for identification of urban trees in VHR images. *IGARSS 2010 : Proceedings of IEEE international Geoscience and Remote Sensing Symposium, 25-30 July 2010, Honolulu, USA. ISBN 978-1-4244-9564-1. pp. 1402-1405.*

Atkinson, P. M. (2004a). Resolution manipulation and sub-pixel mapping. *Remote Sensing Image Analysis: Including the Spatial Domain*, 51-70.

Atkinson, P. M. (2004b). Super-Resolution Land Cover Classification Using the Two-Point Histogram (pp. 15-28).

Atkinson, P. M. (2005). Super-resolution target mapping from soft classified remotely sensed imagery. *Photogrammetric Engineering and Remote Sensing, 71*(7), 839-846.

Atkinson, P. M. (2008). *Issues of uncertainty in super-resolution mapping and the design of an inter-comparison study.*

Atkinson, P. M. (2009). Issues of uncertainty in super-resolution mapping and their implications for the design of an inter-comparison study. *International Journal of Remote Sensing, 30*(20), 5293 - 5308.

Atkinson, P. M., Cutler, M. E. J., and Lewis, H. (1997). Mapping sub-pixel proportional land cover with AVHRR imagery. *International Journal of Remote Sensing, 18*(4), 917-935.

Baranga, D. (2007). Observations on resource use in Mabira Forest Reserve, Uganda. *African Journal of Ecology, 45*, 2-6.

Bender, O., Boehmer, H. J., Jens, D., and Schumacher, K. P. (2005). Using GIS to analyse long-term cultural landscape change in Southern Germany. *Landscape and Urban Planning, 70*(1-2), 111-125.

Besag, J. (1974). Spatial interaction and the statistical analysis of lattice systems. *Journal of the Royal Statistical Society. Series B (Methodological)*, 192-236.

Bijker, W., Ardila Lopez, J. P., and Tolpekin, V. A. (2010). Change detection and uncertainty in fuzzy tree crown objects in an urban environment. *In: GEOBIA 2010 : geographic object - based image analysis, 29 June-2 July 2010, Ghent, Belgium : proceedings / editor E.A. Addink, F.M.B. Van Coillie. - [s.l.] : International Society for Photogrammetry and Remote Sensing (ISPRS), 2010. - (International Archives of Photogrammetry and Remote Sensing : IAPRS : ISPRS ; XXXVIII-4/C7), 6 p.*

Boucher, A., Kyriakidis, P. C., and Cronkite-Ratcliff, C. (2008). Geostatistical Solutions for Super-Resolution Land Cover Mapping. *Geoscience and Remote Sensing, IEEE Transactions on, 46*(1), 272-283.

Chiles, J. P., and Delfiner, P. (1999). Geostatistics: Modeling Spatial Uncertainty: by Jean-Paul Chilès and Pierre Delfiner, Wiley, New York, 1999, 695 pp., ISBN 0-471-08315-1, US $125.00. *Computers & Geosciences, 27*(1), 121-123.

Congalton, R. G. (1991). A review of assessing the accuracy of classifications of remotely sensed data. *Remote Sensing of Environment, 37*(1), 35-46.

Cousins, S. A. O., Eriksson, Å., and Franzén, D. (2002). Reconstructing past land use and vegetation patterns using palaeogeographical and archaeological data: A focus on grasslands in Nynäs by the Baltic Sea in south-eastern Sweden. *Landscape and Urban Planning, 61*(1), 1-18.

Curran, P., Milton, E. J., Atkinson, P. M., and Foody, G. M. (1998). Remote sensing from data to understanding.

Dijkstra, H., Oosterbaan, A., and van Blitterswijk, H. (2003). *Kleine landschapselementen. Analyse van de beleidsvraag voor de ontwikkeling van een monitoring systeem* (No. 491). Wageningen.

Domaas, S. T. (2007). The reconstruction of past patterns of tilled fields from historical cadastral maps using GIS. *Landscape Research, 32*(1), 23 - 43.

Erdas, I. (2010). *ERDAS Field Guide*. Norcross: Erdas, Inc.

ERSDAC. (2010, December 28, 2010). User guide version 5.1. Retrieved September 23 2010, from http://www.science.aster.ersdac.or.jp/en/about_aster/index.html

Fisher, P. (1997). The pixel: A snare and a delusion. *International Journal of Remote Sensing, 18*(3), 679-685.

Geman, S., and Geman, D. (1984). Gibbs distributions, and the bayesian restoration of images. *IEEE Transactions on Pattern Analysis and Machine Intelligence, 6*(2), 721-741.

Google. (2011). Google earth. Retrieved 15 December, 2011, from http://www.google.com/earth/index.html

Groom, G., Mucher, C. A., Ihse, M., and Wrbka, T. (2006). Remote sensing in landscape ecology: experiences and perspectives in a European context. *Landscape Ecology, 21*(3), 391-408.

Hailu Kassaye, R. (2006). *Suitability of Markov random field based method for super resolution land cover mapping.* ITC, Enschede.

Hamre, L., Domaas, S., Austad, I., and Rydgren, K. (2007). Land-cover and structural changes in a western Norwegian cultural landscape since 1865, based on an old cadastral map and a field survey. *Landscape Ecology, 22*(10), 1563-1574.

Herben, T., Muenzbergova, Z., Milden, M., Ehrlen, J., Cousins, S., and Eriksson, O. (2006). Long term spatial dynamics of Succisa pratensis in a changing rural landscape: linking dynamical modelling with historical maps. *Journal of Ecology, 94*(1), 131-143.

Hietel, E., Waldhardt, R., and Otte, A. (2005). Linking socio-economic factors, environment and land cover in the German Highlands, 1945-1999. *Journal of Environmental Management, 75*(2), 133-143.

Hirota, M. (2003). Monitoring the Brazilian Atlantic forest cover. *The Atlantic Forest of South America: Biodiversity Status, Threats, and Outlook.(C. Galindo-Leal and I. Gusmão Camara). Island Press, Washington, DC*, 60-65.

Jensen, J. (1986). Introduction to digital image processing. *Englewood cliff: University of South Carolina.*

Jupp, D. L. B., Strahler, A. H., and Woodcock, C. E. (1988). Autocorrelation and regularization in digital images. I. Basic theory. *Geoscience and Remote Sensing, IEEE Transactions on, 26*(4), 463-473.

Kasetkasem, T., Arora, M. K., and Varshney, P. K. (2005). Super-resolution land cover mapping using a Markov random field based approach. [doi: DOI: 10.1016/j.rse.2005.02.006]. *Remote Sensing of Environment, 96*(3-4), 302-314.

Kumar Bist, G. (2009). *Detection of roads from remote sensing with super resolution mapping.* Enschede: ITC.

Li, S. Z. (2009). *Markov random field modeling in image analysis*: Springer-Verlag New York Inc.

Marroquin, J., Mitter, S., and Poggio, T. (1987). Probabilistic solution of ill-posed problems in computational vision. *Journal of the American Statistical Association*, 76-89.

Mertens, K. C., De Baets, B., Verbeke, L., and de Wulf, R. (2006). A sub-pixel mapping algorithm based on sub-pixel/pixel spatial attraction models. *International Journal of Remote Sensing, 27*(15), 3293-3310.

Mertens, K. C., Verbeke, L., Ducheyne, E., and De Wulf, R. (2003). Using genetic algorithms in sub-pixel mapping. *International Journal of Remote Sensing, 24*(21), 4241-4247.

Mertens, K. C., Verbeke, L. P. C., Westra, T., and De Wulf, R. R. (2004). Sub-pixel mapping and sub-pixel sharpening using neural network predicted wavelet coefficients. *Remote Sensing of Environment, 91*(2), 225-236.

Minnemeyer, S. (2002). Global Forest Watch: Mapping and Monitoring Forest Development. Retrieved 10 December, 2011, from http://proceedings.esri.com/library/userconf/proc02/pap0531/p0531.htm

Oosterbaan, A., and Pels, M. (2007). Monitoring of small landscape elements in the Netherlands. *Landscape Research, 32*(1), 95-102.

Panaguiton, L., Eustaquio, R., and Campo, P. (1999). Urban sprawl assessment in the Mount Makiling forest reserve [Philippines] using remote sensing and GIS [geographic information system] technologies.

Rosenqvist, Å. (1996). The global rain forest mapping project by JERS-1 SAR. *International Archives of Photogrammetry and Remote Sensing, 31*, 594-598.

Saleh, M., Kartikasari, R., Febrianti, L., Fitria, W., Prasetyo, A., Hakim, L., et al. THE USE OF SATELLITE DATA AND GIS IN MONITORING OF INDONESIA FOREST COVER.

Sheeren, D., Bastin, N., Ouin, A., Ladet, S., Balent, G., and Lacombe, J. P. (2009). Discriminating small wooded elements in rural landscape from aerial photography: a hybrid pixel/object-based analysis approach. [Article]. *International Journal of Remote Sensing, 30*(19), 4979-4990.

Sikazwe, J. (2007). *Optimizing Markov random field for super - resolution land cover mapping.* Enschede: ITC.

Skalos, J., and Engstova, B. (2010). Methodology for mapping non-forest wood elements using historic cadastral maps and aerial photographs as a basis for management. *Journal of Environmental Management, 91*(4), 831-843.

Sklenicka, P., and Lhota, T. (2002). Landscape heterogeneity--a quantitative criterion for landscape reconstruction. *Landscape and Urban Planning, 58*(2-4), 147-156.

Solberg, A. H. S., Taxt, T., and Jain, A. K. (1996). A Markov random field model for classification of multisource satellite imagery. *Geoscience and Remote Sensing, IEEE Transactions on, 34*(1), 100-113.

Stone, T. A., Brown, I. F., and Woodwell, G. M. (1991). Estimation, by remote sensing, of deforestation in central Rondônia, Brazil. *Forest Ecology and Management, 38*(3-4), 291-304.

Strahler, A. H., Woodcock, C. E., and Smith, J. A. (1986). On the nature of models in remote sensing. *Remote Sensing of Environment, 20*(2), 121-139.

Tatem, A. J., Lewis, H., Atkinson, P., and Nixon, M. (2002a). Super-resolution land cover pattern prediction using a Hopfield neural network. *Remote Sensing of Environment, 79*(1), 1-14.

Tatem, A. J., Lewis, H., Atkinson, P., and Nixon, M. (2002b). Super-resolution target identification from remotely sensed images using a Hopfield neural network. *Geoscience and Remote Sensing, IEEE Transactions on, 39*(4), 781-796.

Thornton, M. W., Atkinson, P. M., and Holland, D. A. (2006). Sub-pixel mapping of rural land cover objects from fine spatial resolution satellite sensor imagery using super-resolution pixel-swapping. *International Journal of Remote Sensing, 27*(3), 473 - 491.

Tolpekin, V. A., Ardila Lopez, J. P., and Bijker, W. (2010). Super - resolution mapping for extraction of urban tree crown objects from VHR satellite images. *In: GEOBIA 2010 : geographic object - based image analysis, 29 June-2 July 2010, Ghent, Belgium : proceedings / editor E.A. Addink, F.M.B. Van Coillie. - [s.l.] : International Society for Photogrammetry and Remote Sensing (ISPRS), 2010. - (International Archives of Photogrammetry and Remote Sensing : IAPRS : ISPRS ; XXXVIII-4/C7), 7 p.*

Tolpekin, V. A., and Stein, A. (2009). Quantification of the Effects of Land-Cover-Class Spectral Separability on the Accuracy of Markov-Random-Field-Based Superresolution Mapping. *Ieee Transactions on Geoscience and Remote Sensing, 47*(9), 3283-3297.

Tso, B., and Mather. (2009). *Classification Methods for Remotely Sensed Data* (Second Edition ed.): Taylor & Francis Group, LLC.

Van Ede, R., Sluiter, R., and Jong, S. D. (2004). Destriping and geometric correction of an ASTER level 1a image. *Faculty of GeoSciences, Dept. of Physical Geography, Utrecht University*.

Van Eetvelde, V., and Antrop, M. (2004). Analyzing structural and functional changes of traditional landscapes--two examples from Southern France. *Landscape and Urban Planning, 67*(1-4), 79-95.

Vega, B. (2005). *Image fusion of optical and microwave data to assess criteria and indicator C&I related to forest encroachment, for certification process of sustainable forest management SFM : case study in Berau, East Kalimantan, Indonesia.* ITC, Enschede.

Vega, B., Hussin, Y. A., and Sharifi, A. (2006). *Optical and microwave image fusion to detect and monitor illegal logging and tropical rain forest encroachment in east Kalimantan, Indonesia*

Verhoeye, J., and De Wulf, R. (2002). Land cover mapping at sub-pixel scales using linear optimization techniques. *Remote Sensing of Environment, 79*(1), 96-104.

Vuorela, N., Alho, P., and Kalliola, R. (2002). Systematic Assessment of Maps as Source Information in Landscape-change Research. *Landscape Research, 27*(2), 141 - 166.

Walker, R. The scale of forest transition: Amazonia and the Atlantic forests of Brazil. *Applied Geography, In Press, Corrected Proof.*

Welikanna, D. R. (2008). *Analysis of the effectiveness of spectral mixture analysis and Markov random field based super resolution mapping in the context of urban composition.* ITC, Indian Institute of Remote Sensing (IIRS), Enschede, Dehradun.

Woodcock, C. E., and Strahler, A. H. (1987). The factor of scale in remote sensing. *Remote Sensing of Environment, 21*(3), 311-332.

Zhang, Y., Heipke, C., Butenuth, M., and Hu, X. (2006). Automatic extraction of wind erosion obstacles by integration of GIS data, DSM and stereo images. *International Journal of Remote Sensing, 27*(8), 1677 - 1690.

APPENDIX A

Class statistics for image of Buurserzand Study area

Class separability (Transformed Divergence) in image of Buurserzand Study area

Class Name	Heath	Waterbody	Trees	Baresoil
Heath	0.000	1.988	1.999	1.999
Waterbody	1.988	0.000	2.000	2.000
Trees	1.999	2.000	0.000	2.000
Baresoil	1.999	2.000	2.000	0.000

Class mean vectors for Image of Buurserzand Study area

Class Name	Band1	Band2	Band3
Heath	41.126812	26.746377	49.000000
Waterbody	36.952206	19.665441	27.816176
Trees	41.499020	22.737255	74.861765
Baresoil	55.769392	44.310273	57.343816

Class covariances for Image of Twente Study area

Heath	Band1	Band2	Band3
Band1	3.609315	3.261370	5.029091
Band2	3.261370	3.942714	4.738182
Band3	5.029091	4.738182	16.450909

Waterbody	Band1	Band2	Band3
Band1	2.274460	1.696128	-0.399962
Band2	1.696128	2.393192	1.355247
Band3	-0.399962	1.355247	16.025125

Trees	Band1	Band2	Band3
Band1	7.875367	3.512009	31.067087
Band2	3.512009	2.945618	9.652554
Band3	31.067087	9.652554	172.466643

Baresoil	Band1	Band2	Band3
Band1	37.791246	35.699853	19.050041
Band2	35.699853	45.584201	19.372091
Band3	19.050041	19.372091	41.793307

Class statistics for image of Rutland Study area

Class separability (Transformed Divergence) in image of Rutland Study area

Class Name	Forest	Waterbody	Encroached_area
Forest	0.000	2.000	2.000
Waterbody	2.000	0.000	1.962
Encroached_area	2.000	1.962	0.000

Class mean vectors for Image of Rutland Study area

Class Name	Band1	Band2	Band3
Forest	46.313402	51.104651	64.386719
Waterbody	24.352577	33.732558	49.371094
Encroached_area	77.107216	37.325581	63.832031

Class covariances for Image of Rutland Study area

Forest	Band1	Band2	Band3
Band1	3.194965	1.424397	8.594428
Band2	1.424397	1.951879	2.792698
Band3	8.594428	2.792698	51.909968

Waterbody	Band1	Band2	Band3
Band1	12.118331	13.275376	3.730233
Band2	13.275376	19.868810	6.535157
Band3	3.730233	6.535157	146.480985

Encroached_area	Band1	Band2	Band3
Band1	63.892999	59.495144	-2.181847
Band2	59.495144	76.461749	1.066498
Band3	-2.181847	1.066498	23.042264

Image showing training site selection for Study area- I

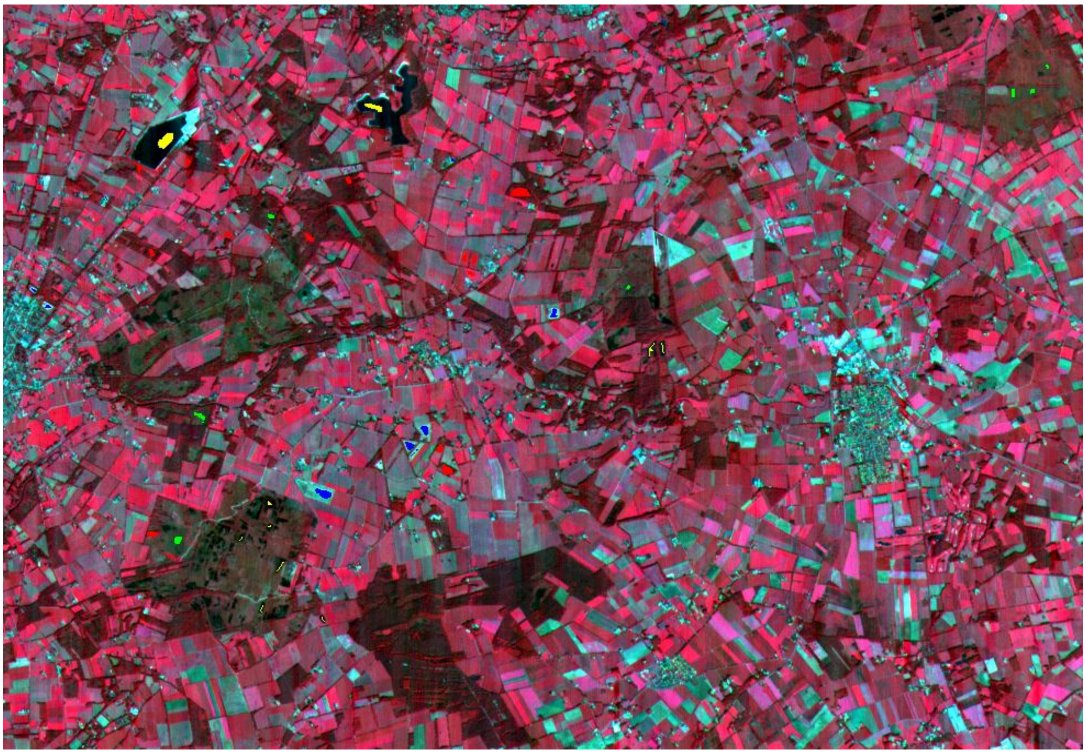

Image showing training site selection for study area- II

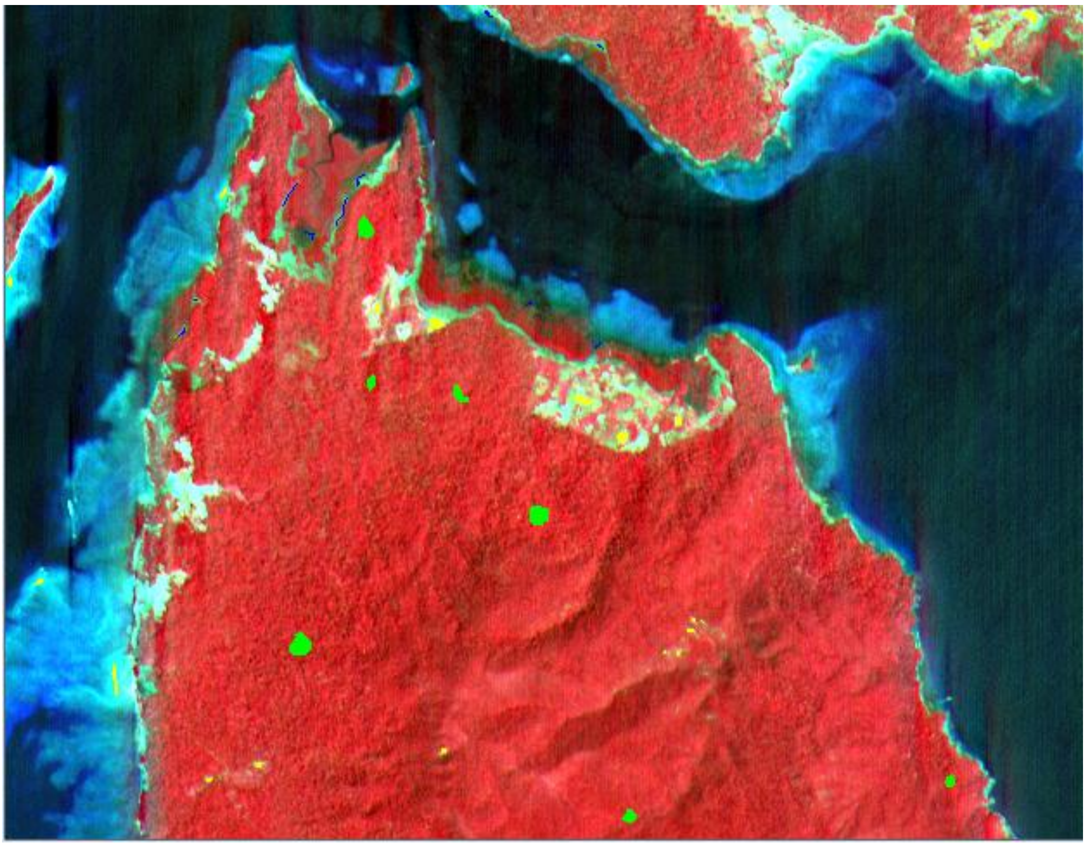

APPENDIX B

Experimentation results for identification of optimal lambda value at S=2,3...10

Lambda	Mean	Stdev
0.1	0.458605	0.01407
0.2	0.464176	0.013902
0.3	0.478686	0.013875
0.4	0.487862	0.012835
0.5	0.508987	0.02549
0.6	0.547744	0.01913
0.7	0.640337	0.018142
0.8	0.689711	0.022073
0.85	0.692309	0.016731
0.9	0.707761	0.019054
0.95	0.687659	0.043516
0.99	0.349087	0.293592

Lambda	Mean	Stdev
0.1	0.450418	0.010376
0.2	0.491349	0.009077
0.3	0.489408	0.008631
0.4	0.518586	0.016425
0.5	0.560628	0.017304
0.6	0.622374	0.016906
0.7	0.683423	0.013248
0.8	0.708849	0.019235
0.85	0.704973	0.012617
0.9	0.724175	0.02614
0.95	0.691414	0.068472
0.99	0.372531	0.238034

Lambda	Mean	Stdev
0.1	0.459612	0.008172
0.2	0.487508	0.011844
0.3	0.516041	0.006957
0.4	0.544042	0.013982
0.5	0.606771	0.015397
0.6	0.658596	0.020341
0.7	0.688934	0.013442
0.8	0.71036	0.022792
0.85	0.736067	0.028045
0.9	0.709526	0.039869
0.95	0.709526	0.039869
0.99	0.658925	0.055226

Lambda	Mean	Stdev
0.1	0.474249	0.009451
0.2	0.503801	0.01019
0.3	0.534562	0.016979
0.4	0.577712	0.009067
0.5	0.629107	0.014685
0.6	0.667754	0.023254
0.7	0.696275	0.024633
0.8	0.71106	0.019905
0.85	0.715911	0.04281
0.9	0.708288	0.057178
0.95	0.655615	0.086707
0.99	0.269072	0.133437

Lambda	Mean	Stdev
0.1	0.487577	0.007541
0.2	0.514429	0.011733
0.3	0.557493	0.016479
0.4	0.607314	0.014849
0.5	0.653282	0.010481
0.6	0.682835	0.021465
0.7	0.695832	0.021249
0.8	0.705439	0.028099
0.85	0.705514	0.053711
0.9	0.640393	0.078303
0.95	0.545308	0.123004
0.99	0.188259	0.126123

Lambda	Mean	Stdev
0.1	0.492411	0.008646
0.2	0.565739	0.015011
0.3	0.017946	0.017946
0.4	0.642132	0.014423
0.5	0.669324	0.024798
0.6	0.674486	0.019439
0.7	0.666615	0.029488
0.8	0.610061	0.04922
0.85	0.589598	0.042067
0.9	0.559879	0.048543
0.95	0.409188	0.117016
0.99	0.207316	0.133518

Table showing results for Window size optimization

	stdk			
Lambda	W=3	W=5	W=7	W=9
0.1	0.008646	0.063753	0.008222	0.00166
0.2	0.015011	0.009883	0.015767	0.001356
0.3	0.017946	0.020889	0.009361	0.001295
0.4	0.014423	0.013464	0.014147	0.003694
0.5	0.024798	0.023607	0.017335	0.006339
0.6	0.019439	0.022486	0.021215	0.014786
0.7	0.029488	0.03594	0.019916	0.050994
0.8	0.04922	0.069432	0.051283	0.197889
0.85	0.042067	0.063753	0.087665	0.002189
0.9	0.048543	0.072528	0.116524	0.002757
0.95	0.117016	0.11613	0.29549	0.002353
0.99	0.133518	0.171864	0.167842	0.211912

	meank			
Lambda	W=3	W=5	W=7	W=9
0.1	0.492411	0.516889	0.541291	0.638005
0.2	0.565739	0.618334	0.657064	0.721774
0.3	0.599575	0.675855	0.709368	0.734546
0.4	0.642132	0.705189	0.722152	0.733761
0.5	0.669324	0.71978	0.717668	0.725236
0.6	0.674486	0.728768	0.718528	0.696097
0.7	0.666615	0.737618	0.740988	0.6
0.8	0.610061	0.7152	0.730449	0.216897
0.85	0.589598	0.676373	0.717219	0.004777
0.9	0.559879	0.637702	0.625151	0.003412
0.95	0.409188	0.389023	0.09773	0.001102
0.99	0.207316	0.276802	0.09773	0.079865

Resultant plot for SLE site 2 experiment at S=2

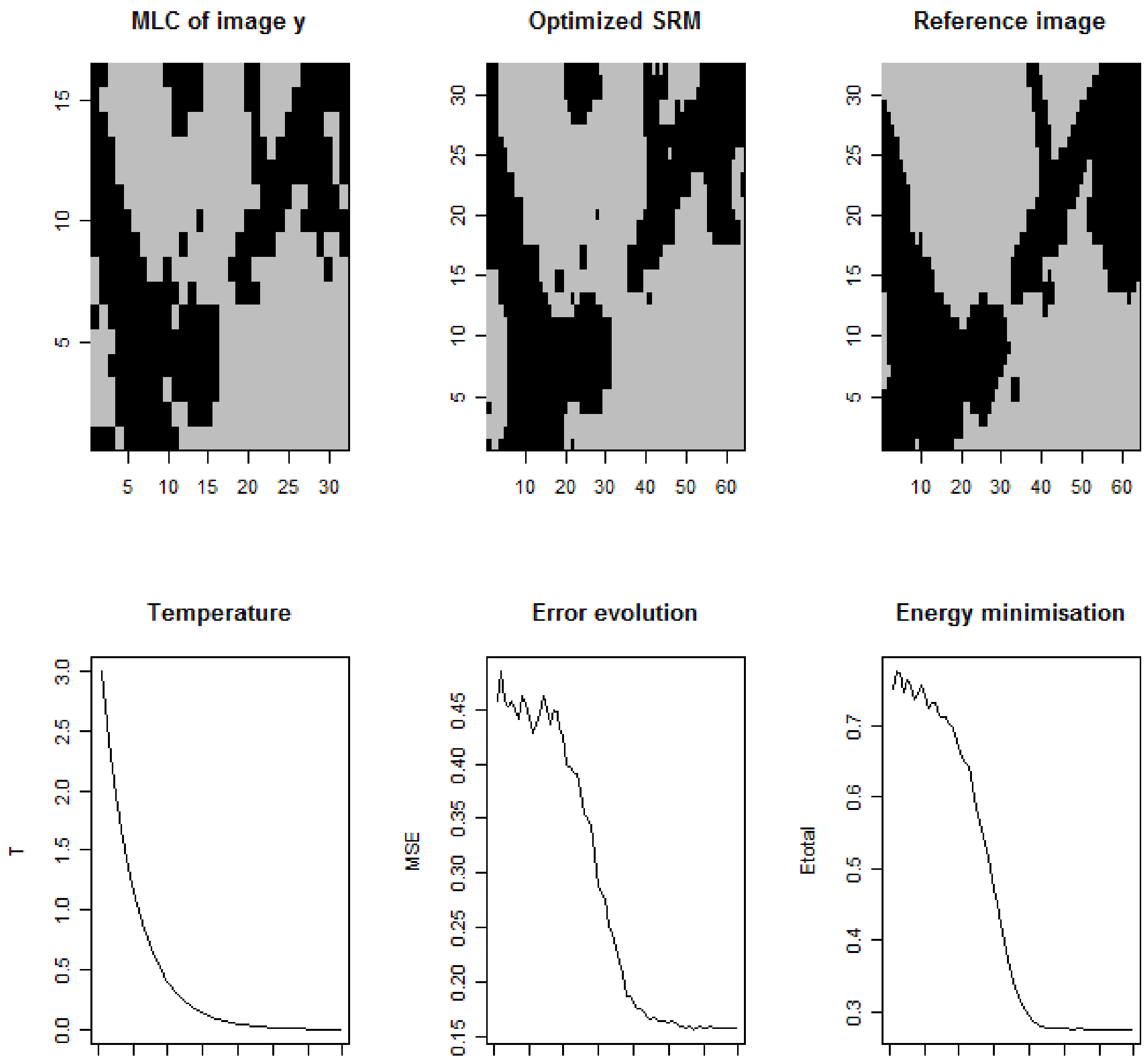

Resultant plot for SLE site 1 experiment from S=2,3…,10

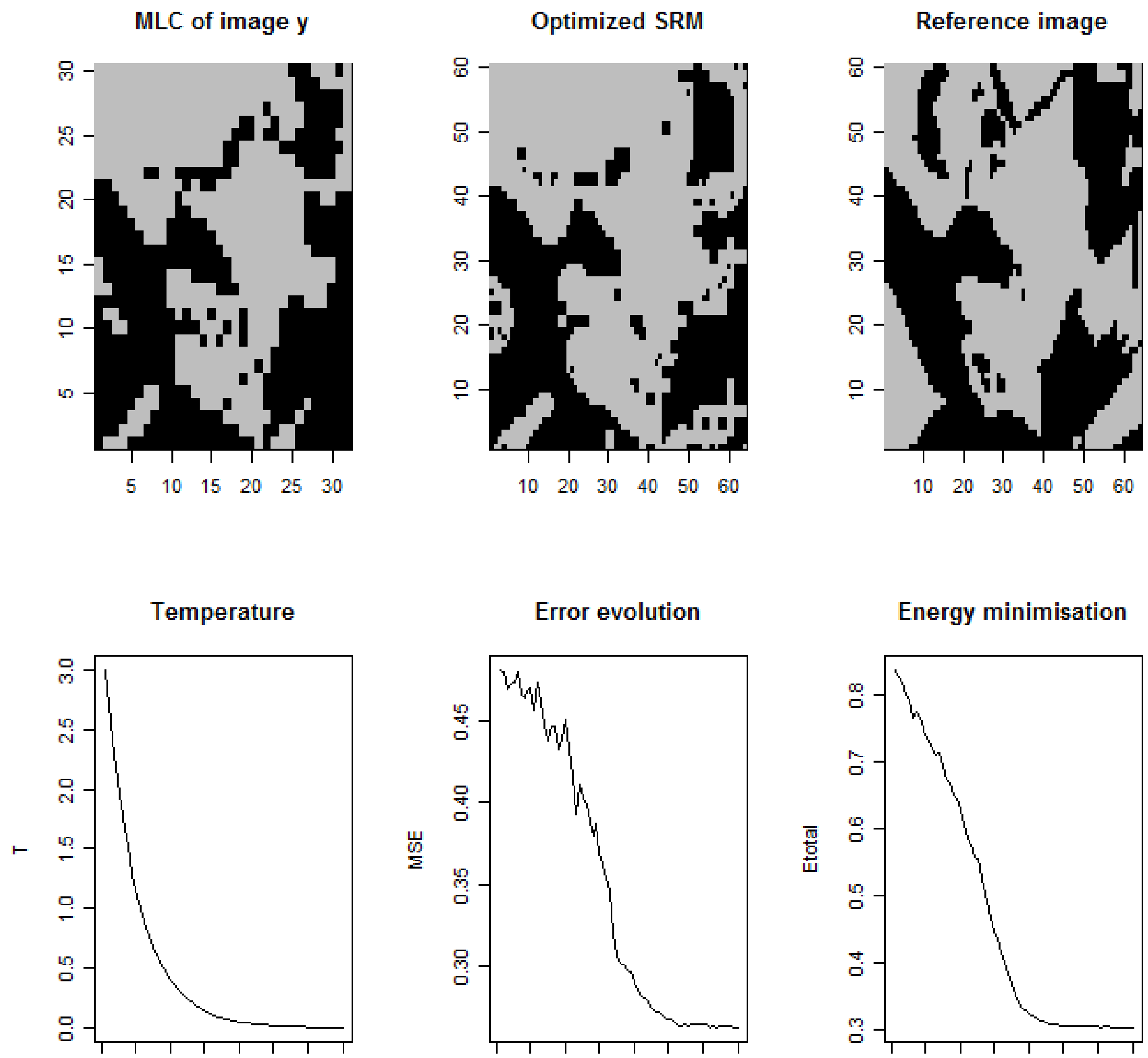

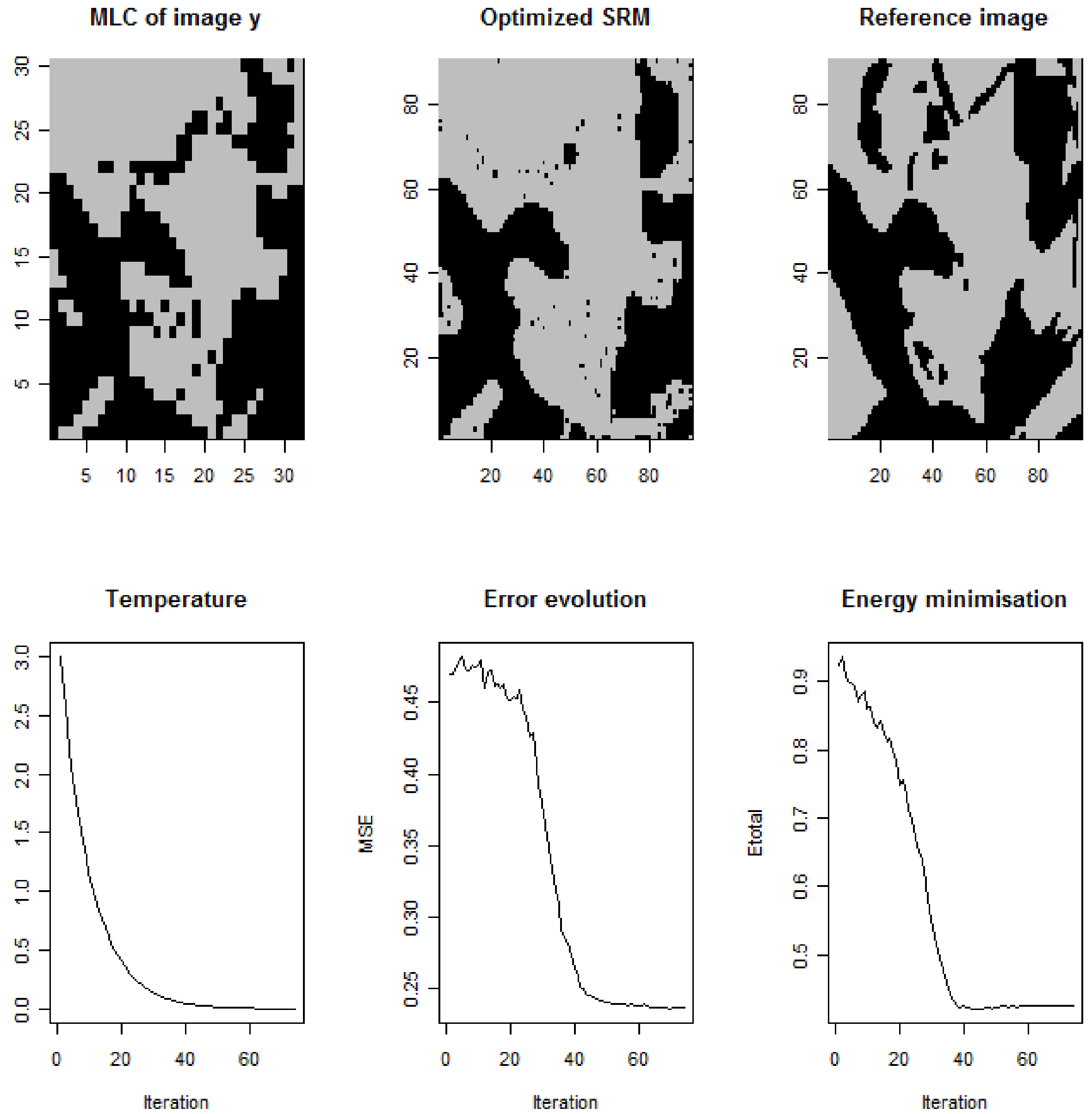

MLC of image y
Optimized SRM
Reference image
Temperature
Error evolution
Energy minimisation
MSE
Etotal
Iteration

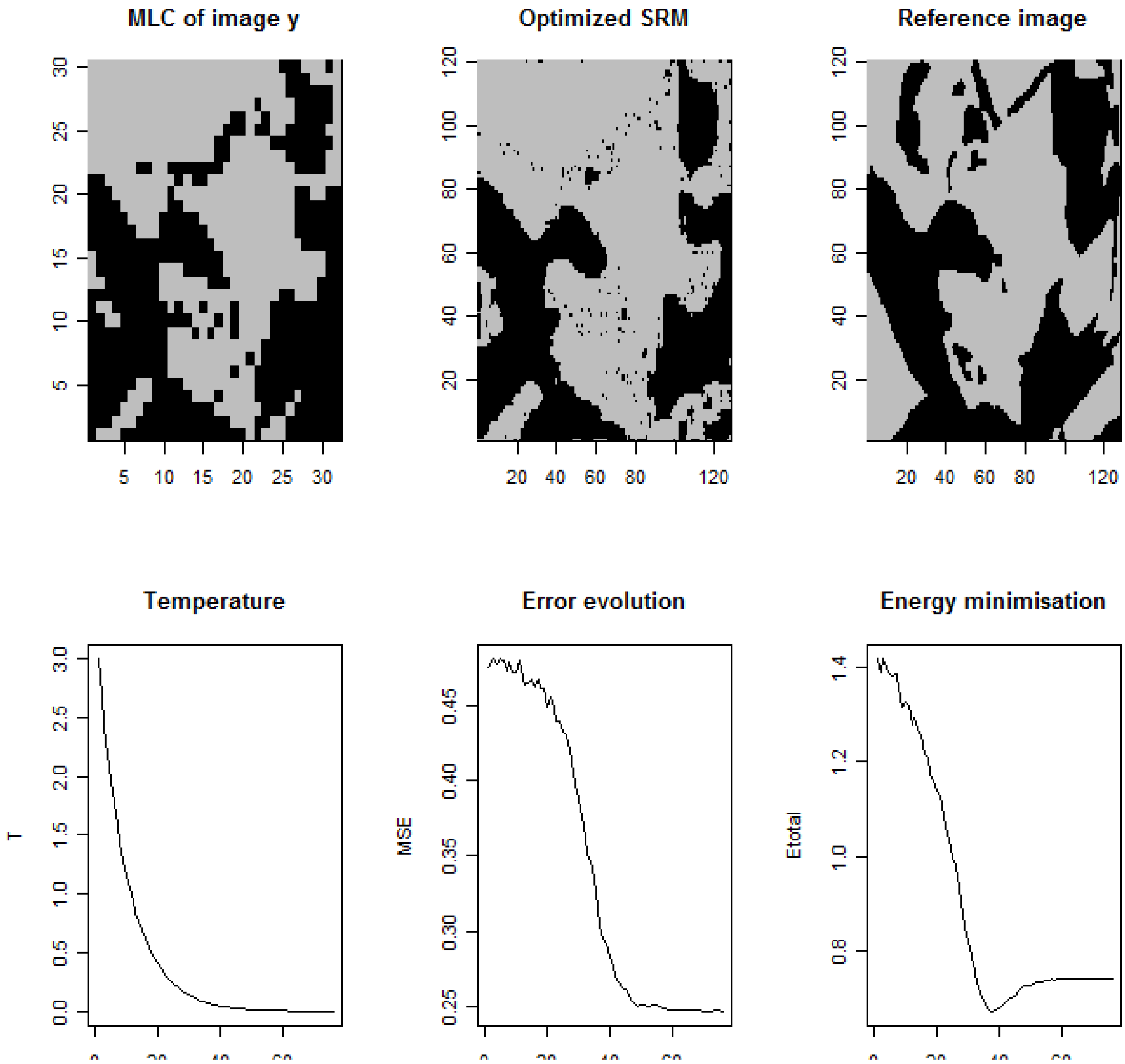
MLC of image y
Optimized SRM
Reference image
Temperature
T
Error evolution
MSE
Energy minimisation
Etotal

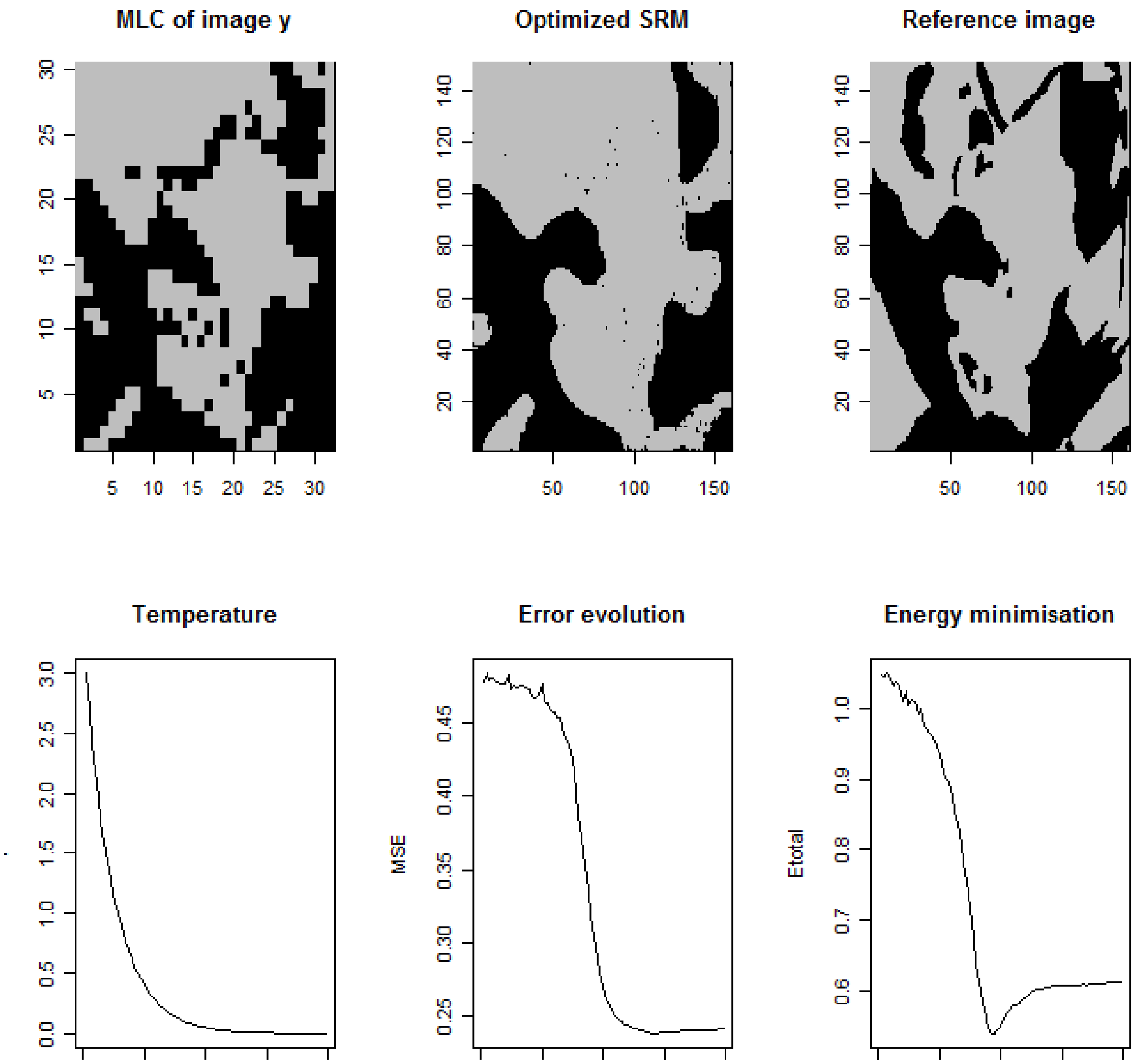
MLC of image y
Optimized SRM
Reference image
Temperature
Error evolution
MSE
Energy minimisation
Etotal

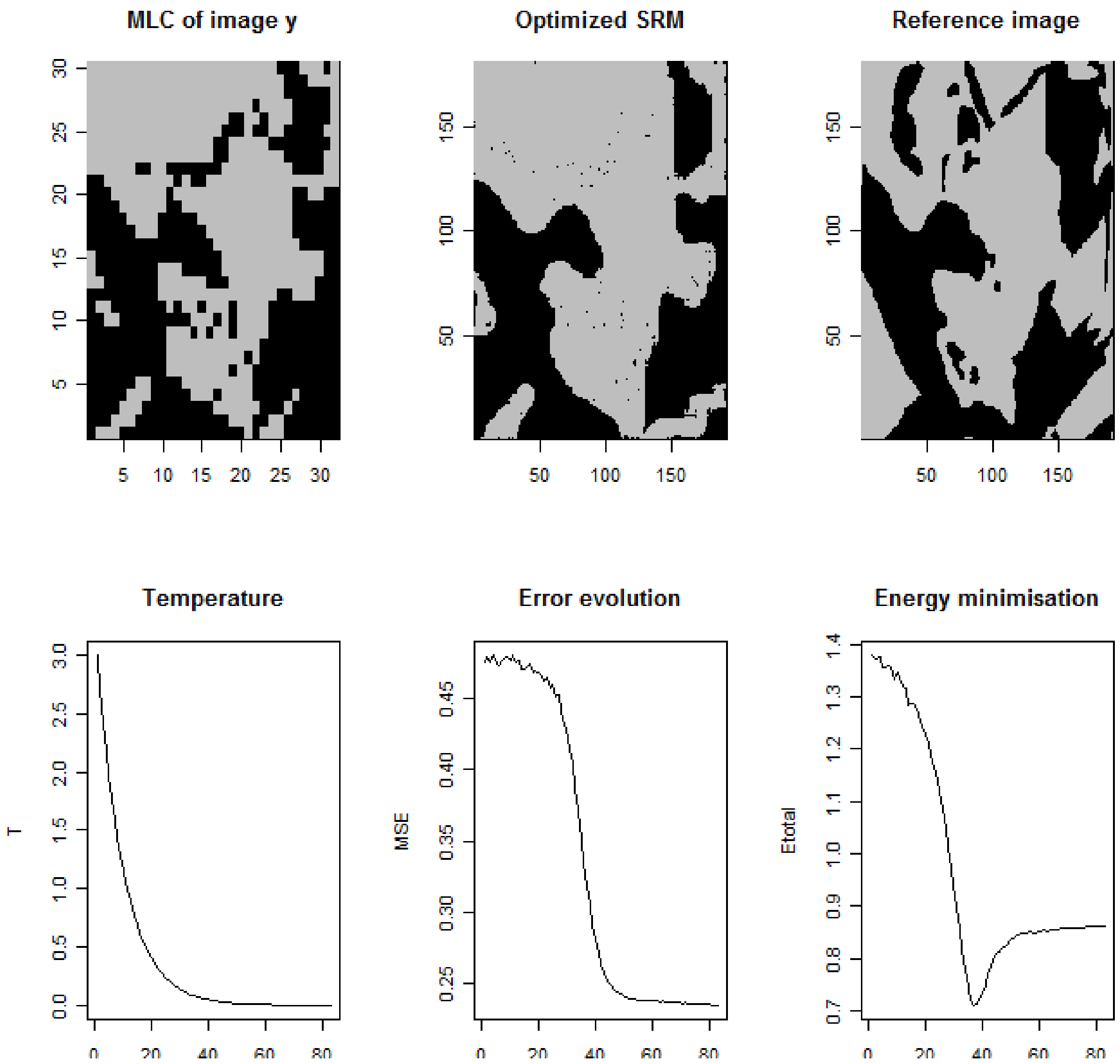
MLC of image y
Optimized SRM
Reference image
Temperature
Error evolution
Energy minimisation
T
MSE
Etotal

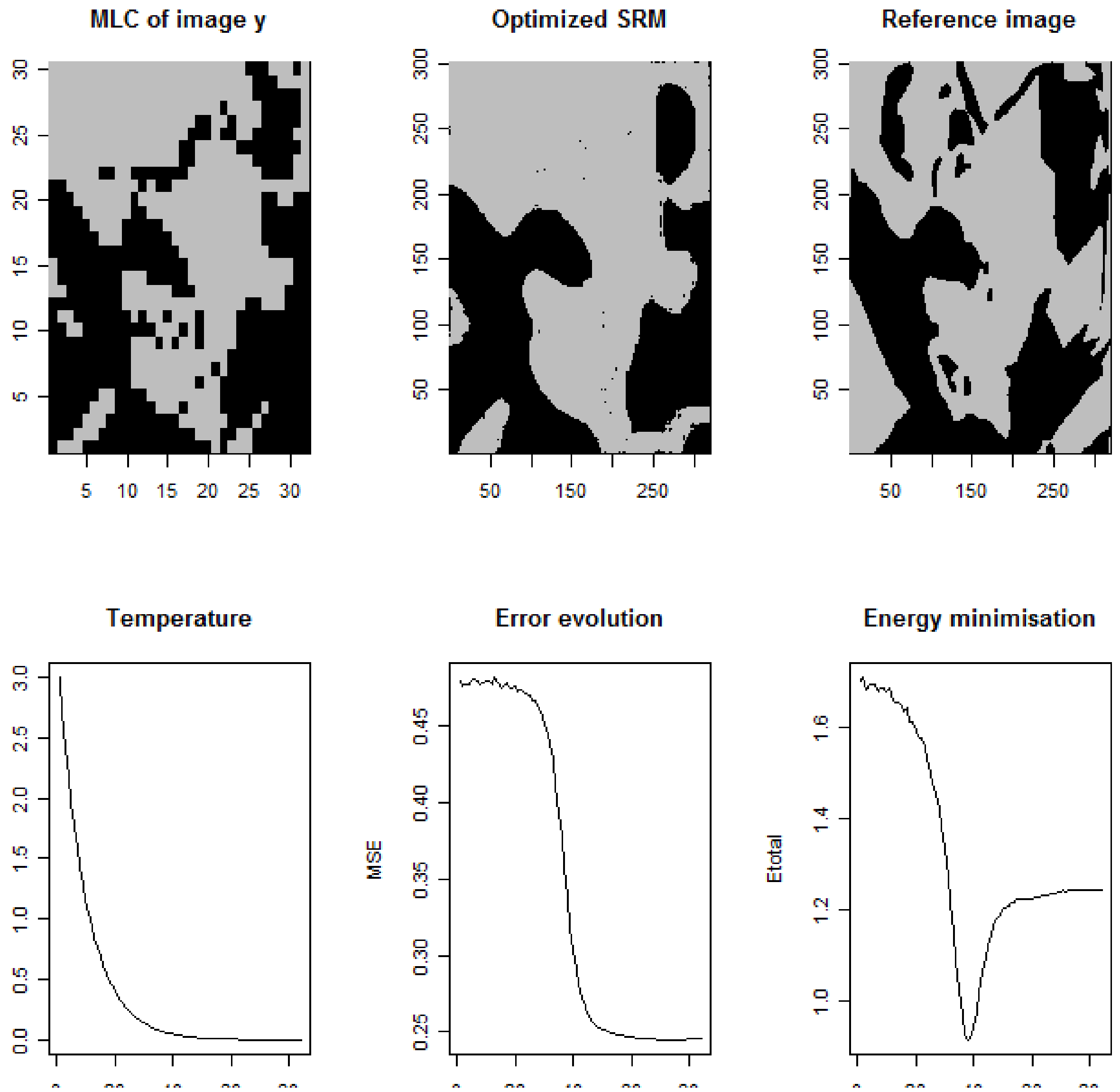
MLC of image y
Optimized SRM
Reference image
Temperature
Error evolution
Energy minimisation
MSE
Etotal

Resultant plot for Fe site 2 experiment at S=2

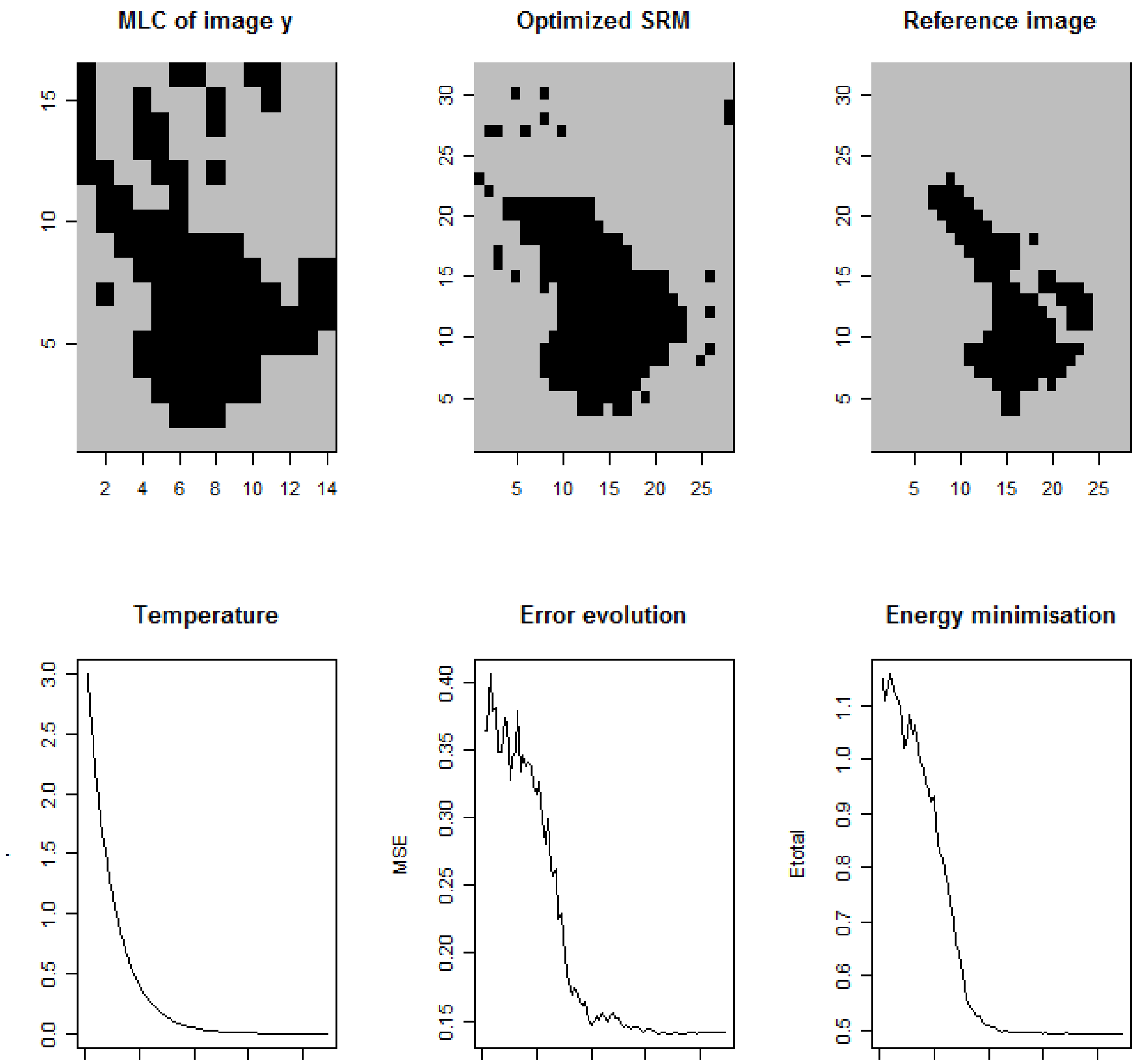

Resultant plot for Fe site 3 experiment at S=2

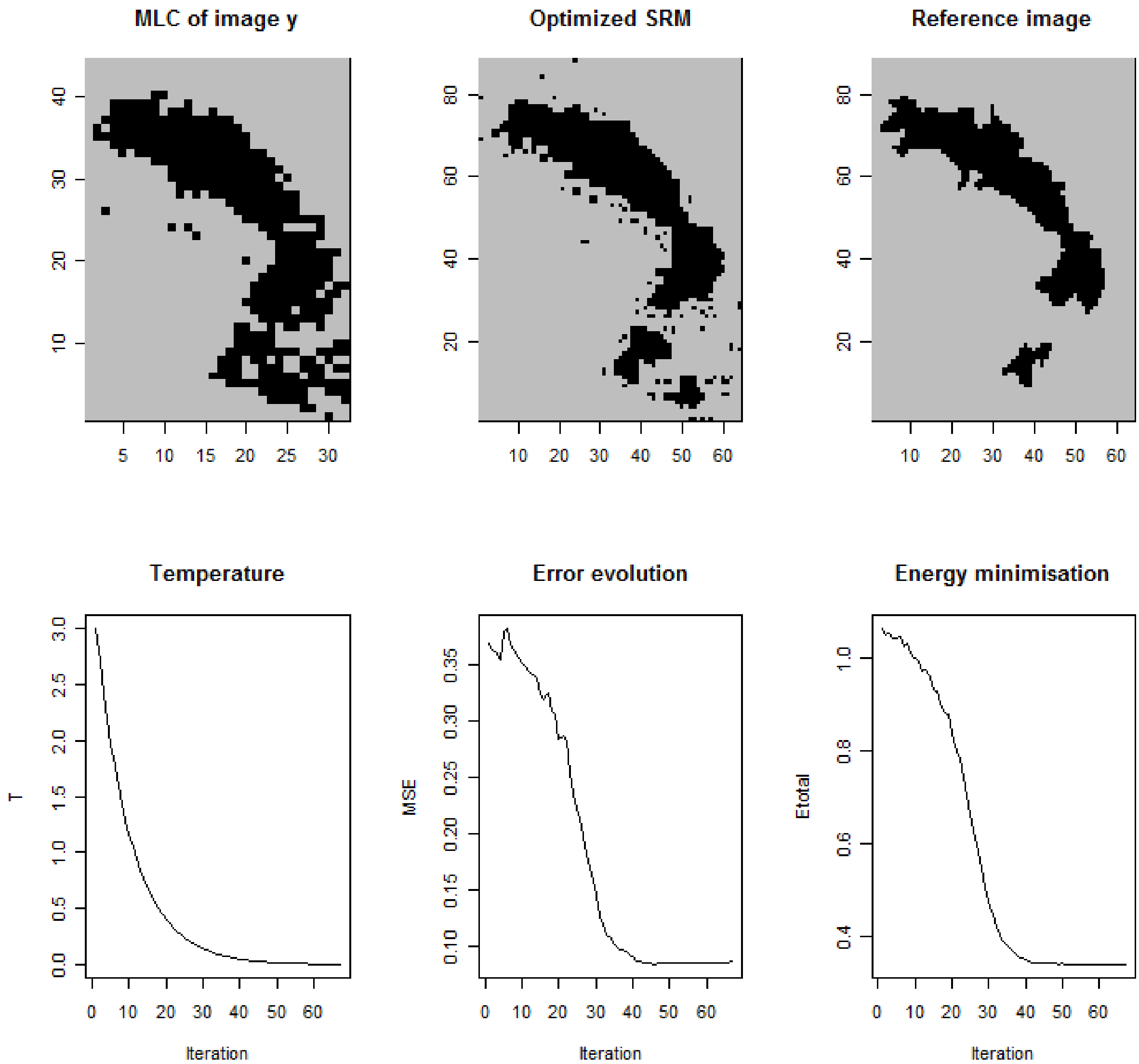

Resultant plot for Fe site 1 experiment from S=2,3...10

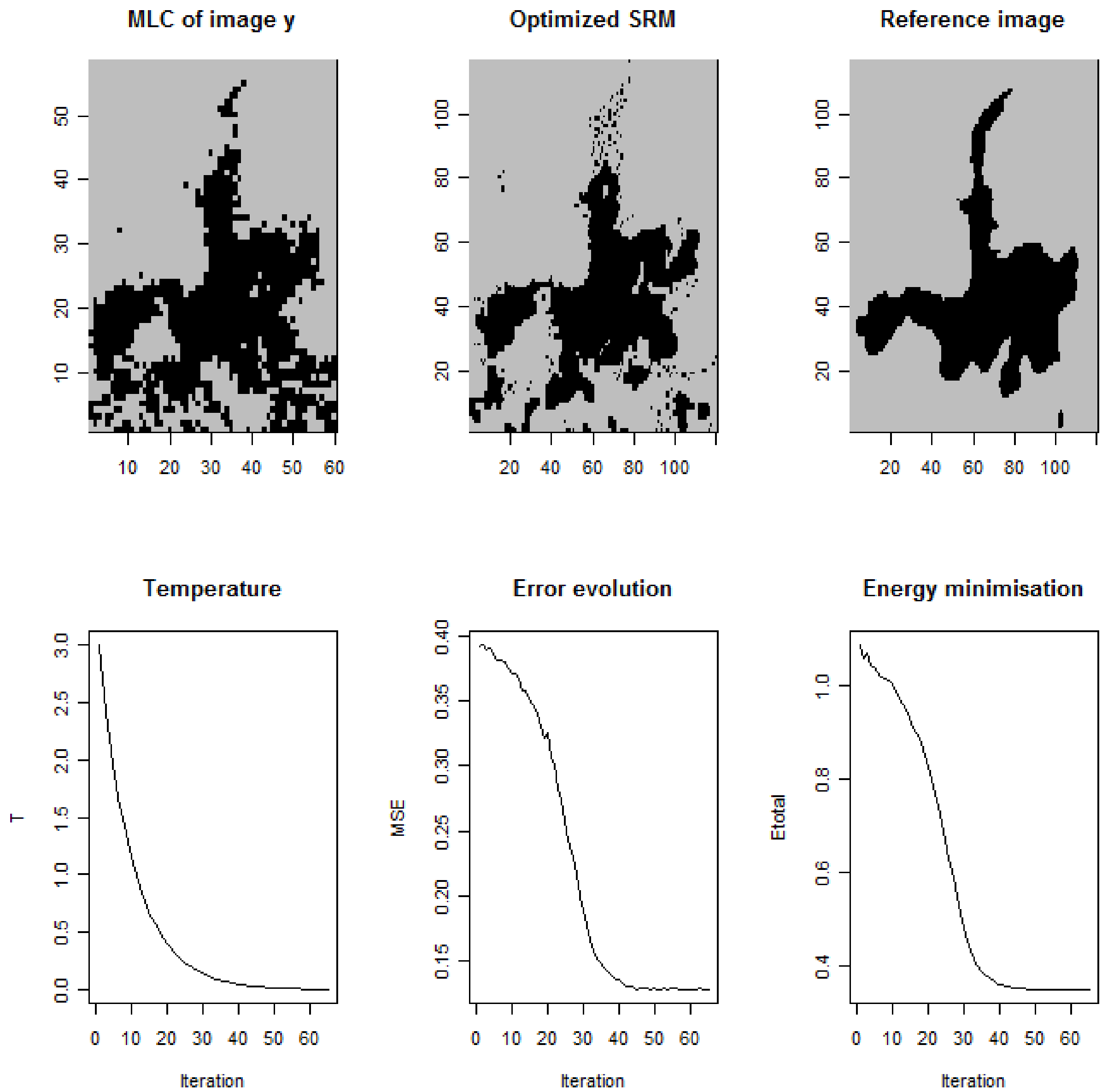

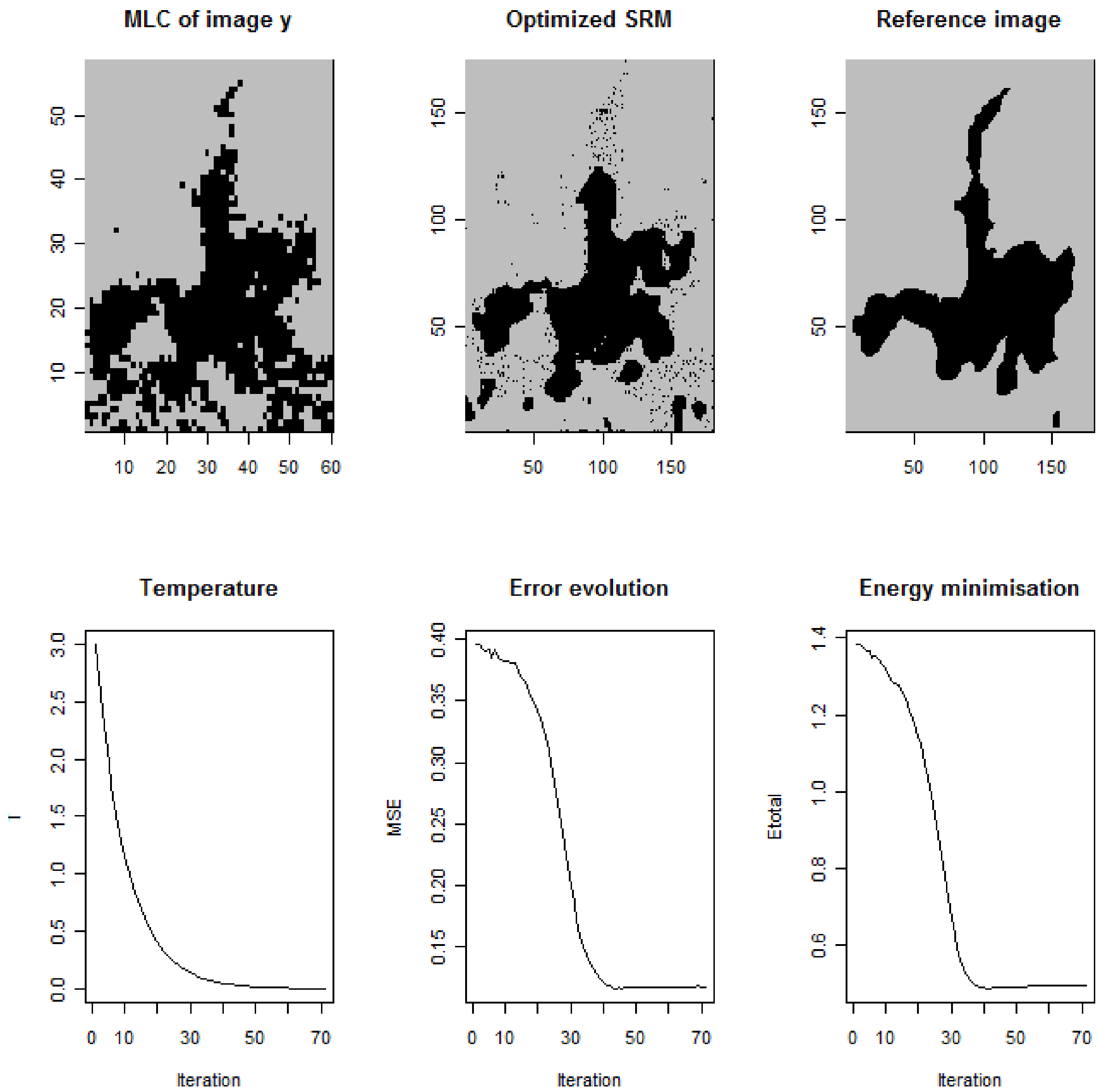
MLC of image y
Optimized SRM
Reference image
Temperature
Error evolution
Energy minimisation
T
MSE
Etotal
Iteration
Iteration
Iteration

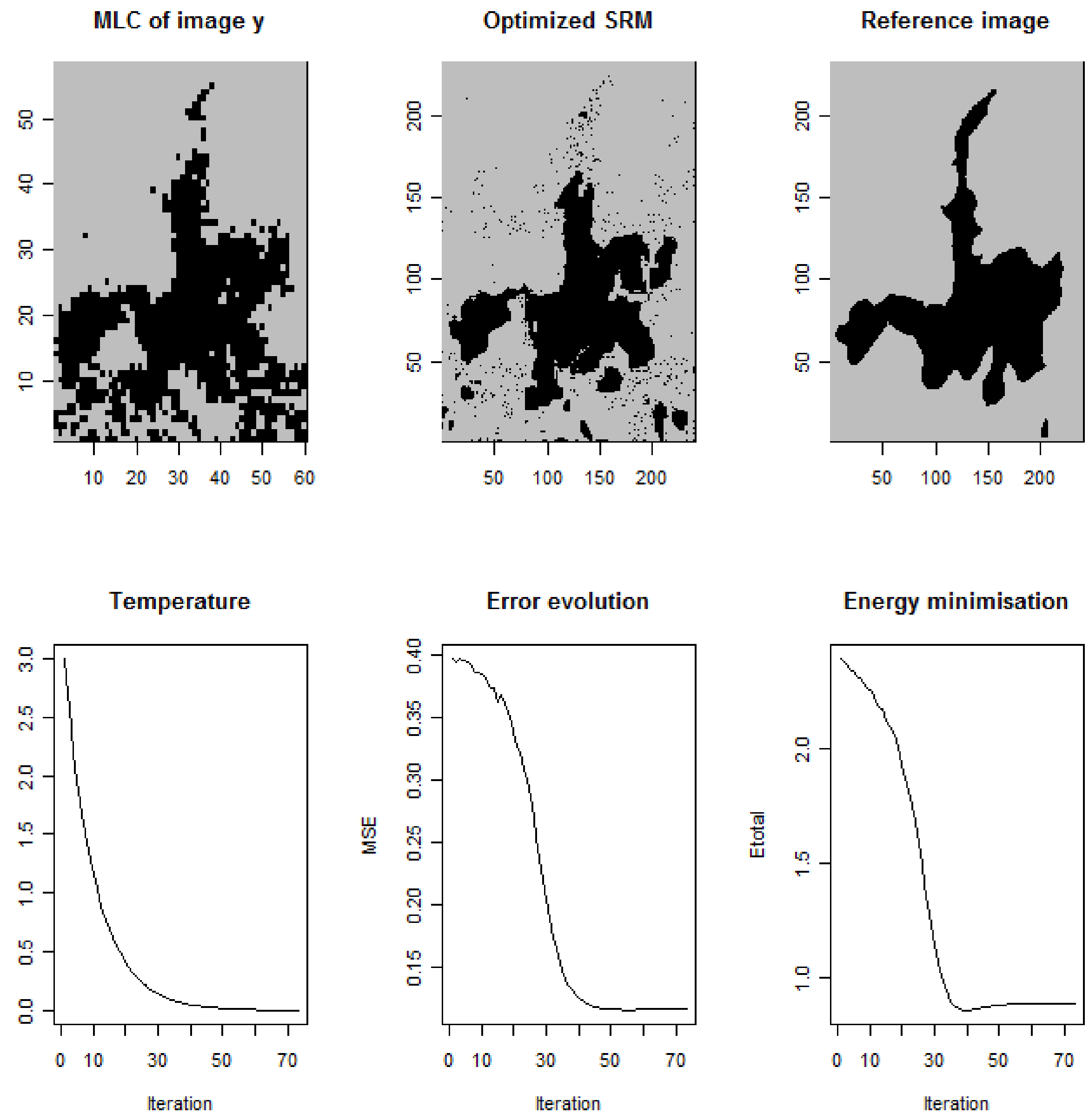
MLC of image y
Optimized SRM
Reference image
Temperature
Error evolution
MSE
Energy minimisation
Etotal
Iteration
Iteration
Iteration

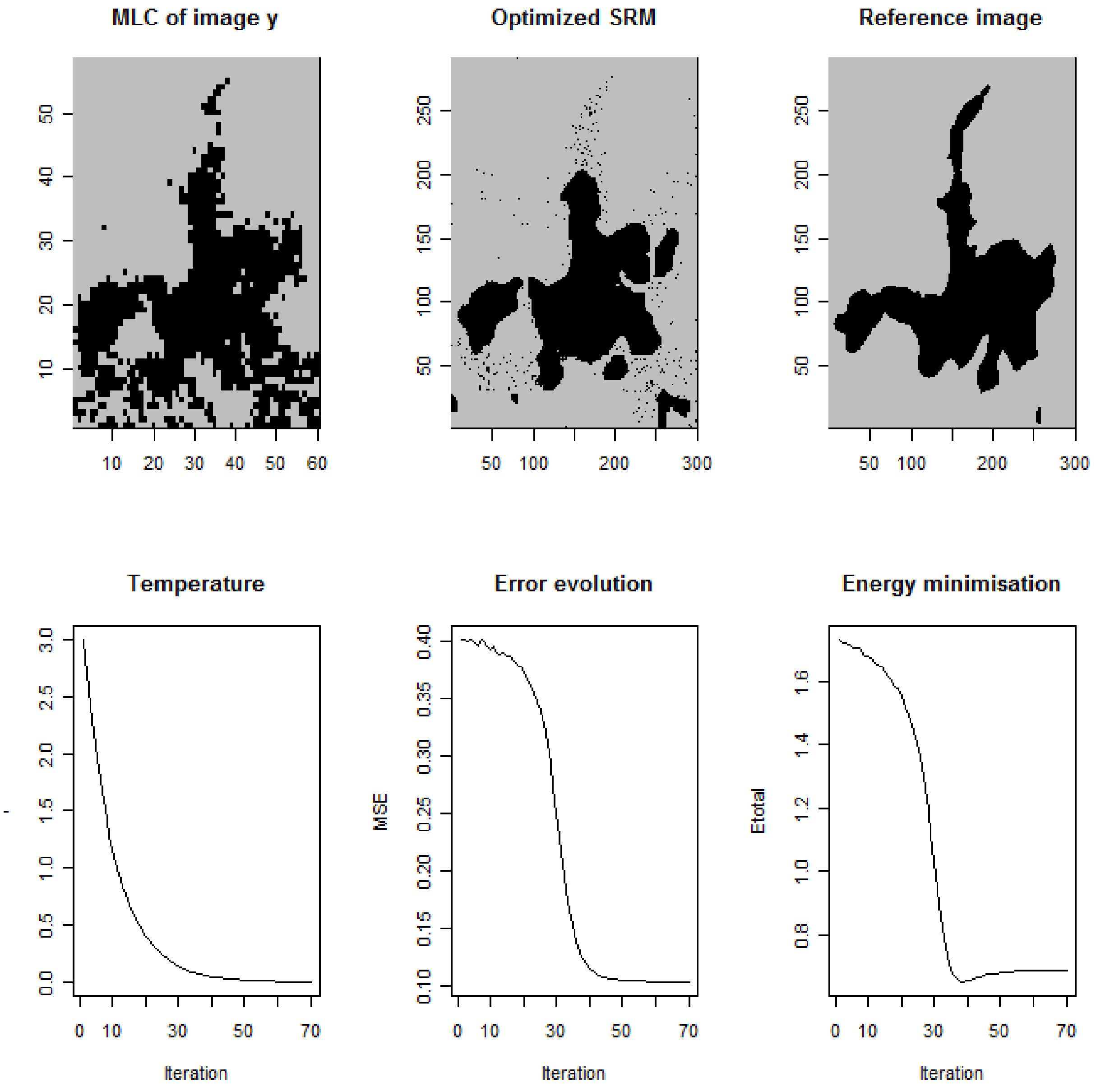
MLC of image y
Optimized SRM
Reference image
Temperature
Error evolution
Energy minimisation
MSE
Etotal
Iteration
Iteration
Iteration

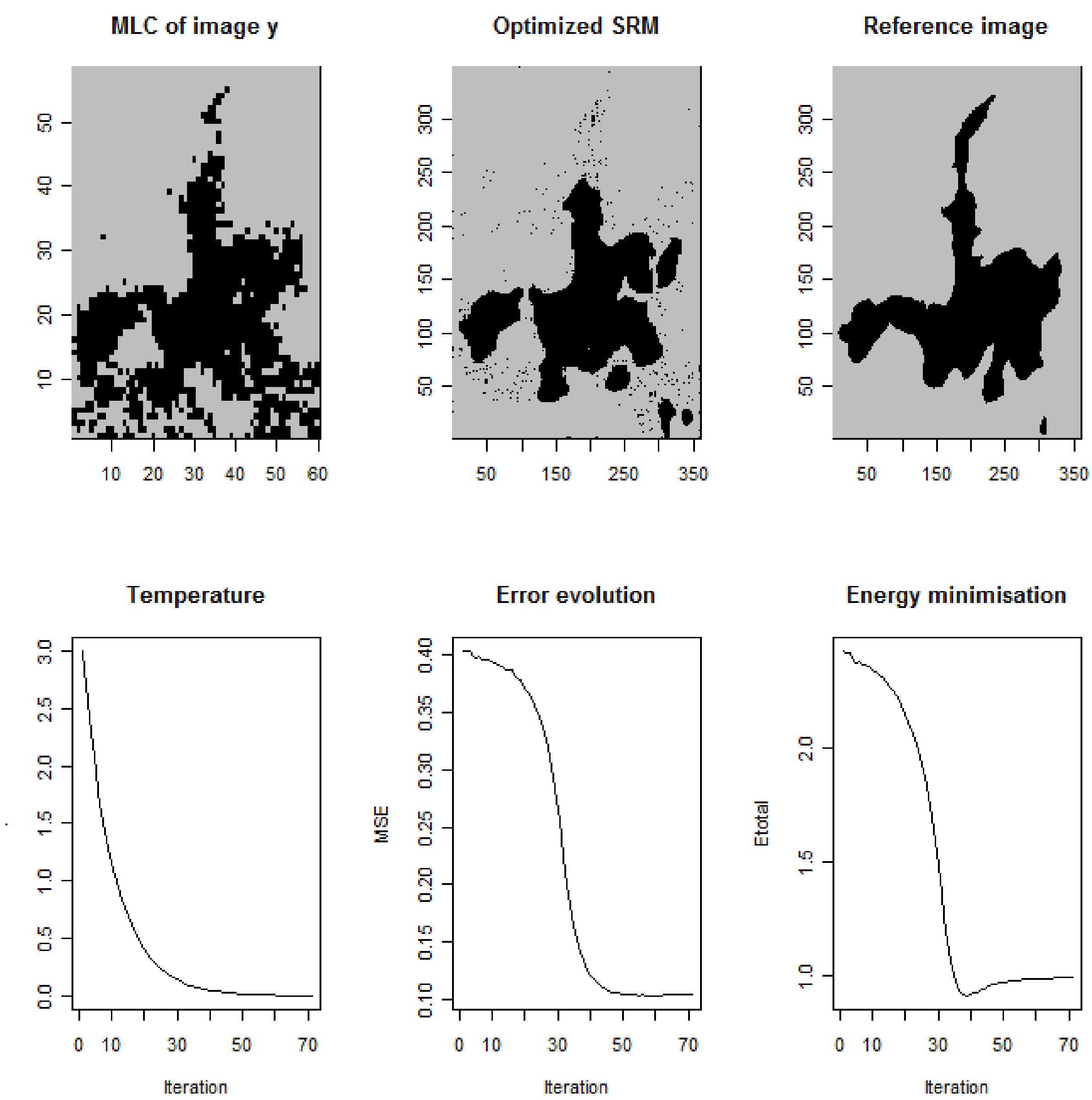
MLC of image y
Optimized SRM
Reference image
Temperature
Error evolution
Energy minimisation
MSE
Etotal
Iteration
Iteration
Iteration

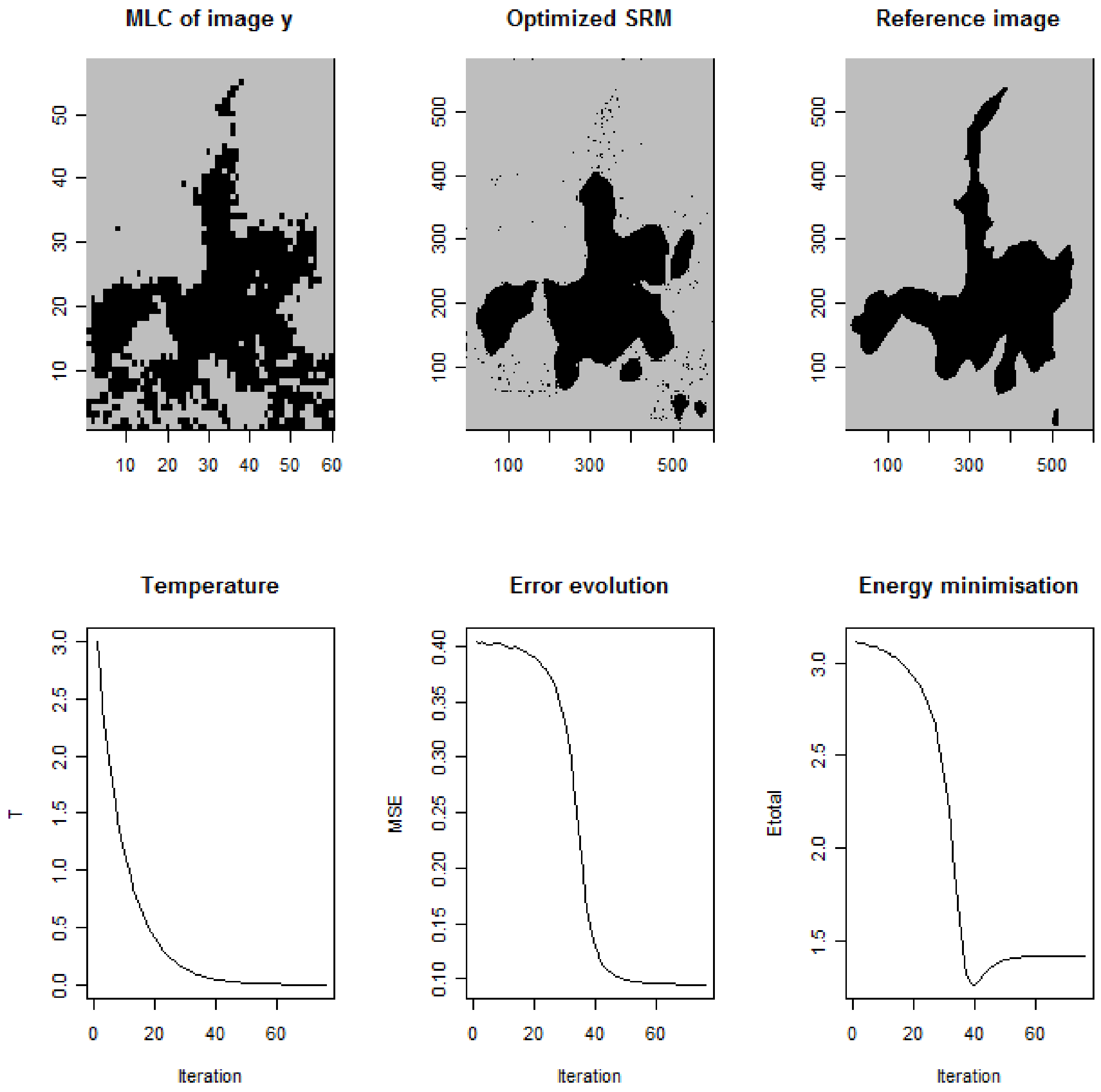

MLC of image y
Optimized SRM
Reference image
Temperature
Error evolution
Energy minimisation
T
MSE
Etotal
Iteration